UNIVERSIDADE FEDERAL DE PERNAMBUCO

CENTRO DE TECNOLOGIA E GEOCIÊNCIAS

DEPARTAMENTO DE ENGENHARIA MECÂNICA

PROGRAMA DE PÓS-GRADUAÇÃO EM ENGENHARIA MECÂNICA

YARGO JOSEPH DURAN PACHECO

Rain erosion fatigue life prediction model for wind turbine coatings: a case study for an offshore wind farm in Northeastern Brazil

Recife

2024

YARGO JOSEPH DURAN PACHECO

Rain erosion fatigue life prediction model for wind turbine coatings: a case study for an offshore wind farm in Northeastern Brazil

Dissertation submitted to the Graduate Program in Mechanical Engineering of the Universidade Federal de Pernambuco, as a requirement for the delivery of the degree of Master of Engineering in Mechanical Engineering.

Area of Concentration: Energy.

Advisor: Prof. Dr. José Ângelo Peixoto da Costa

Co-advisor: Prof. Dr. Frederico Duarte de Menezes

Recife

2024

Catalogação de Publicação na Fonte. UFPE - Biblioteca Central

Pacheco, Yargo Joseph Duran.
Rain erosion fatigue life prediction model for wind turbine coatings: a case study for an offshore wind farm in Northeastern Brazil / Yargo Joseph Duran Pacheco. - Recife, 2024.
121f.: il.

Dissertação (Mestrado) - Universidade Federal de Pernambuco, Centro de Tecnologia e Geociências, Programa de Pós-Graduação em Engenharia Mecânica, 2024.
Orientação: José Ângelo Peixoto da Costa.
Coorientação: Frederico Duarte de Menezes.
Inclui referências e apêndice.

1. Erosão pluvial do bordo de ataque; 2. Modelo de predição da vida em fadiga; 3. Dinâmica explícita; 4. Pás de turbinas eólicas. I. Costa, José Ângelo Peixoto da. II. Menezes, Frederico Duarte de. III. Título.

UFPE-Biblioteca Central

YARGO JOSEPH DURAN PACHECO

RAIN EROSION FATIGUE LIFE PREDICTION MODEL FOR WIND TURBINE COATINGS: A CASE STUDY FOR AN OFFSHORE WIND FARM IN NORTHEASTERN BRAZIL

Dissertation presented to the Graduate Program in Mechanical Engineering of the Universidade Federal de Pernambuco, Centro de Tecnologia e Geociências, as partial Mechanical Engineering requirement for the delivery of the Master's degree in Engineering. Area of concentration: Energy.

Aprovado em: 17/10/2024

BANCA EXAMINADORA

_____
Prof. Dr. José Ângelo Peixoto da Costa (Orientador)
Instituto Federal de Pernambuco

_____
Profª Drª Nadège Sophie Bouchonneau da Silva (Examinadora Interna)
Universidade Federal de Pernambuco

_____
Prof. Dr. Gustavo de Novaes Pires Leite (Examinador Externo)
Instituto Federal de Pernambuco

ACKNOWLEDGEMENTS

To my mother, Cristiane, and my grandparents, Jaime and Perfecta.

To my advisers, Ângelo and Frederico, for their support throughout this work.

To professors Nadège and Gustavo, for taking the time to review this dissertation, and providing helpful insights into it.

And to many of my family and friends: My sincere appreciation goes to all of you who have impacted and helped, in so many ways, in making this study.

ABSTRACT

Leading edge erosion by impacting rain droplets and dust particles has a substantial impact on the aerodynamic characteristics and power output of a wind turbine. With the increasing interest in offshore wind farms, with notably higher maintenance costs and greater susceptibility to leading edge erosion, predicting when the coating/protective system will start failing will be crucial for maintenance planning and keeping the power output of the wind turbine at the highest level. Computational models for rain erosion prediction in wind turbine blades are noted in the literature as a promising way to predict the erosion onset of a particular coating under specific environmental conditions. In the present study, a computational model for rain erosion prediction of the leading edge of wind turbine blades has been developed, taking into consideration the turbine power characteristics, coating material features, and raindrop size distribution, which was later combined with an empirically validated finite element analysis. The model was later employed in a case study for a prospective offshore wind farm located off the Northeastern Brazilian coast. First, numerical simulations of rain droplet impacts were conducted in Ansys Explicit Dynamics and validated against real-life experimental results. Then, the offshore wind farm area's wind and rainfall information were collected from actual satellite observations and climate reanalysis data. Simulations for several droplet diameters, from 0.5 up to 4 mm, impacting an epoxy coating were made, considering the wind turbine's average operating condition. The impact loads were then used as inputs for a fatigue life prediction model developed in the Python programming language. A sensitivity analysis was performed and shows that the model's accuracy has a large sensitivity to input data. The resulting impact stress and fatigue damage data were physically consistent. The erosion onset estimates were coherent for most droplet diameters, ranging from 0.46 up to 4.43 years of operating time and consistent with the values found in similar erosion models in the literature. Considering the average rain intensity in the area and its average droplet diameter, the estimated erosion onset is also in agreement with real-life observations in wind turbine blade coatings.

Keywords: Leading edge rain erosion; Fatigue life prediction model; Explicit dynamics; Wind turbine blades;

RESUMO

A erosão do bordo de ataque pelo impacto de gotículas de chuva e partículas de poeira tem um impacto significativo nas características aerodinâmicas e na potência gerada por uma turbina eólica. Com o crescente interesse em parques eólicos offshore, com custos de manutenção notavelmente mais altos e maior suscetibilidade à erosão do bordo de ataque, prever quando o revestimento/sistema de proteção começará a falhar será crucial para o planejamento da manutenção e conservação da potência da turbina eólica no mais alto nível. Modelos computacionais para predição da erosão por chuva de pás eólicas são apontados na literatura como uma forma promissora de predição da vida útil de um determinado revestimento sob condições ambientais específicas. No presente estudo, um modelo computacional para predição de erosão pluvial em pás eólicas foi gerado levando em consideração as características de potência da turbina, as características do material de revestimento, e a distribuição do tamanho das gotas de chuva, que foram então combinada com uma análise de elementos finitos validada empiricamente. O modelo foi então empregado em um estudo de caso para um parque eólico *offshore* prospectivo localizado na costa do Nordeste brasileiro. Primeiramente, simulações numéricas de impactos de gotículas de chuva foram conduzidas no *Ansys Explicit Dynamics* e validadas contra resultados de experimentos laboratoriais. Então, os dados anemométricos e de precipitação reais da área do parque eólico foram coletados de bancos de dados de observações por satélite e reanálise climática. Simulações de gotas de diâmetros, de 0,5 a 4 mm, impactando um revestimento epóxi foram realizadas considerando as condições médias de operação da turbina eólica. As cargas dos impactos simulados foram então utilizadas como entradas para um modelo de predição de vida em fadiga programado em linguagem Python. Uma análise de sensitividade foi realizada, e demonstra que a acurácia do modelo possui uma elevada sensibilidade aos dados de fadiga de entrada. As tensões de impacto e os dados de dano de fadiga resultantes apresentaram-se fisicamente consistentes. As estimativas de vida de erosão foram coerentes para a maioria dos diâmetros de gota simulados; indo de 0,46 a 4,43 anos de tempo em operação, e consistentes com os valores apresentados por modelos de erosão semelhantes na literatura. Considerando a intensidade de chuva média da área e seu diâmetro médio de gota, a estimativa de vida de erosão permanece congruente com as observações de campo para o início da erosão em revestimentos de pás eólicas.

Palavras-chaves: Erosão pluvial do bordo de ataque; Modelo de predição da vida em fadiga; Dinâmica explícita; Pás de turbinas eólicas;

LIST OF FIGURES

LIST OF TABLES

LIST OF ACRONYMS

AEP	Annual Energy Production
AMPS	Absolute Maximum Principal Stress
CAD	Computer-Aided Design
CFD	Computational Fluid Dynamics
CFL	Courant-Friedrichs-Lewy
EOS	Equation of State
FSC	Fatigue Strength Coefficient
FSE	Fatigue Strength Exponent
FEA	Finite Element Analysis
FSI	Fluid-Structure Interaction
GFRP	Glass Fiber Reinforced Polymer
GPM	Global Precipitation Measurement
HCF	High-Cycle Fatigue
IDF	Intensity-Duration-Frequency
IMERG	Integrated Multi-satellitE Retrievals for GPM
LCOE	Levelized Cost of Energy
LCF	Low-Cycle Fatigue
LEP	Leading Edge Protection
O&M	Operation and Maintenance
PDF	Probability Density Function
SPH	Smoothed Particle Hydrodynamics
TI	Turbulence Intensity
TRMM	Tropical Rainfall Measuring Mission

LIST OF SYMBOLS

α	Correction coefficient for spherical droplet shape [dimensionless]
Γ	Gruneisen coefficient [dimensionless]
ρ	Density [kg/m³]
σ	Nominal stress [Pa]
σ_a	Stress amplitude [Pa]
σ'_a	Corrected stress amplitude (Goodman relation) [Pa]
σ'_f	Fatigue strength coefficient [Pa]
σ_i	Endurance limit [Pa]
σ_m	Mean stress [Pa]
σ_u	Ultimate tensile strength [Pa]
$\Delta\sigma$	Stress range [Pa]
v	Poisson's ratio [dimensionless]
A	Angle of attack [degrees]
A_i	Impacting area [mm²]
b	Fatigue strength exponent [dimensionless]
C	Speed of sound in a medium [m/s]
D	Droplet diameter [m]
D_{rotor}	Rotor diameter [m]
f	Courant-Friedrichs-Lewy's stability time factor [dimensionless]
F	Fraction of liquid water in air comprised of drops with a diameter smaller than a specific diameter D [dimensionless]
F_p	Impact peak force [N]

h	Characteristic dimension of a finite element [mm]
h_k	Particle smoothing length
I	Rain intensity [mm/h]
m_1	Empirical constant (Goodman relation) [dimensionless]
n	Cycle number [dimensionless]
N	Cycle number to fatigue failure [dimensionless]
P	Water hammer pressure [Pa]
P_i	Bernoulli stagnation pressure [Pa]
r	Droplet influence radius [mm]
R	Load ratio [dimensionless]
Re	Reynolds Number [dimensionless]
S_1	Shock EOS linear input parameter [dimensionless]
S_2	Shock EOS quadratic input parameter[dimensionless]
t	Rain event duration [s]
Δt	Simulation time increment [µs]
V	Impact velocity [m/s]
V_p	Particle velocity [m/s]
Vr	Rotor rotational speed [rpm]
V_s	Shockwave velocity [m/s]
V_{water}	Volume of water collected per hour [mm³/h]
V_{wind}	Wind velocity [m/s]
V_D	Volume of a water droplet [mm³]
We	Weber Number [dimensionless]
Z	Specific acoustic impedance [Pa·s/m³]

TABLE OF CONTENTS

1. INTRODUCTION

1.1. BACKGROUND

Global climate change, energy supply, and costs of energy are becoming ever more present concerns for governmental authorities and society. In the last decades, there have been growing efforts to reduce CO2 emissions and other pollutants that increase global warming effects. In that regard, the wind energy industry plays a central role in the long and short-term international energy strategies, which led to a rapid growth in onshore and, especially, offshore wind energy generation. The current offshore wind energy potential can be considered to be in a momentous implementation state and is also expected to grow faster in the next couple of years (DÍAZ and SOARES, 2020). Around the world, installed wind energy capacity has more than tripled in the last decade, as presented in Figure 1.

Figure 1 – Worldly onshore and offshore installed wind energy capacity (MW) from 2011 to 2023.

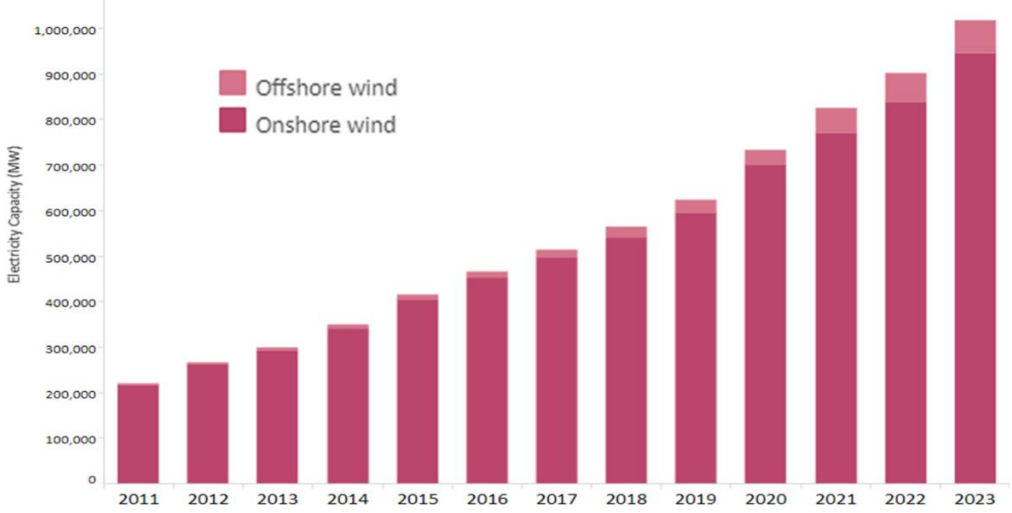

Source: IRENA (2024).

In Brazilian waters, initiatives for offshore wind enterprises are growing in number. With the publication of Decree nº 10.946, of January 2022, a new moment for offshore wind generation in Brazil might begin. Entering into force on June 15, 2022, the decree provides for the assignment of use of physical spaces and natural resources in inland waters under the Union's domain, in the territorial sea, in the exclusive economic zone, and on the continental shelf for the generation of electric energy from an offshore enterprise (BRASIL, 2022). By May 2024, 97 offshore enterprises are undertaking environmental licensing, totaling 15,500 offshore wind turbines, with an installed capacity of over 234 GW (IBAMA, 2024), as presented in Figure 2, a value more than 9 times greater than the installed capacity of onshore projects in the country in 2022, at 25.6 GW (ABEEólica, 2023).

Figure 2 – Evolution of demand for licensing offshore wind farms in Brazil.

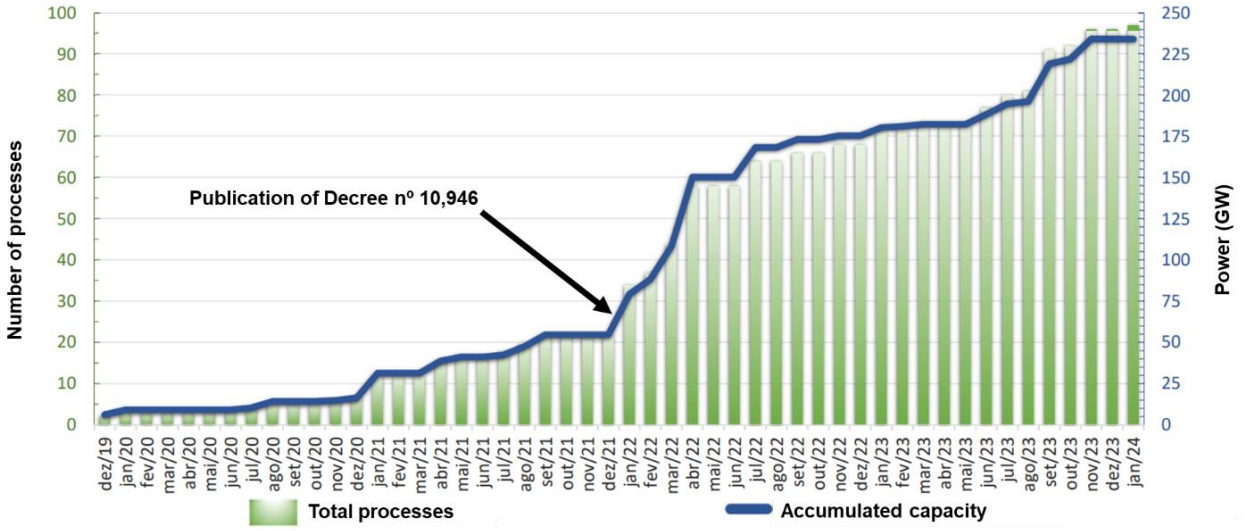

Source: IBAMA (2024).

Along with the expansion of onshore and offshore wind generation, there is a continuous and accelerated demand for the development of more powerful wind turbines. The most usual models in Brazil's prospective offshore market are the already operational Haliade-X from General Electric, which ranges from 12 to 14 MW of power and is equipped with 107.2 meters blades (GENERAL ELECTRIC, 2019), and the Vestas V236 prototype, with 15 MW of power and 115.5 m long blades (VESTAS, 2023), both with tip speeds surpassing 80 m/s at their rated operating speed. This trend has come a long way and, in the future, it is expected that the designs for wind turbines will continue to have increasingly larger rotors with greater tip speeds, as presented in Figure 3.

Figure 3 – Wind turbine dimensions over decades and future trends.

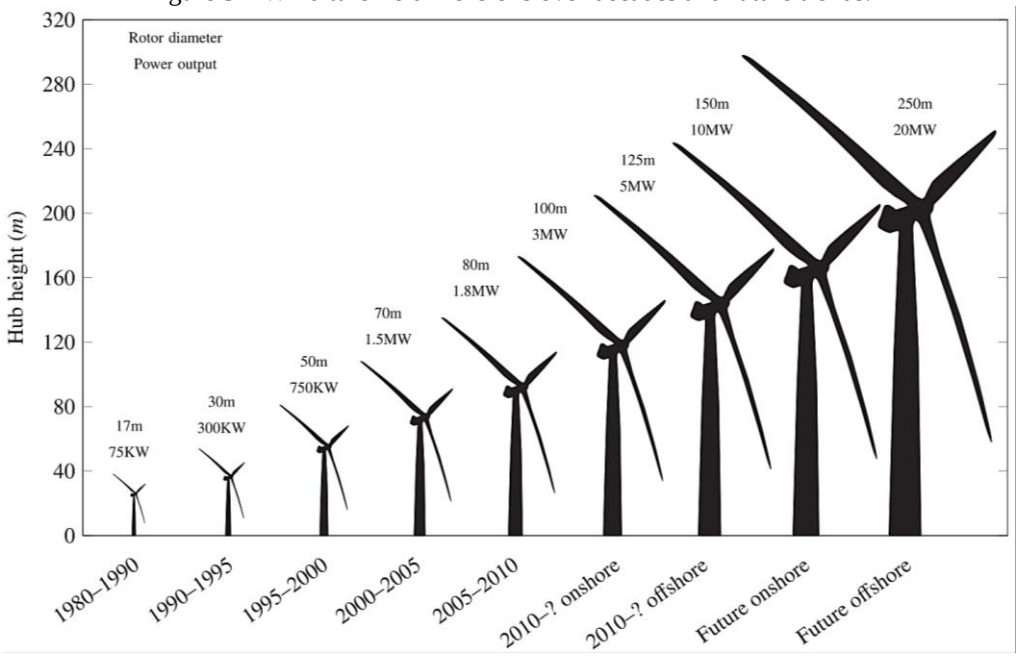

Source: AMIRZADEH et al. (2017a).

This combination, associated with the trending transition to an offshore generation model, makes wind blades more susceptible to erosion phenomena. Leading edge erosion begins early in the life of a blade, and it may show signs of wear within 3 years of operation if some type of protection has not been applied on the leading edge during its manufacturing (REMPEL, 2012). Turbine models are designed for an operating period ranging from 20 to 25 years, during which the leading edge of the blades will continually collide at high speed with water droplets, hail, insects, sand, and other airborne particles. These multiple, repeated random impacts cause shock waves to propagate through the coating, accumulating damage and irreversible deformation, which in turn cause damage that leads to coating erosion, such as the initiation and propagation of fractures, fragmentation, abrasion, and fatigue (MISHNAEVSKY, 2019).

This phenomenon can substantially reduce airfoil performance, yielding a large increase in drag coupled with a significant loss in lift, which are key factors in minimizing wind turbine energy production (SAREEN, 2014). For current wind power systems - operation and maintenance costs (O&M) typically represent 20% to 25% of the total Levelized Cost of Energy (LCOE) (COSTA et al., 2021). Considering the difficulties around checking and maintaining wind turbines at frequent intervals, with their maintenance being a costly, time and labor-intensive activity, blade erosion becomes a high-impact problem for the wind industry. In 2016, for example, just 6 years after the start of operations at the Danish offshore wind farm Horns Rev 2, the owner, Ørsted, had to remove for repair all 273 blades of the park, which were severely eroded (MISHNAEVSKY, 2019).

1.2. MOTIVATION

Performance degradation of the wind blade is initiated in the early stages of erosion, where the surface roughness starts to increase. A rougher surface increases the aerodynamic drag coefficient of the blades, which results in an undesirably lower performance and energy loss. For example, in a 2.5 MW wind turbine, simulated erosion experiments have shown that leading edge erosion can severely affect the airfoil performance to such an extent that, depending on the severity of erosion, up to 25% annual energy loss can be expected (SAREEN et al., 2014).

To combat leading edge erosion several commercial solutions have been developed and proposed in recent years, involving the use of polyurethane elastomer coatings, tapes, and shells, as well as thermoplastic erosion shields, as presented in Figure 4. While these products

provide erosion protection to the leading edge, most of their service lives are still significantly inferior to the 20 to 25-year design life of a wind blade. In addition, because they are located near the tip of the blades, an aerodynamically sensitive section, the application of leading edge protection (LEP) systems, unless fully integrated into the blade, can affect its aerodynamic performance (SAPRE, 2012).

Figure 4 – Different types of solutions for the leading edge erosion protection. (a) BladeRep's LEP 9 multilayered coating solution; (b) 3M's wind protection tape; (c) Polytech's ELLE pre-cast polyurethane shell (d) Helicopter blade equipped with electroformed nickel plates.

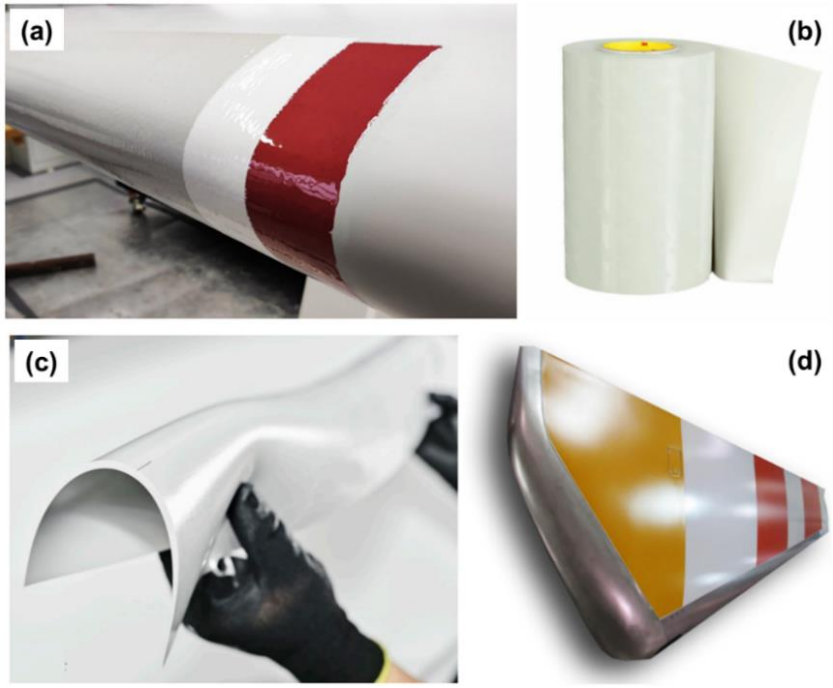

Source: (a) BLADEREP; (b) 3M; (c) POLYTECH; (d) HERRING (2018).

In general terms (not accounting for specific environmental conditions, such as anti-icing capabilities for example), an efficient anti-erosive wind blade leading edge protection system should meet the following pre-requisites (CHEN et al., 2018; MISHNAEVSKY, 2021):

1. **Erosion resistance:** The coating must be resistant to the impingement of liquid and solid particles such as rain, dust sand, hail, and insects.
2. **Weatherability:** The material must be resistant to atmospheric weather conditions such as ultraviolet radiation degradation, flexibility for extreme hot and cold temperatures, humidity, saline air, and other corrosive conditions (acidic or alkali).
3. **Excellent adhesion to the substrate:** The interface between the coating and the substrate is highlighted as a key aspect, as poor adhesion can lead to delamination and, ultimately, premature failure of the coating (CORTÉS et al, 2017). Bonding enhancement can be achieved mechanically through surface

sanding and cleaning, or chemically by, first, selecting a chemically compatible coating-substrate system and, second, by the application of primer material.

4. **Minimal aerodynamic impact:** Erosion shells and shields, while being more efficient in protecting the blade, are also more prone to changing their aerodynamic performance, while contributing to the mass and moment of the blade. The metallic solutions may even require a complete redesign of the airfoils and blade chords to allow for their implementation (HERRING, 2018).
5. **Ease of manufacture:** The system must be able to be easily integrated into the blade's manufacturing process and, consequently, with its other components. Pre-fabricated solutions are preferable, as they are quicker to install, and have a much lesser risk of having manufacturing defects such as air voids trapped during a coating application (DOAGOU-RAD and MISHNAEVSKY, 2020), which act as stress raisers and initiation points for erosion.

The best-performing solutions erosion-wise, the metallic erosion shields are typically composed of stainless steel, nickel, or titanium alloys and have been shown in accelerated rain erosion tests to possess a lifetime greater than that of an offshore wind turbine blade. However, differences in stiffness between the blade and the metallic shield introduce a risk of the shield detaching under loading and as a result, the reliance on the adhesive is high (HERRING et al., 2019). Another major technical challenge specific to this solution is how to integrate the metallic shield into the turbine lightning system since such a large, exposed metallic area will be much more prone to lightning strikes, requiring a much more costly and redundant lightning protection system.

In the coming years, while there is no protection technology with the endurance to match the design life of a wind blade, that is commercially viable, has an acceptable effect on the blade's aerodynamic performance, and can integrate well with the blade manufacturing processes (ease of manufacturing, plus cost and time effectiveness) and its other components, the leading edge erosion will remain an issue, driving operation costs higher with maintenance needs and annual energy production (AEP) losses. With the increasing interest in offshore wind farms, their notably higher maintenance costs, and susceptibility to leading edge erosion, predicting when the coating/protective system will start failing will be crucial for maintenance planning and keeping the AEP performance of the wind turbine at the highest level.

Recently, one of the most proposed tools for dealing with leading edge erosion (AMIRZADEH et al., 2017ab; VERMA et al., 2021; HU et al., 2021), and the main focus of

this study, are computational models for rain erosion prediction in wind turbine blades. By acquiring data for the rainfall history at the wind turbine location, the mechanical properties of its leading edge coating material, and the operational conditions of the wind turbine, these models can output the erosion incubation time: meaning, the time it takes for the blade coating to start losing mass and developing undesirable roughness, allowing predictive instead of corrective interventions, driving maintenance costs and performance loss down. They can also be integrated into viability studies for wind enterprises, providing quantitative, comparable data for analysis of maintenance costs, and being employed as tools to support the design and validation of new rain erosion-resistant solutions.

In Brazil, which currently does not have any offshore wind farms installed or under construction, there are plans to install more offshore wind than the rest of the world has built up to today combined. Major objectives for Brazil are not only to supply power to the population-dense areas along its extensive coast but also to create a parallel trade market for oil exports through large-scale production of hydrogen through these wind projects. In 2020, Brazil's 2050 National Energy Plan (NEP 2050) predicted the potential installed capacity of offshore wind will reach 16 GW by 2050 (GLOBAL ENERGY MONITOR, 2024). For the present licensing offshore enterprises, almost half of the licensing demands can be accounted to the Northeast region, with almost a third of the total number in the state of Ceará only, bounding the region to be the definite hotspot for the future offshore wind energy production in the country.

1.3. RESEARCH AIM

This study aims to develop a methodology for evaluating rain erosion failure in the leading edge of offshore wind turbine blades, applying an empirically validated computational model to predict the fatigue life failure of a choice coating under location and turbine-specific environmental conditions. Ultimately, the model will be applied to a case study for a prospective offshore wind farm location on the Northeastern coast of Brazil.

This is the first study where a finite element-based rain erosion fatigue life prediction model is applied to the conditions weathered by an actual commercial offshore wind turbine while accounting for the wind turbine’s power characteristics, and genuine wind and precipitation data from its, as of now prospective, offshore wind farm area.

1.4. RESEARCH OBJECTIVES

- Create an ANSYS Explicit Dynamics model to simulate liquid droplet impingement against solid surfaces and validate it against empirical droplet impact results. The impacting loads from the model will later serve as inputs to an erosion model.
- Develop a fatigue life prediction model for qualitative analysis and prediction of rain erosion onset in the leading edge of wind turbine blades.
- Apply the fatigue life prediction model to a case study for wind turbine blades located in a prospective offshore wind farm in Brazilian waters off its Northeastern coast. This aims to verify if the fatigue life model is capable of providing physically coherent fatigue damage and erosion onset time results.

2. LITERATURE REVIEW

In this chapter, a literature review is presented. A summary of the history and mechanisms of rain erosion, alongside its effects on the leading edge of wind turbine blades, is presented, followed by a discussion on the dynamics of liquid droplet impact on solid surfaces, the modeling and prediction strategies for liquid impingement erosion, the fatigue life prediction methods and finally some concepts for explicit dynamics simulations.

2.1. A BRIEF HISTORY OF RAIN EROSION

The basic theory needed to understand the major features of high-speed liquid impact has existed for over one hundred years; as such, high speed in this context refers to impact speeds above 50 m/s. The water hammer pressure was first analyzed by JOUKOWSKY (1898), in the context of the hydraulic shock within water pipes. Later, although the damage was deemed to have been caused by cavitation, COOK (1928) discussed liquid impact in terms of compressional waves in what was the first experimental study that tested the resistance of materials to cavitation. This understanding, though, did not lead to any significant advances in quantitative calculations. The turning point towards a renewed and extended application of the rain erosion theory came during the 1960s when this problem piqued the interest of the aircraft erosion community (LESSER, 1995; O'CARROLL, 2018).

Erosion by rain on the exterior of high-speed aircraft during flight was observed during World War II on all-weather fighter airplanes capable of flying at 640 m/s and over. The aluminum edges of wings and particularly of the glass-fiber-reinforced polymer (GFRP) radomes (particularly the Eagle Wing on B-29s flying over the Pacific) were particularly susceptible to this form of degradation. In 1947, the United States Air Force first began research at the Wright-Patterson Materials Development Center, which resulted in one of the first applications of anti-erosive coating, manufactured from 127 μm thick elastomeric neoprene and adhered adhesively to the surface of aircraft radomes (ROSATO et al., 1991).

During the 1960s, the majority of tests undertaken during this period were funded by the U.S. military, and most took place on ground-based systems that allowed a small sample of the candidate material to travel through an artificially generated rain field. Over time, damage would form on the surface of the sample, and these tests allowed for the appropriate ranking of a range of materials based on their resistance to rain erosion. Thus, a range of techniques was

developed and utilized: these included whirling arms, rocket sleds, and in-service testing (O'CARROLL, 2018).

Later, it was only by the usage of the developing techniques of high-speed photography and by clever experimental design that a better understanding of the mechanisms of rain erosion was achieved (LESSER, 1995). Works like the ones of BOWDEN and FIELD (1964), and BRUNTON (1966), developed several new techniques for creating impact events and for viewing them, making visible several of the features associated with the initial stages of impact, and developing the theoretical comprehension of liquid impingement on solid surfaces.

When solutions to the prevailing engineering problem had been found, interest in this damage mechanism appeared to diminish, until wind turbine blades started showing similar signs of erosion in the late 1990s. Like aircraft, wind turbine blades are also eroded due to environmental weather. Although these structures do not travel through the air at speeds comparable to aircraft, they are manufactured from polymers, and not metal, materials that can be eroded rather quickly by rain droplets (O'CARROLL, 2018). The steady increase in blade size and tip speed has only aggravated this problem throughout the years. Besides, unlike aircraft, wind turbines cannot be checked and maintained at frequent intervals, and their maintenance is a very costly, time, and labor-intensive activity, making the erosion of wind blades a high-impact problem for the wind industry.

2.2. EFFECTS OF LEADING EDGE EROSION IN WIND BLADE PERFORMANCE

The blade is a key component for wind energy conversion, and its erosion at the leading edge has introduced severe problems to many wind power enterprises. To understand the significance of leading edge erosion on wind turbine blades, it is important to consider the effects that such erosion will have on the performance and lifetime of the blade, as well as on the performance of the turbine as a whole (KEEGAN, NASH and STACK, 2013). As one of the most important characteristics of a wind turbine blade is its aerodynamic performance, the occurrence of leading edge erosion may pose a threat to the wind turbine's efficiency, and consequently to the management plan and maintenance strategy made for a wind farm, which is closely related to economic benefits of the wind power enterprise (SØRENSEN, 2009).

Wind turbine blades are exposed to precipitation that occurs in a variety of forms and myriad abrasive airborne particles that can, over time, erode their surfaces, particularly at the leading edge. These airborne particles can cause blade erosion damage, reducing aerodynamic performance and hence, energy capture. Leading edge erosion of the blades begins with a

gradual increase in the blade's surface roughness until small pits form near the leading edge. Over time, the density of these pits increases until gouges are formed, growing in size and density and combining to cause delamination near the leading edge (SAREEN et al., 2014). Figure 5 presents the extent of the damage that leading edge erosion can cause on wind turbine blades in service as time progresses.

Figure 5 – (a-f) Several stages of leading edge erosion phenomenon in wind blades.

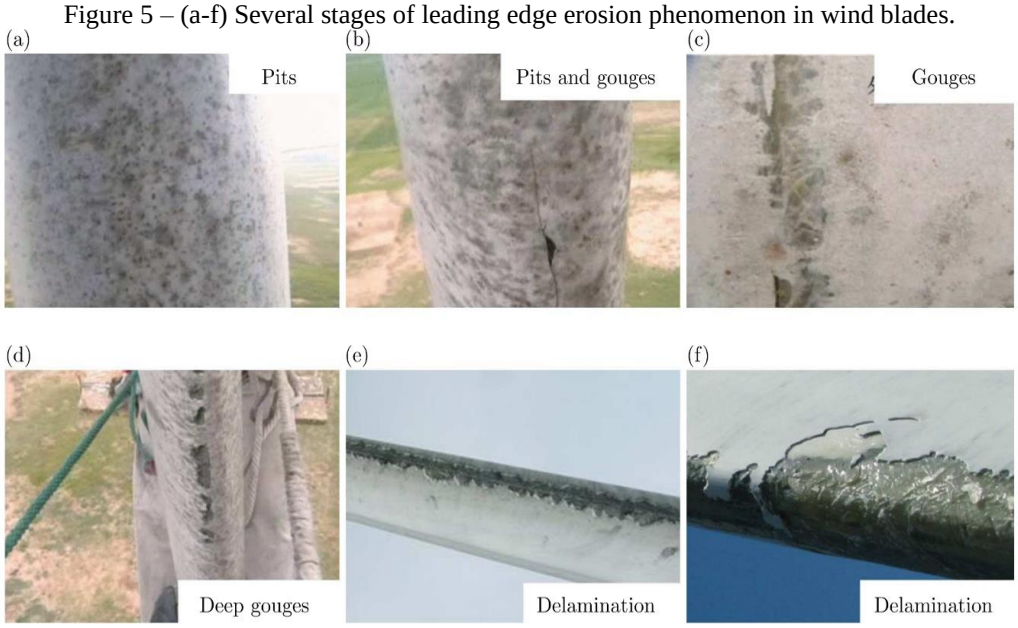

Source: REMPEL (2012).

The detrimental nature of leading edge erosion is well known across the industry, and some efforts have been made to quantify the effect of erosion on wind turbine performance, as well as the accretion of ice, dust, and insect debris. The 3M company found through field experiments that the power loss of a 1.5 MW wind turbine with no leading edge protection could reach 20% to 30% after five years of operation (POWELL, 2011). In a related research, SAPRE (2012) made a comparison between the performance losses due to the use of wind protection tape and due to leading edge erosion to determine the feasibility of using the tape for practical purposes. The results indicated a relatively small rise in drag depending on the extent of the tape on the upper and lower surfaces of the airfoil edge. The rise in drag values due to tape usage spanned a range of 5–15%, while the loss in lift was considered insignificant. For a particular case of the tape extending up to 20% on both upper and lower surfaces, the predicted annual energy loss was close to 0.38%.

GAUDERN (2014) took leading edge erosion data from Vestas' wind turbine blades with up to five years of service and applied its erosion features at different erosion stages to airfoil samples in wind tunnel testing. The study found that as the pattern severity/depth of the erosion increased the airfoil performance decreased, ultimately reducing the lift-drag ratio of

the airfoil from 35% up to 47% in the initial and most severe erosion cases, respectively. SAREEN et al. (2014) conducted wind tunnel experiments with DU 96-W-180 airfoils with varying severity and types of leading edge erosion, showing that leading edge erosion on a wind turbine airfoil can produce significant aerodynamic performance degradation, with test data showing an increase in drag from 6–500% due to erosion (light to heavy erosion cases, respectively). Leading edge erosion has also caused a substantial reduction in the lift coefficient, especially at the higher angles of attack that wind turbines experience during operation, as well as a large increase in the drag of the airfoil and an earlier onset of stall (i.e., at lower angles of attack). It was estimated that an 80% increase in drag, a condition caused by a relatively small degree of leading edge erosion, could result in a 5% loss in annual energy production. Considering an increase in drag of 400-500% along with a loss of lift, as seen in many cases of moderate to heavy erosion, the loss in annual energy production can reach up to 25% for 2.5 MW wind turbines. BECH, HASAGER, and BAK (2018) presented a strategy framework for predicting and mitigating leading edge erosion, based on and supporting the hypothesis that most of the damage accumulated in the leading edge is imposed at extreme precipitation conditions events that occur during a tiny fraction of the turbine's operation life. They demonstrated that reducing the tip speed of the blades during extreme precipitation events may lead to an increase in the service life of the leading edge from a few years to the full expected lifetime of the wind turbine. They have estimated that this life extension may cost a negligible reduction in AEP in the worst case scenario, and a significant increase in AEP in the best.

HAN et al. (2018) used simulations to analyze the effects of contamination and leading edge erosion in the annual power generation of a 5MW wind turbine. The simulations indicated that depending on the severity of the conditions, contamination and erosion conditions reduced and increased the lift and drag coefficients, respectively, of the blade by up to 53% and 314%, while the annual energy production was reduced by 2%–3.7%. WANG et al. (2021) created a computational model to assess the aerodynamic impact on the leading edge of a wind turbine blade with pitting erosion and three levels of delamination. The results showed that the degrees of leading edge erosion have a great influence on flow separation, tangential force coefficient, normal force coefficient as well as the power output of the wind turbine. Considering wind speeds from 7 m/s to 20 m/s, leading edge erosion had the greatest impact on the aerodynamics of the wind turbine at 15 m/s, where the maximum loss in the power output can reach up to 73.26%. This is indicative that there may exist a peak wind speed for the impact of leading edge

erosion on the power generation of the wind turbine, as the impact of leading edge erosion on the power output increases first and then decreases with the increase in the wind speed.

It can be concluded that leading edge erosion has a significant impact on the aerodynamic characteristics and power output of a wind turbine. Furthermore, for current wind power systems, O&M costs typically represent 20% to 25% of the total LCOE (COSTA et al., 2021), not considering the decline in power output from wind turbine blades' leading edge undergoing erosion, and the necessary downtime and costs to repair such damage. Therefore, the understanding and prediction of the effect of leading edge erosion on aerodynamic and flow field characteristics of the wind turbine blade are helpful for the optimization of wind turbine design, safe operation, blade maintenance, and management of wind farms, improving the economic health of the wind power generation enterprise.

2.3. RAIN EROSION MECHANISMS

Different failure mechanisms may be active during the period when a high-speed liquid, such as a droplet, impacts a solid surface. BRUNTON (1966) studied the deformation of solids by the impingement of liquids by impacting a high-speed water jet against the surface of a solid. Three predominating forms of failure were observable:

1. Failure in the region of impact due to the rapid application of a large load over an area roughly equal to the cross-sectional area of the drop. In hard polymers and brittle solids, this causes circumferential fractures, ring cracks, and sometimes, in materials that show some tendency to deform plastically, subsurface shear cracks (Figure 6a). In metals, and in materials capable of deforming plastically at very high rates of strain, a simple surface depression is produced (Figure 6b).
2. Localized failure at surface discontinuities such as scratches, pits, inclusions, and cracks, due to the shearing action of liquid flowing across the surface at high speed. Surfaces that remain smooth during the impact are not affected by this shearing action. Failure of this kind is true erosion since it usually involves the removal of material from the surface.
3. Failure caused by reflection and interference of waves in the solid. This mode of failure is found mainly in hard brittle solids, and when it occurs it is often more damaging than failure in the impact area. It is somewhat controllable as it is dependent on the shape and size of the solid target.

Figure 6 – Deformation due to water jet impact. (a) Ring deformation in polymethylmethacrylate. (b) Depression formed by the deformation of aluminum. The wavy deformation around the rim of the depression is caused by the shearing action of high-speed liquid flow.

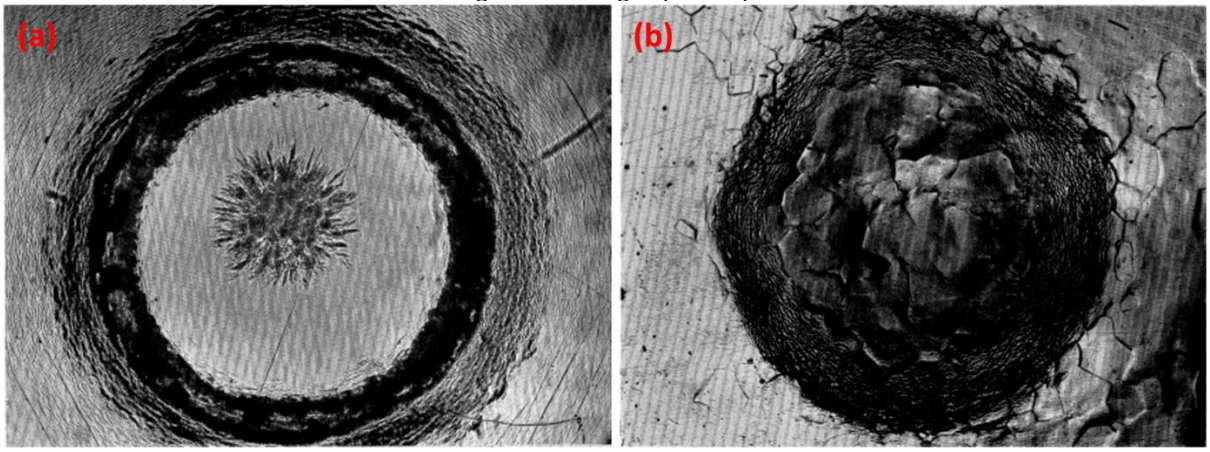

Source: BRUNTON (1966).

Each of these modes of failure can be traced to phenomena intrinsic to, in this case, droplet impact. When the droplet first impacts the surface, an area of high pressure builds up at the point of contact – a phenomenon known as water-hammer (see Section 2.3.2). On contact, pressure waves (often referred to as stress waves) propagate into the target material and travel through it, reflecting off any interfaces present. These waves are also reflected into the water droplet and force the water out of the droplet and along the target surface at a very high velocity (see Section 2.3.3). Next, the water jets away radially from the center of the droplet several times faster than the initial impact velocity (see Section 2.3.4). Each of these specific mechanisms is interconnected, and consequently, it is difficult to explain one independently without stating the effect of the others (O`CARROLL, 2018).

2.3.1 The stages of liquid erosion

The progression of the liquid impact erosion phenomena can be expressed by measuring mass loss over time. Based on experimental mass loss data, SPRINGER and YANG (1975) modeled the behavior of fiber-reinforced composite materials subjected to repeated impingements of liquid droplets and derived equations based on fatigue theorems to describe every stage of rain erosion, listed in the scheme presented in Figure 7. During a period after the start of the erosion process, there is no observable mass loss in the target, a period that is known as the incubation period. After enough fatigue degradation has accumulated, the material enters the second stage, the increasing period, where mass loss begins and accelerates, eventually reaching a steady mass loss state where the material tends to lose mass nearly linearly with time. This stage is then followed by the placid period during which the mass loss rate is reduced.

Figure 7 – Mass loss vs. time in liquid impact erosion and its stages.

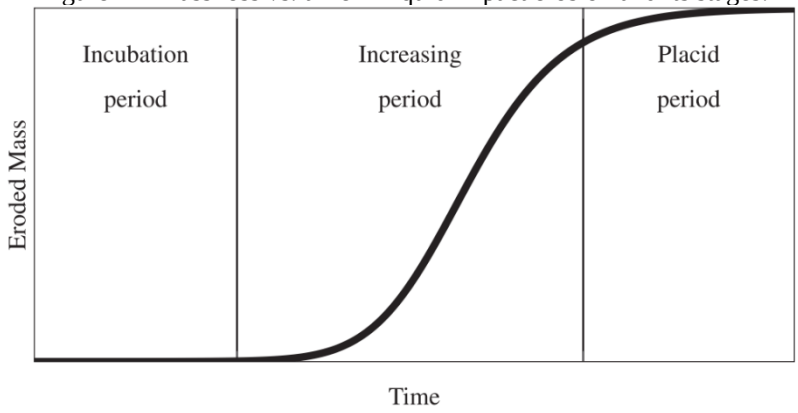

Source: AMIRZADEH et al. (2017b).

During the impact between a spherical drop and a solid surface, the droplets' morphology and associated impact regimes will stay the same over a great range of diameters and velocities. It is when the droplet's impact regime and the surface quality are assessed together that it becomes clearer how the erosion processes happen and how different erosion mechanisms can be active. These mechanisms can be divided into four main categories: direct deformation, stress wave propagation, lateral outflow jetting, and hydraulic penetration (ADLER, 1979 apud AMIRZADEH, 2017a).

Initially, during the incubation period, while the surface is still regular and smooth, the damage mechanisms are restricted to direct deformation due to the droplet impact and its consequent stress waves propagating into the solid medium. During incubation, overall mass loss is not significant, and the damage is mainly attributed to the fatigue of the solid target material: surface roughness increases, and points for concentrated failure become evident such as microcracks, asperities, and cavities. When that happens, surface roughness is increased, and the lateral jetting and hydraulic penetration mechanisms are activated, becoming the main contributors to erosion, mostly through shear-induced damage and crack opening (JACKSON and FIELD, 2000). When encountered by surface asperities, the high-speed lateral jets can cause large shear stresses on the surface. Hydraulic penetration occurs when there are open cracks on the solid surface, and high-speed liquid can flow into these cracks and create elevated pressures at the tip of the cracks which furthers their growth. In the end, as the surface roughness is severely increased, liquid material accumulates on the surface and reduces the impact damage of the incoming drops, which explains the reduced mass loss rate in the placid period (ARMIZADEH et al., 2017a).

2.3.2 Direct impact and the water hammer pressure

In 1928, COOK (1928) already discussed liquid impact in terms of compression waves sweeping through the involved mass and demonstrated that the pressures generated within a flow of water could be large enough to erode turbine blades made of steel, clearly recognizing the importance of the water hammer pressure. Using Cook's description, the water hammer phenomenon happens when a moving droplet of water is suddenly arrested by a fixed, rigid surface, and there is a sudden arrest of the front layer of the impinging droplet, compressing a portion of the fluid. As water is virtually incompressible, high pressures are generated and transmitted to the impacting object as potential energy.

For a drop or jet impact, the pressure at the liquid-solid interface is taken to be constant and is approximated by the water hammer pressure. The equation for water-hammer pressure for an impact with a homogenous, isotropic, elastic solid, for a cylindrical jet (Equation 1) and a spherical drop (Equation 2), becomes (PREECE and MACMILLAN, 1977):

$$P = \frac{\rho_0 C_0 V_0}{1 + \frac{\rho_0 C_0}{\rho_1 C_1}} \tag{1}$$

$$P = \frac{\propto}{2}\left[\frac{\rho_0 C_0 V_0}{1 + \frac{\rho_0 C_0}{\rho_1 C_1}}\right] \tag{2}$$

where P is the water hammer pressure, ρ_0 and C_0 are the density and acoustic velocity of the liquid, respectively, V_0 is the impact velocity, $\propto$ is a dimensionless constant (where $\frac{\propto}{2}$ is a correction coefficient for the spherical shape of the drop), and the subscripts 0 and 1 pertain to the liquid and solid, respectively.

The ratio of acoustic pressure to the associated particle speed in a medium is the specific acoustic impedance (Z). For planar waves, it amounts to the product of the density (ρ) by the speed of sound of the material (C). The product ρC often has greater acoustic significance as a characteristic property of the medium than does either ρ or C individually. For this reason, ρC is called the characteristic impedance of the medium (KINSLER et al., 2000). In that, the water hammer pressure equation for a droplet becomes:

$$P = \frac{\propto}{2}\left[\frac{Z_0 V_0}{1 + \frac{Z_0}{Z_1}}\right] \quad (3)$$

It can be noted from Equation 3 that the acoustic impedance affects the generated pressures, as presented in Figure 8, where it is shown that as the acoustic impedance ratio (relative to water) increases so does the impact pressure. (O'CARROLL, 2018).

Figure 8 – Impact pressure for water droplets of different velocities impinging on materials of different acoustic impedances relative to water.

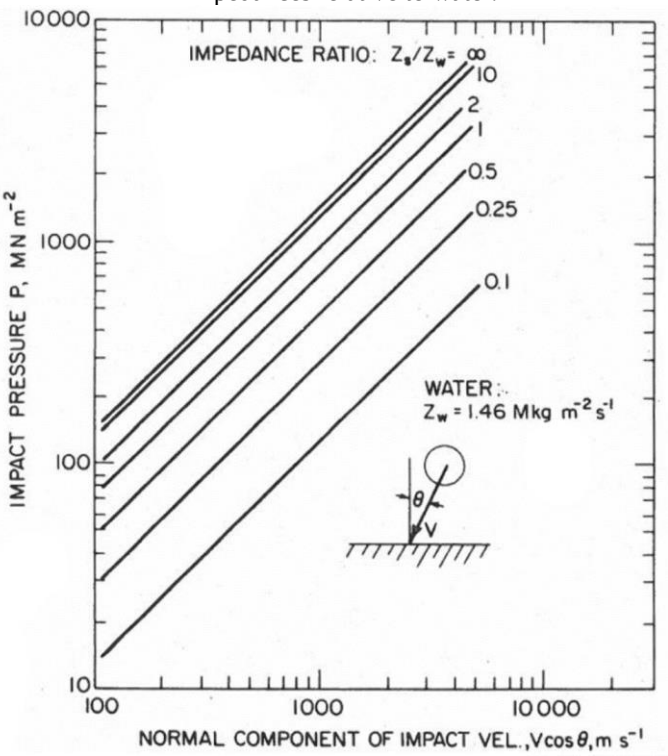

Source: SPRINGER (1976).

When a spherical water droplet impacts onto a surface, the contact periphery between the liquid and solid initially expands supersonically, generating a shock envelope that compresses the liquid behind it, the water hammer pressure (Figure 9). Due to the geometry of the droplet and its curved front profile, the contact edge slows down allowing the shock front to eventually overtake it (COAD, 1997). When that happens, the lateral jetting regime begins.

Figure 9 – Schematic of a post-impact water droplet, indicating the areas of high pressure where the water hammer is affecting the material.

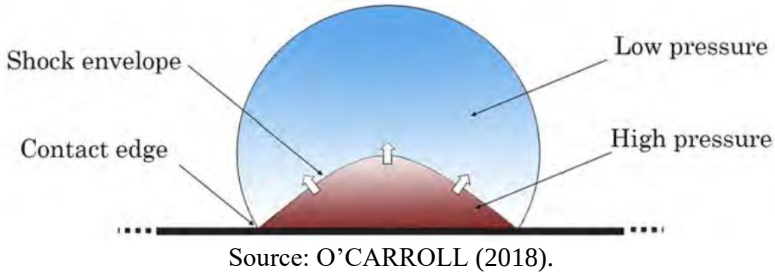

Source: O'CARROLL (2018).

2.3.3 Stress waves propagation

The mechanical equilibrium, or the state of stress in the target material is disturbed by the droplet impact and the pressure it creates on the impact zone. Three large pressure waves – often referred to as stress waves – emerge from the impact zone to propagate this disturbance to the rest of the solid target, and therefore, shape its stress and strain field. Two bulk waves propagate outwards into the target from the impact point: a dilatational wave traveling in a longitudinal direction (compressional waves), and a shear wave traveling in a transverse direction. The other shear wave is called a Rayleigh wave, which moves along the surface and interacts with surface cracks (JACKSON and FIELD, 2000; IBRAHIM and MEDRAJ, 2020). Figure 10 illustrates the directions and the interaction of these stress waves.

Figure 10 – Stress waves generated at the impact of a liquid drop on a rigid material: Compressional waves, shear waves, and Rayleigh surface waves interact with each other and their reflections.

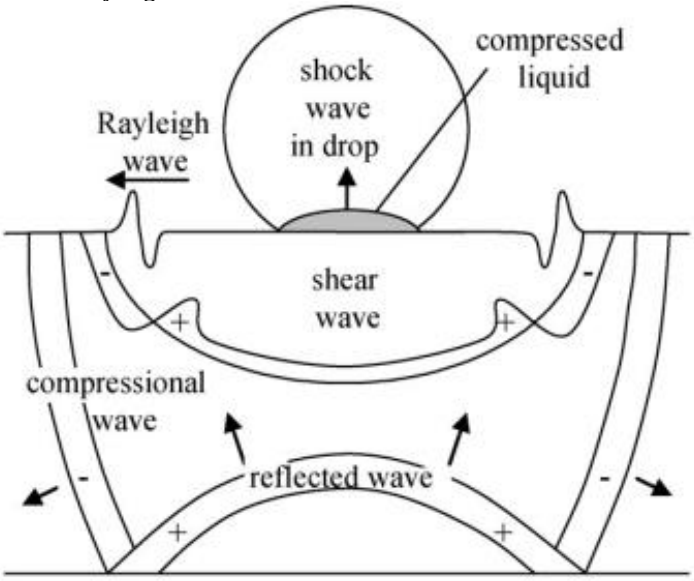

Source: GRUNDWÜRMER et al. (2007).

Compressional waves, often referred to as longitudinal or dilatational waves, are waves in which the oscillation of the medium is parallel to the direction in which the wave is traveling. These waves travel directly through the thickness into the material from the point of impact and will reflect off any interfaces with another material possessing a different acoustic impedance. These reflections take place in the target material, and some of the waves are even reflected into the droplet, influencing the jetting process (O'CARROLL, 2018).

Longitudinal waves are initially in compression but will flip to tensile waves when reflecting off any interface. The compression wave has little effect on the damage pattern, however, when it reflects and changes phase to a tensile wave it can cause fracture. This is particularly important with small specimens, as with thin plates, reflected waves from the rear

surface can reinforce the front surface Rayleigh wave and cause bands of fracture (JACKSON and FIELD, 2000). These waves can travel, back and forth, between the target surface and the interfaces within the material many times before dissipating. The ratio of acoustic impedances between the materials governs how much of the energy from the stress wave is transmitted and how much is reflected. If the acoustic impedances of the materials on either side of an interface are very similar, most of the energy will be transmitted across the interface – on the other hand, if the acoustic impedances are very different, then most of the energy will be reflected (SPRINGER, 1976, apud O'CARROLL, 2018).

Shear waves, or transverse waves, are waves whose oscillations are perpendicular to the direction of the wave's advance. Shear waves are slower than compressional waves, and while they are comparatively weaker, they can interfere with the longitudinal waves. The interference created between all these stress waves moving throughout the material can cause damage to occur at different depths in the material – this is demonstrated in Figure 11. There are the expected surface fractures at (A), but also fractures at (C), which are probably formed as a result of the interference between the reflected compressional wave and the slower outgoing shear wave (BRUNTON, 1966).

Figure 11 – Cross section through a 3-5 mm thick polymethylmethacrylate plate impacted by a water jet at the location marked by the red cross). Fractures at A are shear fractures and lie along shear trajectories. Fractures at B are caused by the tangential tensile stresses across the front of the expanding dilatational wave. Fractures at C and D are the result of the reflection and interference of the initial compression wave. Note that the scabbing fractures at D are more extensive than the ring fractures on the impact surface.

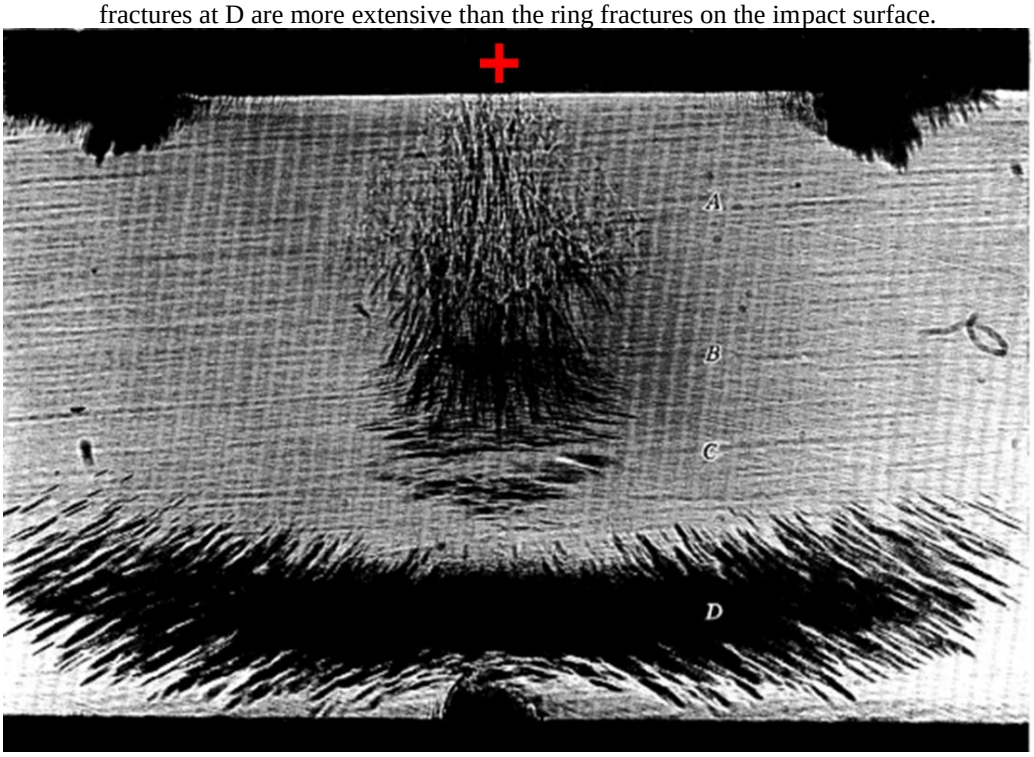

Source: Adapted from BRUNTON (1966).

The Rayleigh surface waves are confined to the surface and attenuate at a lower rate compared with surface bulk waves. The Rayleigh wave has both vertical and horizontal components, and the depth to which the Rayleigh wave penetrates depends on its wavelength which, in turn, depends on the impact velocity and the drop radius. These waves can introduce surface roughness or damage to the surface, which can be later exploited by lateral jetting (see Section 2.3.4), resulting in material loss and further extension of cracks (JACKSON and FIELD, 2000).

The velocities of these waves depend on the properties of the target, mainly elastic modulus, Poisson's ratio, and density. The fracture can take place in the solid target due to the passage of stress waves having high amplitudes of sufficient duration, exceeding the dynamic fracture strength of the target. Stress waves can also interact with microstructural discontinuities resulting in the formation of high tensile stress due to stress concentration, and, therefore, their propagation is considered one of the main mechanisms with which high-speed droplet impact can cause failure (IBRAHIM and MEDRAJ, 2020).

2.3.4 Lateral jetting

The time for the shock wave to overtake the contact edge is mere fractions of a microsecond after the initial impact and depends upon the impact velocity, the shock-compensated shock wave velocity in the water, and the radius of the impacting drop. When it happens, a free surface is generated behind the shock front and decompression can occur with release waves propagating from the free surface towards the center of the drop and lateral jetting spreading outwards from the impact site (Figure 12). Then, the pressure of the compressed water quickly reduces from the "water hammer pressure" to the Bernoulli stagnation pressure (P_i), Equation 4, which can be an order of magnitude lower (COAD, 1997).

$$P_i = \frac{\rho V^2}{2} \tag{4}$$

Figure 12 – Post-impact schematic of a water droplet before and after the water jetting process. Note the change in the position of the contact edge.

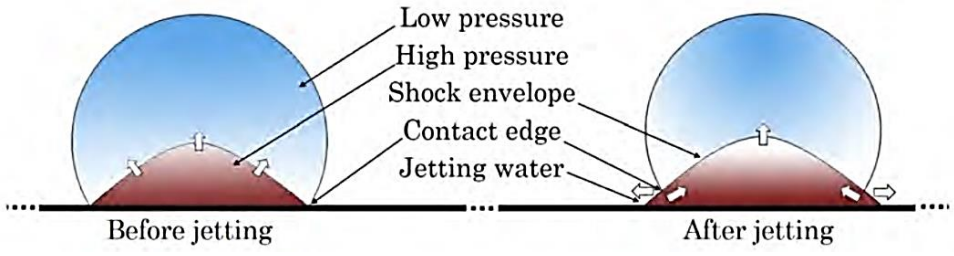

Source: O'CARROLL (2018).

In the event of compression and decompression occurring during the impact event, the velocity generated to push the water out from the center of the droplet to its sides (jetting) can be several times the impact velocity of the droplet. JENKINS and BOOKER (1960) measured the average velocity of lateral jetting for a 2 mm water droplet over a range of impact velocity of 100 to 1140 m/s (Figure 13). For an initial velocity of 100 m/s, the jetting velocity was approximately 600 m/s already.

Figure 13 – Lateral jetting velocity and its ratio to impact velocity for a 2 mm droplet.

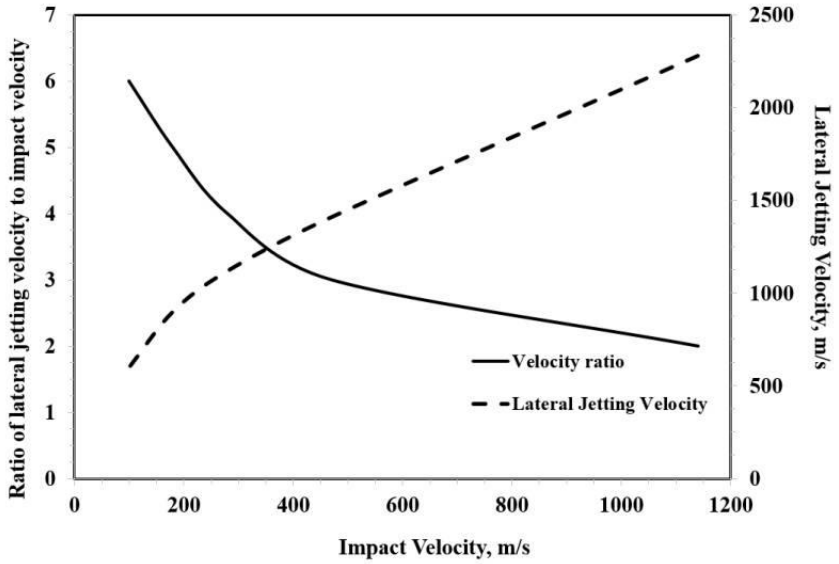

Source: IBRAHIM and MEDRAJ (2020), adapted from JENKINS and BOOKER (1960).

From a tribological point of view, and because of this high velocity, lateral jetting plays an important role in the initiation of erosion damage as it can potentially tear surface irregularities (IBRAHIM and MEDRAJ, 2020). Lateral jetting causes shear stress at the surface and can exploit surface asperities that arise from the surface roughness or damages introduced by the Rayleigh surface waves, resulting in material loss and further extension of cracks (GRUNDWÜRMER et al., 2007), as demonstrated in Figure 14. Therefore, surface quality and roughness play a very important role in the initiation of erosion damage.

Figure 14 – Erosion process by water jetting: (a) water droplet impact, and subsequent water jetting, (b) water jetting meets a surface asperity, pushing the prone material and creating cracks, (c) crack propagating into a cavity, (d) Shear failure of prone material.

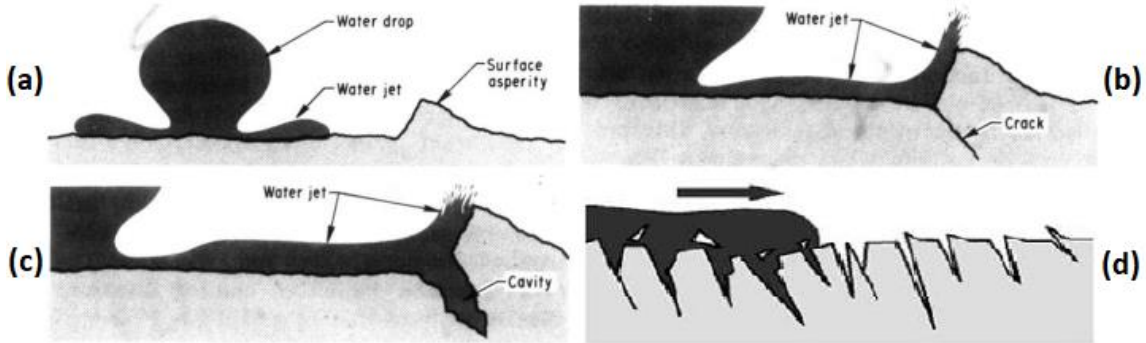

Source: (a-c) HEYMANN (1970a) and (d) O'CARROLL (2018).

2.4. DYNAMICS OF DROPLET IMPACT ON SOLID SURFACES

The impact of liquid droplets on a flat, solid surface is a subject of scientific interest due to the highly dynamic and complex nature of the impacting droplet structure. Advancements in novel measurement technologies and high-speed cameras have allowed these areas to be studied in detail, as presented in Figure 15, becoming widely growing areas of interest. The applications of such studies are many since droplet impacts can erode steam and wind turbine blades, and scour aircraft. In nature, droplet impacts can erode soil, compact snow, disrupt hummingbird and mosquito flight, and damage the surfaces of leaves (MITCHELL et al., 2019).

Figure 15 – High-speed images of a 2.9 mm diameter water droplet impacting at 2.1 m/s. The time between images is 100 μs. The image progression starts from the top left side and proceeds downwards, then to the right.

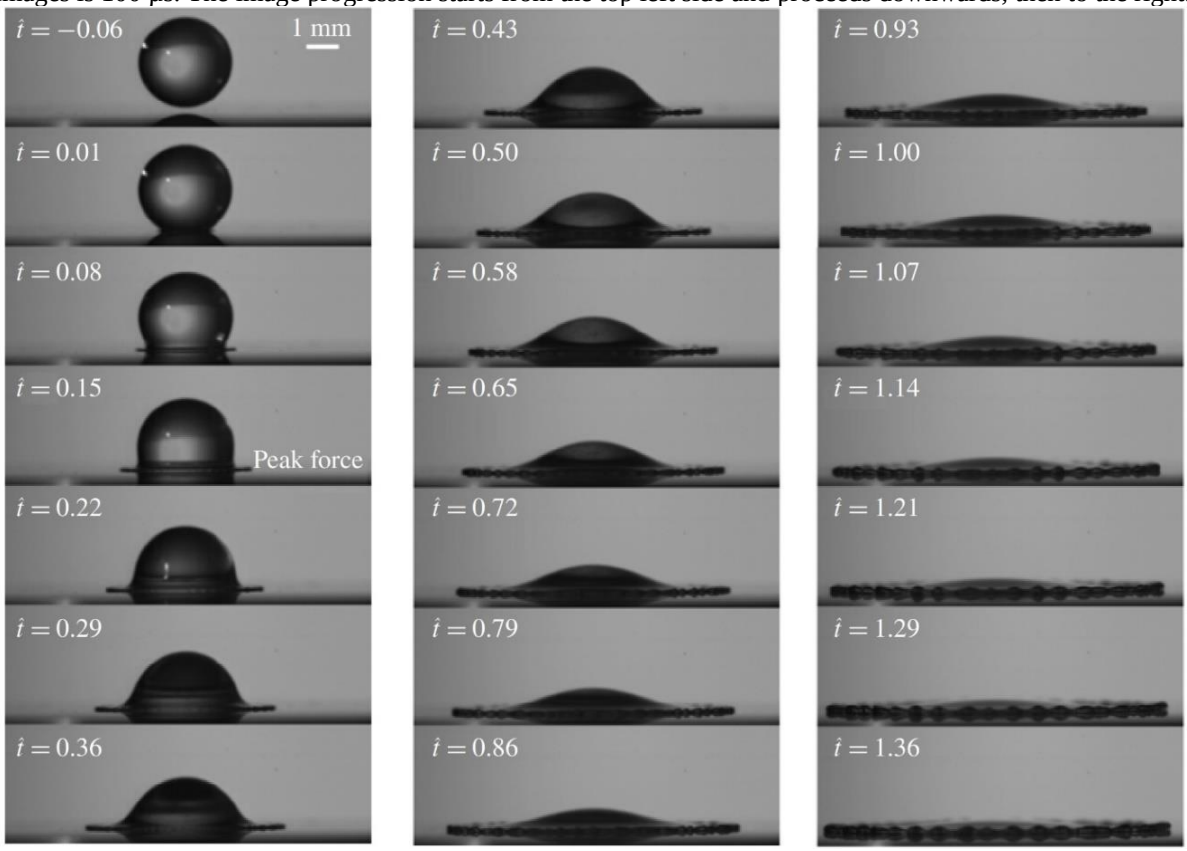

Source: MITCHELL et al. (2019).

The force-time history associated with the droplet impact is of considerable importance since it characterizes the time scale over which an object will experience the impact force and the resulting impulse (i.e., change in momentum). Similarly, in designing material processing applications, the force-time history is essential to characterize material erosion since it provides an evolution of the time-dependent loading. This allows, for example, the calculation of stresses and strains experienced by the solid. For typical millimeter-sized rain droplets, most of these phenomena happen on the order of milliseconds making observations difficult for the human

eye. Due to their rapid deformation and potentially destructive nature, high-speed droplet impacts are inherently difficult to image and pose significant measurement challenges (MITCHELL et al., 2019).

The study of the characteristics of the impact pressure caused by droplet-solid impact and its consequent temporal and spatial stress and strain fields in the solid received considerable attention during the 1960s throughout the 1980s, when the interest in developing rain erosion resistant materials was high in the aeronautical industry, and although many analytical and numerical models were developed, the main difficulty facing the definitive characterization of the loading and the stress field in a droplet impact, comprehending the coupled liquid-solid interaction encountered in a water droplet erosion problem, remained an obstacle (IBRAHIM and MEDRAJ, 2020).

A growing interest in the theoretical analysis, experimental research, and numerical simulation of droplet impact force has been stimulated in recent years by the required comprehensive understanding of the collision phenomenon (ZHANG et al., 2019). Enabled by advancements in high-speed photography and improved measurement techniques, several empirical studies allowed these phenomena to be comprehended in more extensive detail. These studies reveal that the impact force is characterized by a rapid rise to a maximum, followed by a much more gradual decay to zero force, as presented in Figure 16. As might be intuitively surmised, existing studies indicate that the peak force increases with increased droplet diameter, liquid density, and/or impact velocity (MITCHELL et al, 2019).

Figure 16 – Impact force evolution and corresponding images of a water droplet impacting a solid surface.

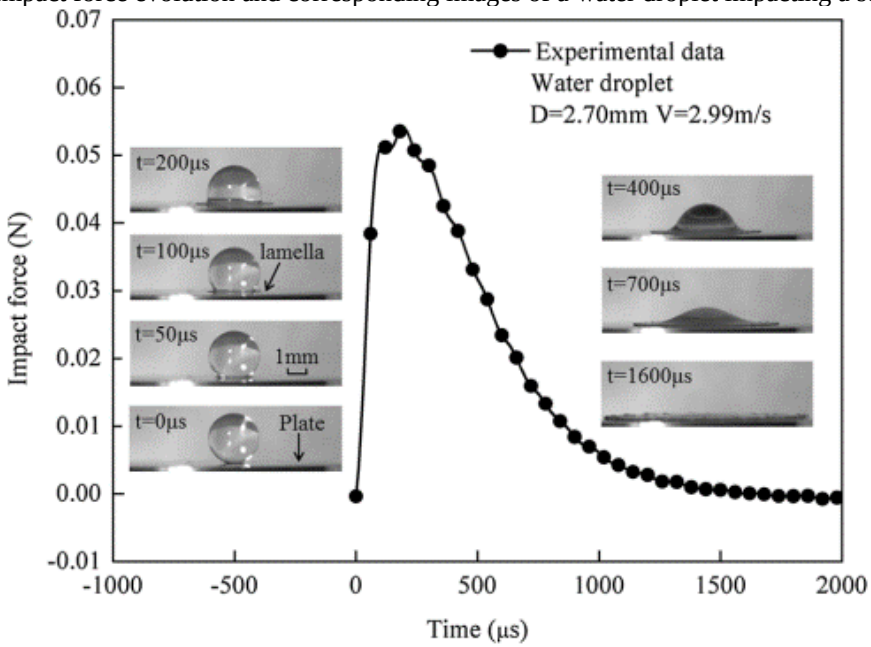

Source: ZHANG et al. (2017).

LI et al. (2014) studied the characteristics of the impact forces of water droplets and the influences of impact velocity and diameter on impact forces (Figure 17). Considering the droplet size, they found its influence on erosion is dependent on impact time duration (total time in which a droplet imparts a normal force), which decreases with the rise in impact velocity and increases with increased droplet diameter, further indicating that the impact pressure is the key factor to material erosion when impact velocity is taken as the influence factor.

Figure 17 – Force and time durations for (a) a 2.96 mm diameter droplet with different impact velocities; (b) several water droplets with the same impact velocity of 2.80 m/s and different diameters.

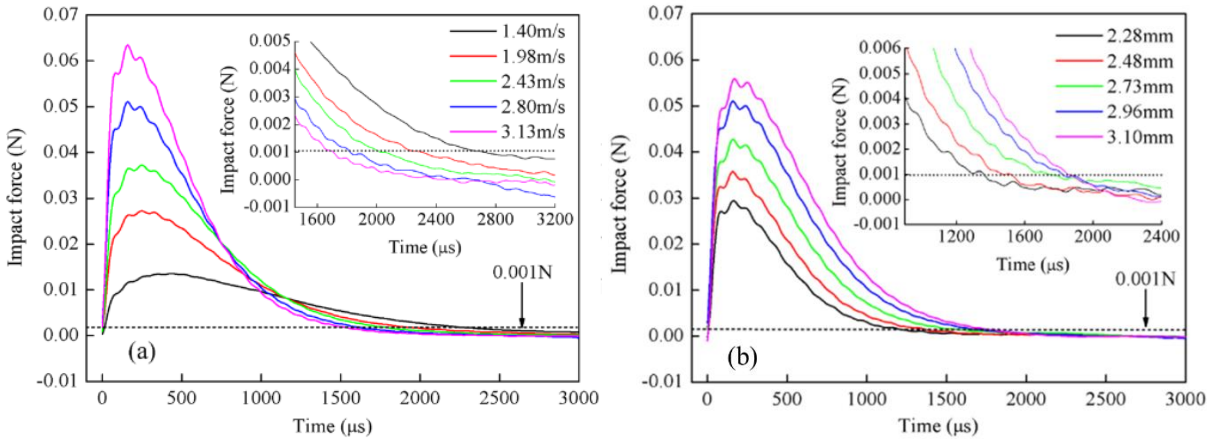

Source: Adapted from LI et al. (2014).

ZHANG et al. (2017), through experimentally validated numerical simulations, disclosed that in the inertia-dominated zone – when Reynolds number (Re) is larger than 230, dimensionless peak force remains constant, which indicates that the effect of viscosity could be neglected and inertial force dominates the impact process. Additionally, in the inertia-dominated zone, a universal curve of dimensionless impact force exists; in other words, dimensionless force is independent of Reynolds and Weber (We) numbers, and can be calculated according to the expression:

$$F_p = 0.84\rho V^2 D^2 \tag{5}$$

where ρ is the density of the solid, V is the impacting velocity and D is the droplet diameter.

GORDILLO et al. (2018) studied the temporal evolution of the shape and impact force of impacting drops over a wide range of Re numbers ($10^{-1} < \mathrm{Re} < 10^{4}$), providing a quantitative description of the maximum force and the peak time as a function of Re across inertial, viscous and viscoelastic regimes. MITCHELL et al. (2019) created a single model equation capable of representing the droplet force profile along its entire load span and across a wide range of Reynolds and Weber numbers. They also found that the force profiles are invariant concerning Weber number and that for high Reynolds flows, the only influential parameters for droplet impact are liquid density, impact velocity, and droplet diameter. ZHANG et al. (2019) studied

the effects of the droplet shape on its impact force and erosion effects and found that as the horizontal–vertical ratio of the droplets increases (i.e. the droplet becomes “wider”), the peak impact force increases by a power function trend and the time to reach the collision force peak decreases.

2.5. MODELLING AND PREDICTION OF LIQUID IMPINGEMENT EROSION

Generally, modeling water droplet erosion involves the development of mathematical models that can predict erosion initiation and rate of progression. This breaks down mainly into three tasks: characterization and evaluation of the intensity of the erosive environment in terms of impact loading, definition and measurement of the relevant target properties and their response to impact, and adoption of representative failure criteria. Figure 18 presents a general schematic of the formulation of rain erosion prediction models (IBRAHIM and MEDRAJ, 2020).

Figure 18 – General schematic for the formulation of a simple erosion prediction model.

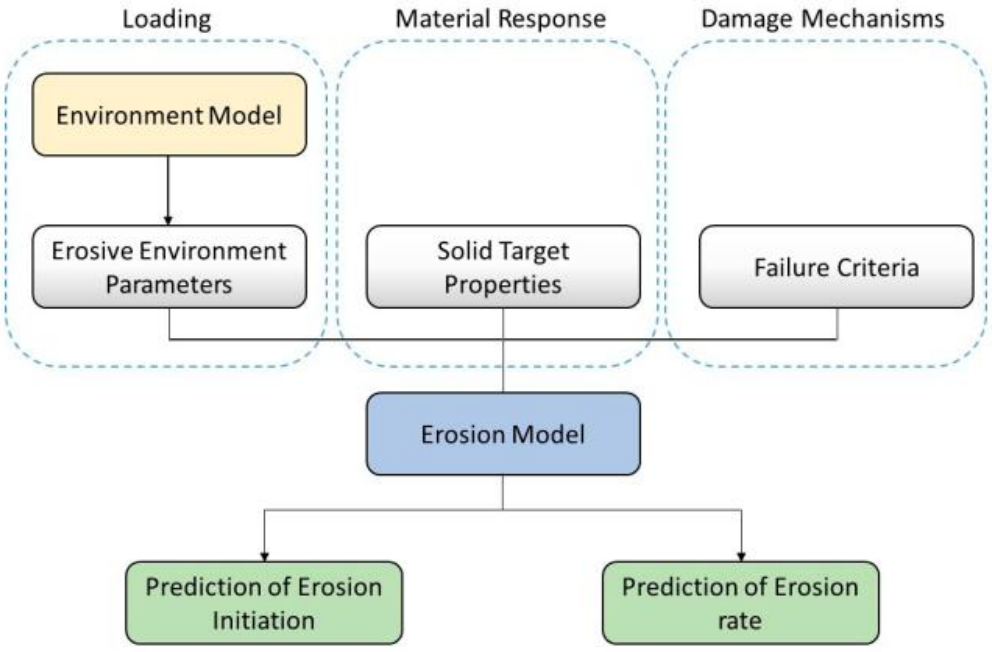

Source: IBRAHIM and MEDRAJ (2020).

The environment model represents all the parameters that relate to the loading characteristics generated by the impacting object. For rain erosion, these inputs could be the droplet size and shape, the impact velocity and angle, and the frequency of impact, among others, which relate in a larger sense to the meteorological data in a certain location, such as rainfall rates and the ensuing droplet size distribution. Many analytical and numerical models were developed from the 1960s onwards to characterize the impact pressure distribution and

stresses in the solid. A comprehensive review of the initial efforts (1960s – 1980s) can be found in LESSER and FIELD (1983) and LESSER (1995), as well as in the previous Section 2.4 for an overview of the most recent developments of the last decade.

Besides the obstacle that is facing the characterization of the loading and the stress fields, the coupled liquid-solid interaction in the water droplet erosion problem has presented another issue, which is the proper selection of the material properties pertaining to the resistance to water droplet impact erosion (i.e., erosion strength). Many attempts were made to use different material properties such as strength (yield or ultimate), hardness, toughness, hardenability, and ultimate resilience to represent erosion resistance (IBRAHIM and MEDRAJ, 2020). From those attempts, it became evident that the resistance to rain erosion has some qualitative correlation with hardness, tensile strength, and strain energy. In some cases, very good correlations have been obtained between erosion resistance and various properties within a specific class of materials, but not between different classes (PREECE and MACMILLAN, 1977), meaning that the material properties that would make a metal resistant to erosion are very different to a polymer's.

For polymeric materials, a key finding is that the acoustic properties play a vital role in their ability to resist erosion due to repeated high-velocity droplet impacts. The ability of the material to damp out the impact energy and quickly recover is essential for its performance. The recovery of a material has two aspects: one being the level of recovery that can occur and the second being how fast it can occur. Due to the small impact frequency, the long-term (viscoelastic) recovery is not as significant as the short-term (elastic) impact frequency as an indicator of material erosion durability. A reduction in the acoustic impedance mismatch relative to the water is also desirable, as it will reduce the water-hammer pressure generated during an impact event. In the same manner, a hardness reduction is desirable as, for more viscous polymers, the rigid nature of a hard surface does not lend to good performance as observed in metals (O'CARROLL, 2018). The coating morphological parameters, such as the surface roughness and the air voids contained in its interior (MISHNAEVSKY et al., 2019; DOAGOU-RAD and MISHNAEVSKY, 2020), also have a steep contribution to rain erosion resistance.

To overcome the multiplicity of associated parameters related to erosion resistance, the concept of erosion strength was first proposed by THIRUVENGADAM (1967) as a single numerical property value that would encompass other multiple mechanical properties, governing the volume of erosion in a particular material, and defined as the energy absorbed

per unit volume of material up to fracture under the action of the erosive forces in various environments. Despite its limitations, the concept of erosion strength has been adopted in several erosion models, as well as the one that is arguably the most used numerical erosion model for coated and uncoated fiber-reinforced composites, the Springer model (SPRINGER and YANG, 1975)

Taking it as an example, the Springer model is based on fatigue concepts such as the cumulative fatigue damage rule of Palmgren-Miner (detailed in Section 2.6.3) to ascertain the failure criteria of the evaluated materials. Employing the fatigue theorems established for the rain erosion of homogeneous materials, SPRINGER and YANG (1975) derived algebraic equations that describe the incubation period, rate of mass removal, and the total mass loss of the impacted solid, and that were consistent with experimental data, and could quantitatively predict the erosion of fiber reinforced materials under previously untested conditions. While other researchers before Springer, such as MOK (1969) and HEYMANN (1970b), also attempted to use fatigue similarities to develop erosion models, however, their models remained applicable to limited experimental data. Springer's models, on the other hand, were proven to correlate a considerable amount of erosion data, especially at subsonic impact speeds (IBRAHIM and MEDRAJ, 2020). The third and last component for formulating an erosion prediction model, the damage mechanisms and the failure criteria, will be more extensively detailed in Section 2.6.

2.6. FATIGUE LIFE PREDICTION AND THE EROSION FAILURE CRITERIA

The word fatigue originated from the Latin expression *fatigare* which means 'to tire'. The word fatigue has also become a widely accepted terminology in engineering vocabulary for the damage and failure of materials under cyclic loads, which can occur in many different forms. Mere fluctuations in externally applied stresses or strains result in mechanical fatigue. Cyclic loads acting in association with high temperatures cause creep fatigue; when the temperature of the cyclically loaded component also fluctuates, thermomechanical fatigue (i.e., a combination of thermal and mechanical fatigue) is induced. Recurring loads imposed in the presence of a chemically aggressive or embrittling environment give rise to corrosion fatigue. The repeated application of loads in conjunction with sliding and rolling contact between materials produces sliding contact fatigue and rolling contact fatigue, respectively, while

fretting fatigue occurs as a result of pulsating stresses along with oscillatory relative motion and frictional sliding between surfaces (SURESH, 1998).

Fatigue analysis procedures for the design of modern structures rely on techniques, which have been developed over the last 100 years or so. Initially, these techniques were relatively simple procedures that compared measured constant amplitude stresses (from prototype tests) with material data from test coupons. These techniques have become progressively more sophisticated with the introduction of strain-based techniques to deal with local plasticity effects, procedures to deal with variable amplitude stress responses, methods to predict how fast a crack will grow through a component, and techniques to deal with even the occurrence of stresses in more than one principal direction, such as multi-axial fatigue (BISHOP and SHERRATT, 2000).

2.6.1 The stress-life approach and the S-N curve

Once a local stress-time or strain-time history has been established, such as for an impacting rain droplet, a fatigue analysis method must be selected for the point likely to be critical. The usual stages of fatigue, illustrated in Figure 19, demonstrate that total fatigue life is considered to be made up of a crack initiation phase (sometimes referred to as incubation period) and a crack propagation phase. The proportion which each contributes will vary with the geometry, the loading, and especially with the material. Most finite element analysis (FEA) based fatigue packages have three main life prediction methods available: Stress-Life (S-N, nominal stress, or total life), Strain-Life (Local-Stress-Strain, Crack-Initiation, Manson-Coffin or Critical-Location Approach - CLA) and Crack-Propagation (usually described using linear elastic fracture mechanics), which together covered 95% of all fatigue design calculations at the start of the 21st century (BISHOP and SHERRATT, 2000).

Figure 19 – An idealization of the fatigue design process, and the fatigue life stages.

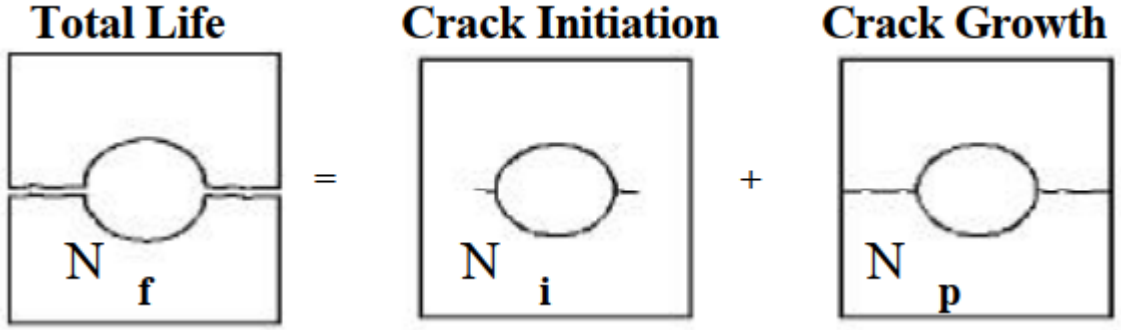

Source: BISHOP and SHERRATT (2000).

The Stress-Life approach assumes that all stresses in the component, even local ones, always stay below the elastic limit. It is the oldest of the three main methods, dating to the 19th century, and is still suitable when the applied stress is nominally within the elastic range of the material and the number of cycles to failure is large. Thus, the nominal stress approach is therefore best suited to problems that fall into the category known as high-cycle fatigue (HCF). The situation where the nominal stress method does not work well is in the low-cycle fatigue (LCF) region, where the applied strains have a significant plastic component. In this region, a strain-based methodology must be used instead (BISHOP and SHERRATT, 2000).

Considering impinging rain droplets impacting a solid surface, it is expected that the very impacted surface will be the region where the highest stresses are observed, and where fatigue wear will initiate. This is not always the case, as shown in MISHNAEVSKY et al. (2019), where it was observed that the damage very often starts from large defects within the coating. FEA results from studies such as AMIRZADEH et al. (2017b) and DOAGOU-RAD, MISHNAEVSKY, and BECH (2020), additionally demonstrate that, as expected, the stresses within the coating/surface layers remain well within the elastic limit of their respective materials. Consequently, failure is expected to occur at a high number of impacts, suggesting that a high-cycle fatigue approach must be adopted, for which the stress-life method would be appropriate.

The stress-life approach to fatigue was first introduced in the 1860s by August Wöhler (WÖHLER, 1860). Conducting systematic investigations of fatigue failure, he established a rotating bending testing station (conceptually the same apparatus widely used today for cyclically stressing metals) where he observed that the strength of steel railway axles subjected to cyclic loads was appreciably lower than their static strength. This empirical method has found widespread use in fatigue analysis, mostly in applications where low-amplitude cyclic stresses induce primarily elastic deformation in a component that is designed for long life, i.e., in the HCF applications. His work led to the characterization of fatigue behavior in terms of stress amplitude-life (S-N) curves and to the concept of a fatigue “endurance limit”, which characterizes the applied stress amplitude below which a (nominally defect-free) material is expected to have an, supposedly, infinite fatigue life (SURESH, 1998).

To generate a S-N curve several identical specimens are tested to total separation and the number of cycles needed is recorded as N. Load, not stress, is kept constant during the test. For each specimen, a nominal stress, σ, is calculated from simple elastic formulas and the

results are plotted as the un-notched S-N diagram (Figure 20), a basic material property. N is always plotted on the x-axis, and a logarithmic scale is used, while the y or σ axis may be linear or logarithmic (BASQUIN, 1910).

Figure 20 – Typical S-N diagram showing the variation of the stress amplitude for fully reversed fatigue loading as a function of the number of cycles to failure for ferrous and nonferrous alloys. The solid line illustrates the behavior observed for mild steels and other materials that harden by strain-aging, while the dashed line illustrates the behavior of aluminum alloys and other materials that do not generally exhibit a fatigue limit.

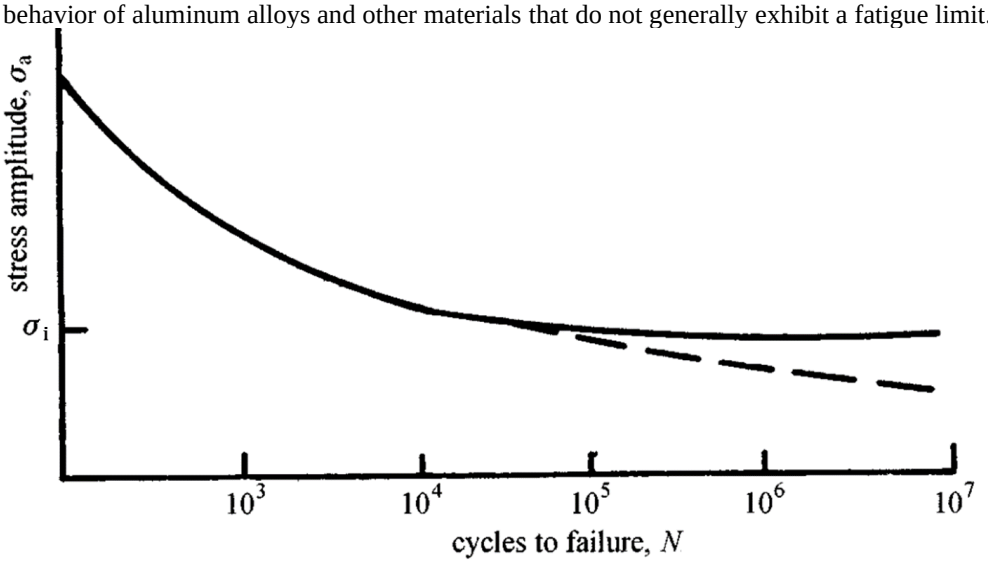

Source: Adapted from SURESH (1998).

When the S-N curve is drawn on a log-log scale, with the true stress amplitude plotted as a function of the number of cycles or load reversals to failure, a linear relationship is commonly observed in the finite-life region (10^4 to 10^6 cycles), and is known as the Basquin equation (BASQUIN, 1910):

$$\sigma_a = \sigma'_f (N)^b \tag{6}$$

The resulting expression relates the stress amplitude, σ_a, in a fully-reversed, constant amplitude fatigue test to the number of cycles to failure, N. σ'_f is known as the fatigue strength coefficient, which relates to the intercept on the y-axis when N equals 1 (which, to a good approximation, equals the ultimate tensile strength, σ_u, corrected for necking, in a monotonic tension test for most metals), and b is known as the fatigue strength exponent or Basquin exponent, which relates to the slope of the curve and, for most metals, is in the range of -0.05 to -0.12. It is worthwhile to note that Equation 6 is valid only for zero mean stress scenarios (SURESH, 1988). Another characteristic inferred from the S-N curve of a material is the endurance or fatigue limit, σ_i, which is the stress amplitude at the area of the curve known as the "knee point" and the threshold between the finite and the infinite fatigue life regions. These parameters and their relation to S-N data are presented in Figure 21.

Figure 21 – Fatigue test results regressed to Basquin`s law, with its parameters outlined. The blue error bounds illustrate the uncertainty in obtaining the endurance limit.

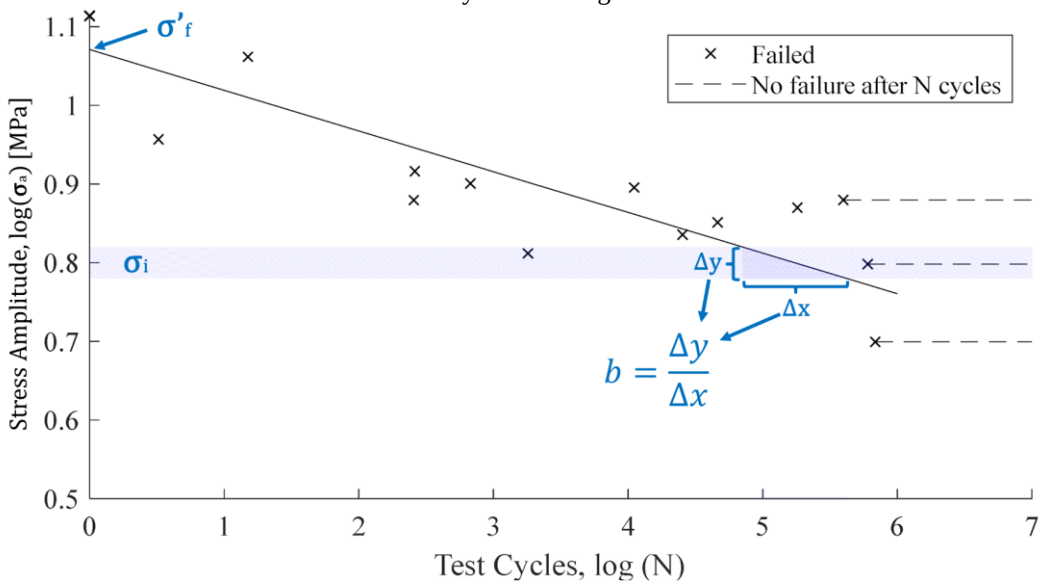

Source: Adapted from HERRING et al. (2021).

However, great care should be taken when dealing with stresses below the endurance limit because this can be sensitive to a variety of effects such as mean stresses and corrosion. Welds in ferrous metals, for instance, are assumed not to have a fatigue limit but experience a change of slope at around 10^7 cycles. For materials that do not exhibit a true fatigue limit, tests are usually terminated between 10^7 and 10^8 cycles, and the corresponding stress amplitude is then quoted as an endurance limit at the specified cycle number: Service failure may then occur if more than 10^8 cycles are applied (BISHOP and SHERRATT, 2000).

The simplest scenario where a single stress value can be straightly compared to the stress values on the S-N curve is the uniaxial state of stress. However, when multiple stress components are present, as in a multiaxial state of stress is present, the direct application of the S-N curve becomes impractical (AMIRZADEH et al., 2017b). In such instances, equivalent stress methodologies are commonly employed to consolidate multiple stress components into a single parameter for comparison with the S-N curve. Notable examples of such equivalent stress methods include the signed von-Mises stress, signed Tresca stress, and absolute maximum principal stress (AMPS) (BISHOP and SHERRATT, 2000). Von Mises and Tresca stresses are inherently positive, which poses challenges in preserving the alternating nature of stress-time history. To mitigate this, when utilizing Von Mises or Tresca stresses, the sign of the stress signal is determined based on the largest principal stress, considering its absolute value (AMIRZADEH et al., 2017b). Although they are popular for stress analyses, Von Mises and Tresca are not recommended for fatigue analyses as they are non-directional, whereas fatigue cracks are directional (BISHOP and SHERRATT, 2000). As such, in this study, the AMPS is

adopted as the approach to address multiaxial stress conditions in the fatigue damage calculations, as recommended by BISHOP and SHERRATT (2000) and previously used by AMIRZADEH et al. (2017b).

2.6.2 Fatigue life and rain erosion prediction

The process of rain-induced erosion can be considered a case of fatigue damage initiation and evolution as it involves repeated low-stress loadings that cause failure over an extended period. Fatigue properties of materials are usually expressed in the form of S-N curves, showcasing the stress amplitude versus the number of cycles to failure. Similarly, liquid impact erosion behavior of materials has been presented as erosion endurance curves, i.e., the impact velocity versus the number of impacts either to complete the incubation period or to increase the erosion depth by a certain amount (AMIRZADEH et al., 2017b). THOMAS and BRUNTON (1970), while investigating the mechanisms of erosion under drop impingement, found great similarities between the S-N curves determined in a standard fatigue test and the erosion velocity/endurance curves set by the incubation period onset, as presented in Figure 22. For example, in the case of mild steel, the erosion curves show an endurance limit similar to the one found in the S-N curve, while in the aluminum alloy, there is no such limit in the S-N curve and none in the erosion curves as well. It has also been reported by HATTORI, HIROSE, and SUGIYAMA (2010), in their study on cavitation erosion by liquid jet impact, that the conclusion of the erosion incubation period matches with macroscopic fatigue failure.

Figure 22 – Comparison of fatigue S-N curve (a) and erosion endurance curve (b) for the aluminum alloy HE 15. The crosses indicate the completion of the incubation period, and the open circles indicate when the erosion depth is increased by 100 μm.

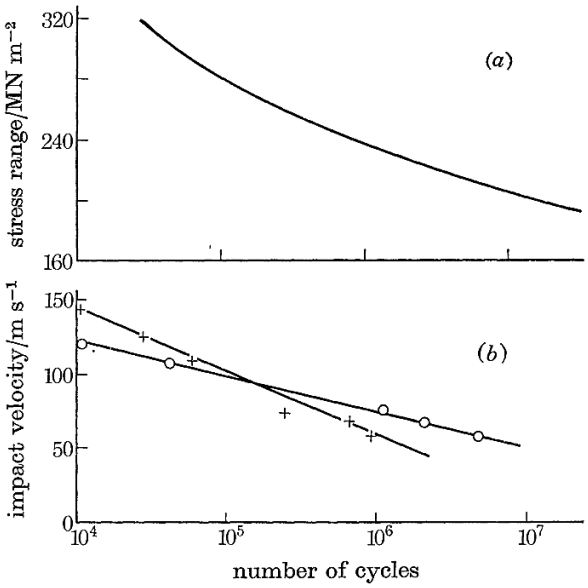

Source: THOMAS and BRUNTON (1970).

The use of fatigue life as an analog to erosion performance also makes up the basis of the Springer erosion model (SPRINGER and YANG, 1975), when it was established that the end of the incubation period can be ascertained by applying fatigue theorems to the rain erosion problem. The model requires specific coating and substrate material properties, such as speed of sound measurements, and fatigue properties such as the Wöhler constant, endurance limit, and the fatigue "knee", all characteristic parameters obtainable from S-N, or Wöhler curves. While being widely used, the Springer model suffers from its limited applicability, since its parameters, just by the model's concept, need to be first adapted to fit a certain set of empirical data. As such, fatigue testing of material samples will always be required before applying this model. The usage of a theoretical estimation of the impact stress for a 1-dimensional droplet (SPRINGER and YANG, 1975) also results in different impact loading values from the ones observed in experimental and computer simulation data (KEEGAN, NASH, and STACK, 2014).

The stresses produced by a single rain droplet impacting a coating material layer are usually not large enough to induce failure. However, the large number of drops impacting the surface will, over time, induce failure in the wind turbine blade surface. Rain droplets of different diameters, speeds, and shapes, striking the surface at different angles will generate different impact loadings, each affecting the impacted surface differently and providing varying contributions to fatigue buildup. When every impact or cycle contributes differently to failure, besides having to ascertain the ultimate point of fatigue failure, a rain erosion prediction model also needs to additionally account for how the fatigue damage evolves after every discrete impact event. For cases such as this, cumulative fatigue damage methods have been developed, such as the generally used Palmgren-Miner rule.

2.6.3 The Palmgren-Miner rule and cumulative fatigue damage

It is usual in fatigue testing for the fatigue loading to have a constant amplitude, with or without a mean offset. However, in engineering applications components are invariably subjected to varying cyclic stress amplitudes, mean stresses, and loading frequencies. The simplest extension of the constant amplitude case is one in which the stress amplitude changes from time to time, as in Figure 23. The loading history then consists of n_1 cycles of amplitude S_1, n_2 of S_2, n_3 of S_3, and so on. Usually, the pattern repeats after several stress values, S_n. The sequence up to S_n is then called a "block", and the target is to estimate how many of these

blocks can be applied before failure occurs. The rule generally used for this is the Miner or Palmgren-Miner hypothesis (PALMGREN, 1925; MINER, 1945). Considering first the n_1 cycles of S_1, if we have S-N data we can find the number of cycles of S_1 which would cause failure if no other stresses were present. Calling this N_1, the simplest assumption is then that n_1 cycles of S_1 use up a fraction n_1/N_1 of the life. Doing a similar calculation for all the other stresses and summing all the results gives the total damage fraction for one block. The reciprocal of this is then the life in blocks. Given as an equation this is:

$$\sum_{i=1}^{m} \frac{n_i}{N_i} = 1.0 \tag{7}$$

or, for the sequence illustrated in Figure 23, Equation 10 would become (BISHOP and SHERRATT, 2000):

$$\frac{n_1}{N_1} + \frac{n_2}{N_2} + \frac{n_3}{N_3} = 1.0 \tag{8}$$

Figure 23 – A typical block loading sequence.

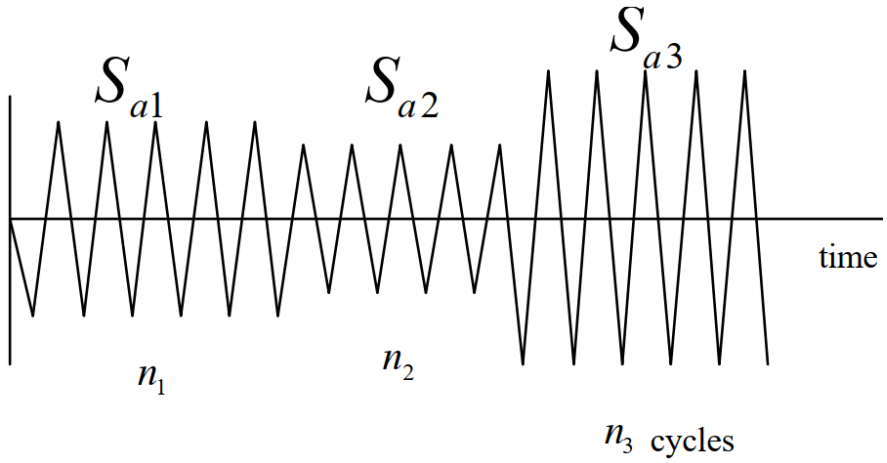

Source: BISHOP and SHERRATT (2000).

The summation is carried out over all stress amplitude values that are present in a stress-time history. Fatigue failure occurs when the damage index equals one. Note that, under the Miner's rule assumption, the damage index is not a physical parameter and is not necessarily related to the stiffness or strength of the material (AMIRZADEH et al., 2017b). Qualitatively, strength is not affected by fatigue, and mean fatigue life remains the same for each cycle type, thus, the order of load cycles is of no effect on the strength degradation life prediction, rendering the life estimate equal to that of Miner's sum (NIJSEEN, 2006).

Palmgren-Miner sum does not describe the accumulation of physical damage, but the target is to estimate how many of the loading blocks can be applied before the failure that is

defined using experimental S-N curves occurs. One should keep in mind that there are associated limitations for the Palmgren-Miner hypothesis, which revolves around it being:

1. Linear, i.e., it assumes that all cycles of a given magnitude do the same amount of damage, whether they occur early or late in life.
2. Non-interactive (sometimes referred to as sequential effects) i.e., it assumes that the presence of S_2 (and so on), does not affect the damage caused by S_1.
3. Stress-independent i.e., it assumes that the rule governing the damage caused by S_1 is the same as that governing the damage caused by S_2. This limitation is often misunderstood and is sometimes confused with limitation 2.

These assumptions are known to be faulty, but wide use of the hypothesis has shown that in most circumstances it gives acceptable results (BISHOP and SHERRATT, 2000). In the case of complex real-life stress signals, adjustments are necessary to translate them into the cycles used in the Palmgren-Miner hypothesis. For that, cycle counting algorithms can be used, such as the Rainflow cycle counting method.

2.6.4 The Rainflow cycle counting method

Real engineering components experience complex stress responses, and seldom, if ever, experience constant amplitude loading. Therefore, some type of cycle counting scheme must be employed to reduce a complex irregular loading history into a series of constant amplitude events. Taking the loading history presented in Figure 24 as an example, each cycle transition is equal to approximately 100 MPa but the overall transition of the peaks is over 400 MPa. It then needs to be decided what “cycles” of stress should be used. One approach would be to take the stress difference between adjacent peaks and valleys, which would result in many cycles of about 100 MPa. However, because fatigue behavior is non-linear, higher stress levels cause much higher fatigue damage, and the above approach would therefore grossly underestimate fatigue damage. A second, alternative approach would be to assume that the peak levels (400 MPa) are representative of the stress amplitudes; but if this amplitude were used for all cycles, then this approach would grossly overestimate damage (BISHOP and SHERRATT, 2000).

Figure 24 – Time history for an irregular loading response.

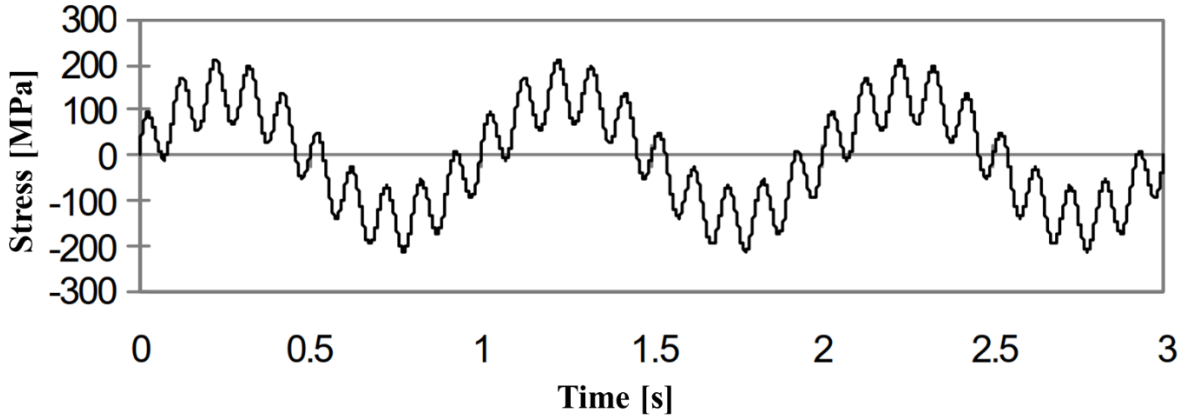

Source: Adapted from BISHOP and SHERRATT (2000).

The most accurate fatigue life estimates are obtained using an analysis based on the strain at the most highly stressed/strained locations, and the Rainflow counting algorithms are an essential part of these procedures (DOWNING and SOCIE, 1982). By identifying the overall trends in the response, whilst also keeping track of intermediate and small response cycles properly, Rainflow ranges have been widely used for estimating fatigue damage from random signals since MATSUISHI and ENDO (1968) first introduced the concept. Its name comes from its original cycle counting methodology of imagining the stress peaks as a series of pagoda roofs with rain dripping downwards (SURESH, 1998).

Due to the great importance of the Rainflow counting method, many different algorithms have been proposed in the literature. A constant between all these proposals is that the Rainflow counting method corresponds to the stable cyclic stress/strain behavior of a material in that all strain ranges counted as cycles will form closed stress/strain hysteresis loops, and those counted as half cycles will not. The range of a closed hysteresis loop is defined by its highest and lowest point, i.e., by the pair of a local maximum and minimum in the strain function (RYCHLIK, 1987).

The procedure for Rainflow cycle counting is relatively straightforward, and the most common procedure, as outlined by BISHOP and SHERRATT (2000), is:

1. Extract the peaks and valleys from the stress signal, so that all points between adjacent peaks and valleys are discarded.
2. The beginning and the ending of the signal are forced to have the same value. This can be done in several ways but the simplest is to copy the starting point to the end of the signal. In the example shown in Figure 25(a), point 9 is a copy of point 1, and is not included in the original signal history.

3. Find the highest peak and reorder the signal so that this becomes the beginning and the end. The beginning and end of the original signal must be joined together.
4. Start at the beginning of the sequence and select consecutive sets of 4 peaks and valleys, applying the following rule: If the middle segment is shorter than the first and the third, then it is extracted as a Rainflow cycle. In the example presented in Figure 25(a), segment 3-4 is shorter than 2-3 and 4-5, and segment 7-8 is shorter than 6-7 and 8-9. They are counted and removed from the next iteration in Figure 25(b).
5. If no cycle is counted then a check is made on the next set of 4 peaks, i.e., peaks 2 to 5, and so on until a Rainflow cycle is counted. Every time a Rainflow cycle is counted the procedure is restarted from the beginning of the sequence (Figure 25(b)). Eventually, all segments will be counted as cycles and so for every peak in the original sequence, there should be a corresponding Rainflow cycle counted.

Figure 25 – Rainflow cycle counting for a load sequence. (a) In the first iteration, the cycles are counted, and their segments are extracted. (b) The cycle counting is restarted for the new loading sequence.

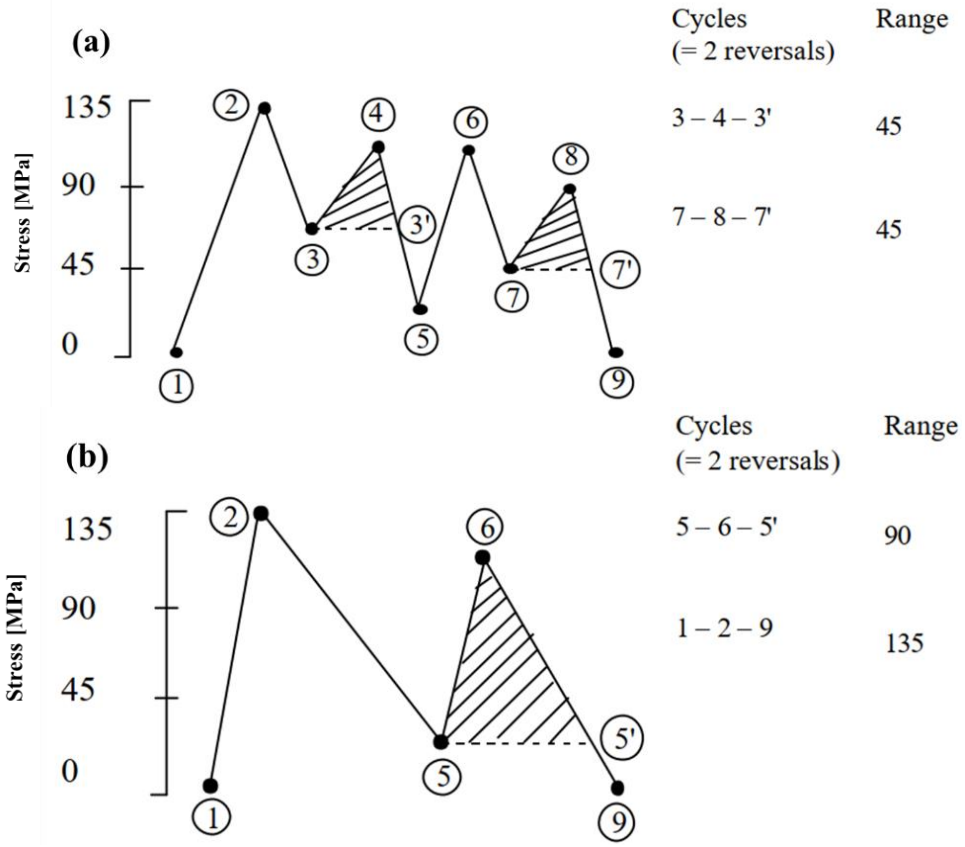

Source: Adapted from BISHOP and SHERRATT (2000).

As the Rainflow counting algorithm proceeds, it matches peaks and valleys to form closed hysteresis loops. When the algorithm reaches the end of the time-series data record, a series of unmatched peaks and valleys might remain unclosed and, therefore, are not counted by the algorithm. These so-called “half-cycles” typically include the largest peak and valley in

the record, and they may also include other large events. Thus, the potentially most damaging events (the largest cycles) contained in the time series are not counted by the classical formulation of the Rainflow algorithm. When pairing it with the Palmgren-Miner rule to assess the cumulative fatigue damage, several techniques have been proposed for handling these half-cycles in wind turbine applications. Some ignore them, some consider their damage contribution as half of a complete cycle (hence, their name), and others consider them as a full cycle, the latter being the most conservative approach (SUTHERLAND, 1999). The recommended practice is to treat all unclosed cycles as half-cycles and register their fatigue damage as half of an equivalent full cycle of the same range and mean stress characteristics (CRANDALL, MARK, and KHABBAZ, 1962; MADSEN, 1990; SUTHERLAND, 1999). Palmgren-Miner's equation is modified and employed in this study as:

$$\sum_{i=1}^{m} \begin{cases} \frac{n_i}{N_i} & if\ n_i\ is\ a\ full\ cycle \\ \frac{n_i}{2N_i} & if\ n_i\ is\ a\ half\ cycle \end{cases} = 1.0 \tag{9}$$

2.6.5 Mean stress correction and the linear Goodman relation

The Rainflow cycle's mean stresses cannot be directly used for fatigue analysis and must first be corrected for the nonzero mean stresses present in the signal. To account for nonzero mean stresses, many mean stress correction equations have been proposed. Among these, the linear Goodman relation is one of the most used (AMIRZADEH et al., 2017b).

Most of the descriptions of fatigue life and fatigue testing pertain to fully reversed fatigue loads where the mean stress of the fatigue cycle is zero. However, fully reversed stress cycles with zero mean stress are not always representative of many applications. The mean level of the imposed fatigue cycle is known to play an important role in influencing the fatigue behavior of engineering materials. Figure 26 presents a fatigue cycle of sinusoidal waveform with a nonzero mean stress. In this case, the stress range ($\Delta\sigma$), the stress amplitude (σ_a) and the mean stress (σ_m), are respectively defined as:

$$\Delta\sigma = \sigma_{max} - \sigma_{min} \tag{10}$$

$$\sigma_a = \frac{\sigma_{max} - \sigma_{min}}{2} \tag{11}$$

$$\sigma_m = \frac{\sigma_{max} + \sigma_{min}}{2} \tag{12}$$

The mean stress can also be characterized in terms of the load ratio, R, as:

$$R = \frac{\sigma_{min}}{\sigma_{max}} \tag{13}$$

where R = –1 is considered for fully reversed loading, R = 0 for zero-tension fatigue, and R = 1 for a static load (SURESH, 1988).

Figure 26 – Visual representation of a stress signal over time, outlined with the stress parameters that affect fatigue life.

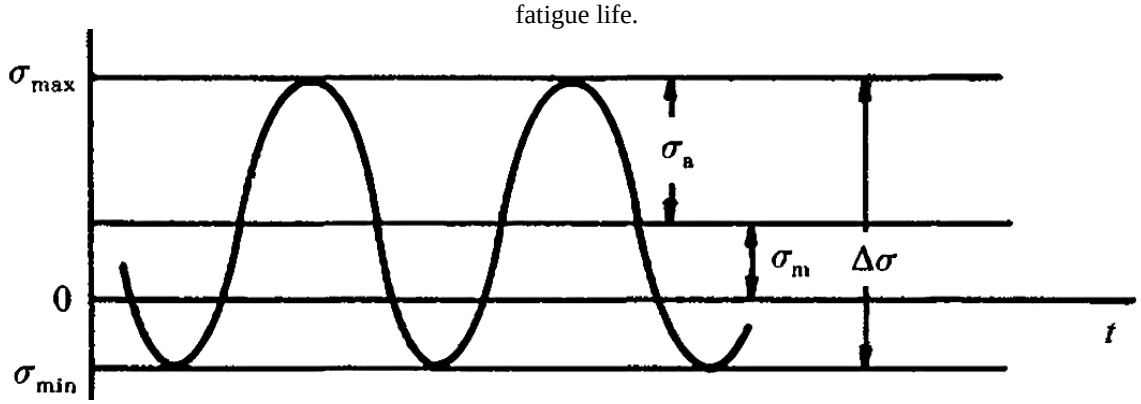

Source: SURESH (1988).

A simple way to account for the mean stress is to assume that it reduces the allowable applied amplitude of stress linearly. It is reasonable to expect that once the mean stress reaches the ultimate tensile strength of the material, no fatigue load can be carried at all. If the fatigue strength is known at any mean stress, the linear relation can then be defined. This is known as Goodman's Relation. As an empirical formula, the Goodman approach has been relatively successful, but there are limitations. Above a certain mean stress, combining the mean stress with the fatigue loading takes the material beyond its yield stress at every stress peak. To allow for this, a cut-off line can be introduced, resulting in the Modified Goodman Relation (BISHOP and SHERRATT, 2000).

The modified Goodman relation corrects the amplitudes of the Rainflow counted signal according to their mean stress using the following relationship:

$$\sigma'_a = \sigma_a \left[1 - \left(\frac{\sigma_m}{\sigma_u}\right)^{m_1}\right] \tag{14}$$

where σ'_a is the corrected amplitude, σ_a is the original stress amplitude, σ_m is the mean stress, σ_u is the ultimate tensile strength, and m_1 is an arbitrary empirical constant. If fatigue tests at multiple mean stresses are available, m_1 can be calculated. Otherwise, the most conservative assumption is to have m_1 equal to 1 (SURESH, 1988). Note that the ultimate tensile strength in

Equation 14 should be substituted with the ultimate compressive strength for negative mean stresses (AMIRZADEH et al., 2017). Once the Rainflow stress amplitudes have been corrected, they can be related to a material's S-N curve and be applied to Palmgren-Miner's rule for fatigue damage accumulation.

2.7. EXPLICIT DYNAMIC MODELLING

This chapter is dedicated to explaining the formulation behind the computational model, providing some notions regarding its governing equations, meshing methods, boundary conditions, and numerical material characterization. All modeling in this research is undertaken with the finite element software ANSYS and its Explicit Dynamics solver. Some of the information presented in the upcoming sections is exclusive to this solver and its approach to modeling impact events. ANSYS Explicit Dynamics is a transient explicit dynamics Workbench application that uses the ANSYS Autodyn solver. It can perform a variety of engineering simulations, including the modeling of nonlinear dynamic behavior of solids, fluids, gases, and their interaction, offers a wide range of pre and post-processing tools, as well as the ability to integrate the model inputs and output into other analyses (ANSYS, 2019).

2.7.1 Explicit dynamics

An explicit dynamics analysis is used to determine the dynamic response of a structure due to stress wave propagation, impacts, or rapidly changing time-dependent loads. Momentum exchange between moving bodies and inertial effects are usually important aspects of the type of analysis being conducted. This type of analysis can also be used to model mechanical phenomena that are highly nonlinear. Nonlinearities may stem from the materials (hyperelasticity, plastic flows, failure), from contact (high-speed collisions and impact), and from geometric deformation (buckling and collapse). Events with time scales of less than 1 second (usually at an order of 1 millisecond) are efficiently simulated with this type of analysis, and although events that last more than 1 second can be modeled, long run times can be expected (ANSYS, 2019).

The explicit dynamics method is still similar to the classical implicit finite element methods in several ways. For both, the structural bodies analyzed must be discretized into elements that jointly represent the complete body. However, the approach utilizes an explicit

(rather than iterative) method to solve the basic equation of motion solved by an implicit transient dynamic analysis:

$$m\ddot{x}^n + c\dot{x}^n + kx^n = f^n \tag{15}$$

where *m* is the system inertia load, *c* is the system damping load, *k* is the system stiffness load, and f is the external load, while x, $\dot{x}$ and $\ddot{x}$ are the displacement, speed, and acceleration, respectively. There, n is the given time step, and the premise of the solving process is to determine the displacement x^{n+1} at the time t^{n+1}. Conceptually, the difference between Explicit and Implicit dynamic solutions can be written as:

$$\text{Explicit:} \quad x^{n+1} = f(x^n, \dot{x}^n, \ddot{x}^n, x^{n-1}, \dot{x}^{n-1}, \dots) \tag{16}$$

where all these terms are known at this time state 'n' and therefore can be solved directly, whereas for an implicit approach the solution depends on unknown displacements, nodal velocities, and accelerations at the time state 'n+1' (KEEGAN, NASH, and STACK, 2014), becoming:

$$\text{Implicit:} \quad x^{n+1} = f(\dot{x}^{n+1}, \ddot{x}^{n+1}, x^n, \dot{x}^2, \dots) \tag{17}$$

Based on these values, the internal and external forces can be calculated and the accelerations can then be subsequently determined. These acceleration values can then be fed back into the equations for the next time step, initiating the next series of calculations (KEEGAN, NASH, and STACK, 2014).

The ANSYS Explicit Dynamics solution process is summarized in the following steps (ANSYS, 2019). First, at the first timestep when the initial impact is detected, the resultant motion of the node points will produce deformation in the elements of the mesh. The deformation results in a volume change (hence density) of the material in each element. The rate of deformation is used to derive material strain rates using various element formulations. Then, constitutive laws take the material strain rates and derive resultant material stresses. The material stresses are then transformed back into nodal forces using various element formulations. External nodal forces are computed from boundary conditions, loads, and contact (body interaction) and integrated into the calculation. The nodal forces are divided by nodal mass to produce nodal accelerations., which are integrated explicitly in time to produce new nodal velocities. The nodal velocities are integrated explicitly in time to produce new nodal positions. The solution process (or cycle) is then repeated until the user-defined time is reached. This strategy is resumed and outlined in the flowchart shown in Figure 27.

Figure 27 – Summary flowchart for the Explicit Dynamics solution process.

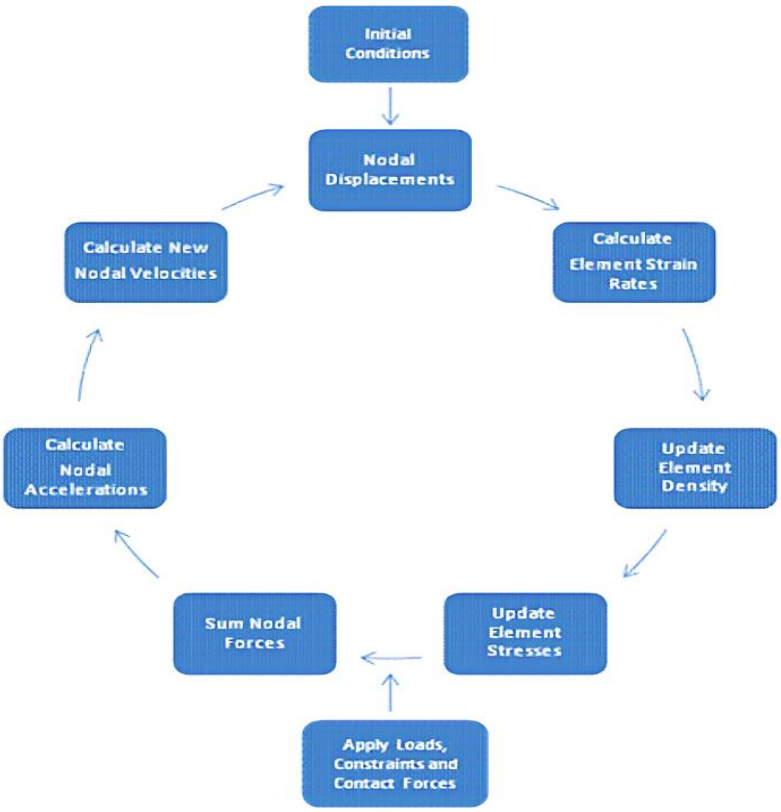

Source: ANSYS (2019).

2.7.2 Lagrangian and Eulerian reference frames

The classical approach to discretizing bodies of interest in finite element analyses is to represent the body with several smaller elements, defined by several nodes. The interactions and relations defined between these adjoining nodes and elements are what constitute the material behavior of the structure as a whole. Elements can take many shapes and forms and can be represented by varying numbers of nodes. The two most common forms of elements utilized for three-dimensional simulations are the hexahedral and tetrahedral, as shown in Figure 28 (KEEGAN; NASH; STACK, 2014).

Figure 28 – Hexahedral and Tetrahedral, common element types in Explicit Dynamics analysis.

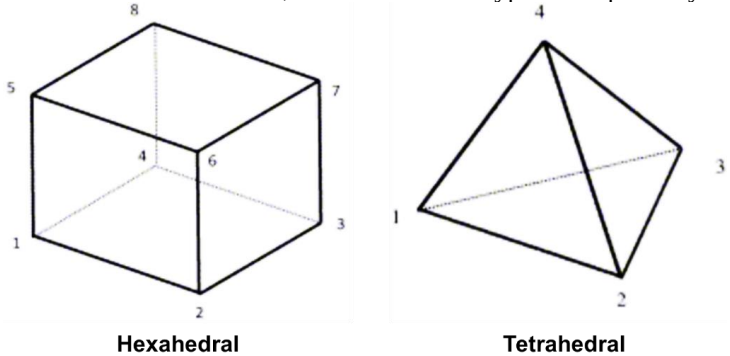

Source: ANSYS (2019).

By default, all bodies in an Explicit Dynamics analysis system are discretized and solved in a Lagrangian reference frame: The material associated with each body is discretized in the form of a body-fitted mesh, each element of the mesh representing a volume of material. The same amount of material mass remains associated with each element throughout the simulation, and if the material goes through deformation, so does the mesh (Figure 29a). Solving using a Lagrangian reference frame is the most efficient and accurate method to use for most structural models, however, in simulations where the material undergoes extreme deformations, such as in a fluid or gas flowing around an obstacle, the elements will become highly distorted as the deformation of the material increases. Eventually, the elements may become so distorted that the elements become inverted (negative volumes), and the simulation cannot proceed without resorting to numerical erosion of highly distorted elements (ANSYS, 2019). Such skewing can drastically reduce the accuracy of the modelling and additionally significantly increase the required computational power and time. Considering these drawbacks and limitations, alternative methods of discretizing and representing high-deformation bodies in simulations have been developed (KEEGAN; NASH; STACK, 2014), such as the Eulerian modeling approach and the Smoothed Particle Hydrodynamics (SPH) method (see Section 2.7.5).

Eulerian modeling approaches originate from computational fluid dynamic methods of modeling multiphase and liquid-solid interactions; however, it has also seen increasing use in structural impact simulations; through coupling it with classical finite element methods. Unlike the classic Lagrangian meshing methods whereby a mesh is attributed to the geometry of a body, a Eulerian meshing approach applies a mesh to a specified domain within which the body of interest will be present (either stationary or moving). The body within the domain is therefore not represented by a fixed mesh applied to its geometry; rather the body adopts the nodes within the domain as it moves or deforms within it. This means that when the body moves and deforms, the mesh that represents the geometry can be altered either by changing to different nodes or altering the shape of the domain mesh (Figure 29b). Different approaches to the method can make use of either or both techniques, however, the resulting benefit is that the mesh representing the body does not undergo excessive stretching or skewing, therefore avoiding the drawback associated with these effects (KEEGAN; NASH; STACK, 2014). Using a Eulerian reference frame is generally computationally more expensive than using a Lagrangian reference frame. The additional cost comes from the need to transport material from one cell to the next and to track in which cells each material exists. Each cell in the grid can contain one or more materials (to a maximum of 5 in the ANSYS Explicit Dynamics system), and the location and

interface of each material is tracked only approximately (to first-order accuracy) (ANSYS, 2019).

Figure 29 – Representation of (a) Lagrangian and (b) Eulerian reference frame approaches when material deformation is experienced. The green area in (b) represents the material within the Eulerian reference frame.

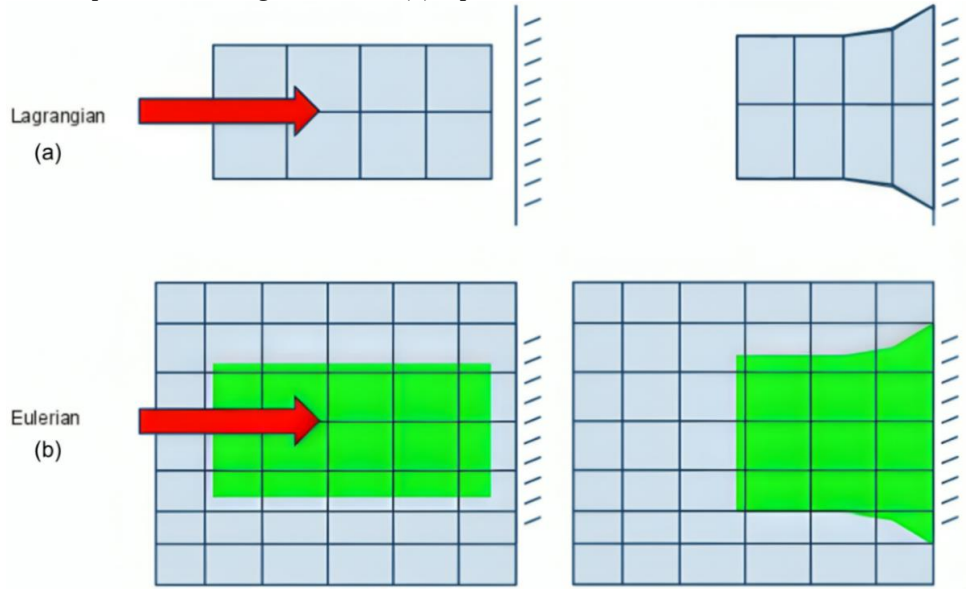

Source: ANSYS (2019).

2.7.3 Explicit time integration

The Explicit Dynamic solver uses a central difference time integration scheme (often referred to as the Leapfrog method). After forces have been computed at the nodes of the mesh (resulting from internal stress, contact, or boundary conditions), the nodal accelerations are derived by equating the acceleration. The advantages of using this method for time integration for nonlinear problems are that (1) the equations become uncoupled and can be solved directly (explicitly) with no requirement for iteration during time integration; (2) no convergence checks are needed because the equations are uncoupled; (3) no inversion of the stiffness matrix is required since all nonlinearities (including contact) are included in the internal force vector (ANSYS, 2019).

To ensure the stability and accuracy of the solution, the size of the timestep used in explicit time integration is limited by the Courant-Friedrichs-Lewy (CFL) condition:

$$\Delta t \leq f * \left[\frac{h}{C}\right]_{min} \tag{18}$$

where Δt is the time increment, f is the stability time factor (0.9 by default), h is the characteristic dimension of an element, and C is the local speed of sound in an element of the

material. This condition implies that the timestep must be limited such that a disturbance (stress wave) cannot travel farther than the smallest characteristic element dimension in the mesh in a single timestep. For example, for a mesh with a characteristic dimension of 1 mm and a material sound speed of 5000 m/s, the resulting stability time step would be 0.18 μs, and to solve this simulation to a termination time of 0.1 seconds would require 555,556 time increments (ANSYS, 2019). The timestep parameter is automatically corrected during the simulation in the ANSYS Explicit Dynamics module and is one of the most relevant factors to the total simulation time.

2.7.4 Shock equations of state

In physics and chemistry, an equation of state (EOS) is a thermodynamic equation relating state variables, which describes the state of matter under a given set of physical conditions, such as pressure, volume, temperature, or internal energy (PERROT, 1998). A general computational material model requires equations that relate stress to deformation and internal energy (or temperature). Hooke's law is the simplest form of an equation of state and is implicitly assumed when you use linear elastic material properties. Hooke's law is energy independent and is only valid if the material being modeled undergoes relatively small changes in volume (less than approximately 2%). If the material is expected to experience high volume changes during an analysis, an alternative equation of state should be used (ANSYS, 2019). There are several equations of state to describe different types of phenomena. If the impact between two bodies is being modeled, the Shock EOS options are the best methods to model the materials involved in the Explicit Dynamics environment.

The Rankine-Hugoniot relations describe the relationship between the states on both sides of a shock wave or a combustion wave (deflagration or detonation) in a one-dimensional flow in fluids or a one-dimensional deformation in solids. express the fact that the flux of mass, momentum, and energy must be continuous at a shock, whilst the pressure, density, and internal energy of the gas may not be continuous (BILLINGHAM and KING, 2000).

The Rankine-Hugoniot equations for the shock jump conditions can be regarded as defining a relation between any pair of variables such as density, pressure, energy, particle velocity, and shock velocity. In many dynamic experiments, it has been found that for most solids and many liquids over a wide range of pressure, there is an empirical linear relationship between particle velocity (V_p) and shock wave velocity (V_s):

$$V_s = C + S_1 V_p \tag{19}$$

where C is the speed of sound in a medium and S_1 is an empirical parameter originating from the linear regression of the data (the slope of the curve). The Shock EOS linear model also allows the option to include a quadratic shock velocity, particle velocity relation of the form:

$$V_s = C + S_1 V_p + S_2 {V_p}^2 \tag{20}$$

where the quadratic input parameter, S_2, can be set to a non-zero value to better fit highly non-linear $V_s - V_p$ material data (ANSYS, 2019).

In the ANSYS Explicit Dynamics environment, two Shock EOS approaches are available: Linear and Bilinear. Throughout the literature, either the Shock Linear EOS or the Gruneisen formulation are frequently chosen to characterize the water droplet in fluid-solid impact modeling (ZHANG et al., 2019; VERMA et al., 2020, HU et al., 2021). Since the Gruneisen formulation of the shock EOS is not available in ANSYS Explicit Dynamics, the Shock Linear EOS has been selected as the modeling property for the water droplet in this study.

2.7.5 Smoothed particle hydrodynamics (SPH)

The smoothed particle hydrodynamics (SPH) method is a meshless approach to representing bodies in finite element analyses. It was first introduced in the field of astrophysics by GINGOLD and MONAGHAN (1977), where the method was used to simulate nonaxisymmetric phenomena and solve equations of fluid dynamics in the context of astrophysical flows. SPH is a Lagrangian scheme that is based on particle interpolation to compute smooth field variables. Such particles act as control masses and carry all physical properties of the system to be simulated. Because of its Lagrangian nature, the SPH method has clear advantages over traditional mesh-dependent Eulerian methods. For example, given that there are no grids in the computational domain, it does not suffer from mesh distortions that affect the numerical accuracy in simulations of large material deformations (SIGALOTTI; KLAPP; GESTEIRA, 2021).

In this method, fluid is defined by a set of moving particles, where an individual particle corresponds to an interpolation point with known fluid properties. Every single particle defined by the SPH formulation corresponds to a mass, but can also represent the hydrodynamic

(pressure and velocity) and thermodynamic (temperature and phase changes) states of the fluid at that point. A kernel function, also described as the interpolation function, is utilized in the formulation and is related to the smoothing length h_k (used to determine the region of influence of the neighboring particles) and the actual positioning of the neighboring particles. In that manner, an arbitrary property of each particle in the SPH domain is given by the approximated smoothed value of every neighboring particle within a radius of $2h_k$ (VERMA et al., 2020), as illustrated in Figure 30. In summary, it is the interpolating scheme between the particles, made possible by the kernel function, that will determine the material behavior.

Figure 30 – A particle's active domain in the SPH method.

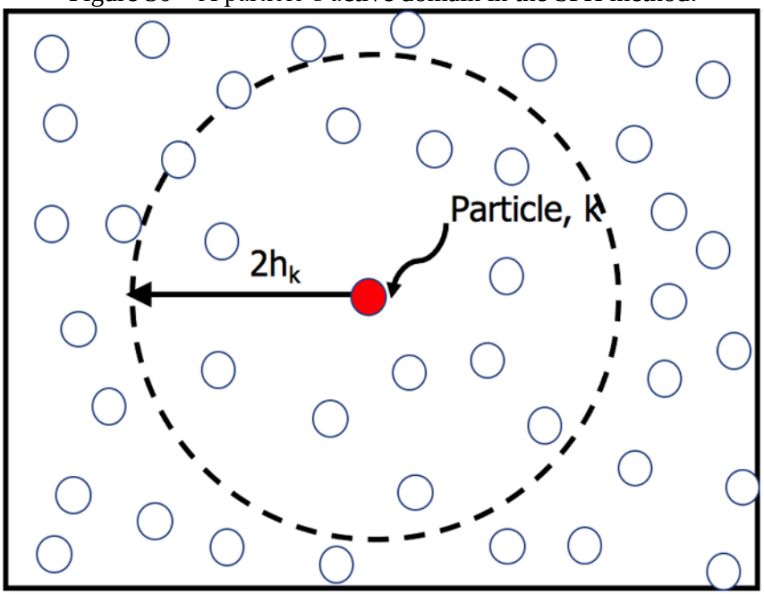

Source: VERMA et al., 2020.

The SPH approach is particularly effective in solving large deformation problems that can afford moderate computational cost, which is its key advantage over traditional FEA and the coupled Eulerian-Lagrangian approaches. The former is not as accurate as SPH for large deformation analysis, while the latter is usually more computationally expensive than SPH. Besides, the SPH approach has three other merits: (1) taking into account the large deformation of raindrops during impact on the solid, (2) directly calculating the transient stress time series, and (3) characterizing the impact wave propagation in the FEA model (HU et al., 2021). The practical usage of the SPH method in the ANSYS Explicit Dynamics environment is further discussed in the later sections related to the numerical modeling work of this study.

3. METHODOLOGY

Modeling an erosion onset prediction model for a wind turbine coating is an extensive, multi-fronted endeavor. The flowchart presented in Figure 31 is a summary of the steps taken to create it, which are detailed in the ensuing sections. It consists of multiple components, encompassing computational fluid dynamics, finite element modeling, rainfall data examination, and fatigue life analysis.

Figure 31 – Flowchart of the erosion onset prediction model for a wind turbine coating. The steps' corresponding section numbers are presented in parentheses.

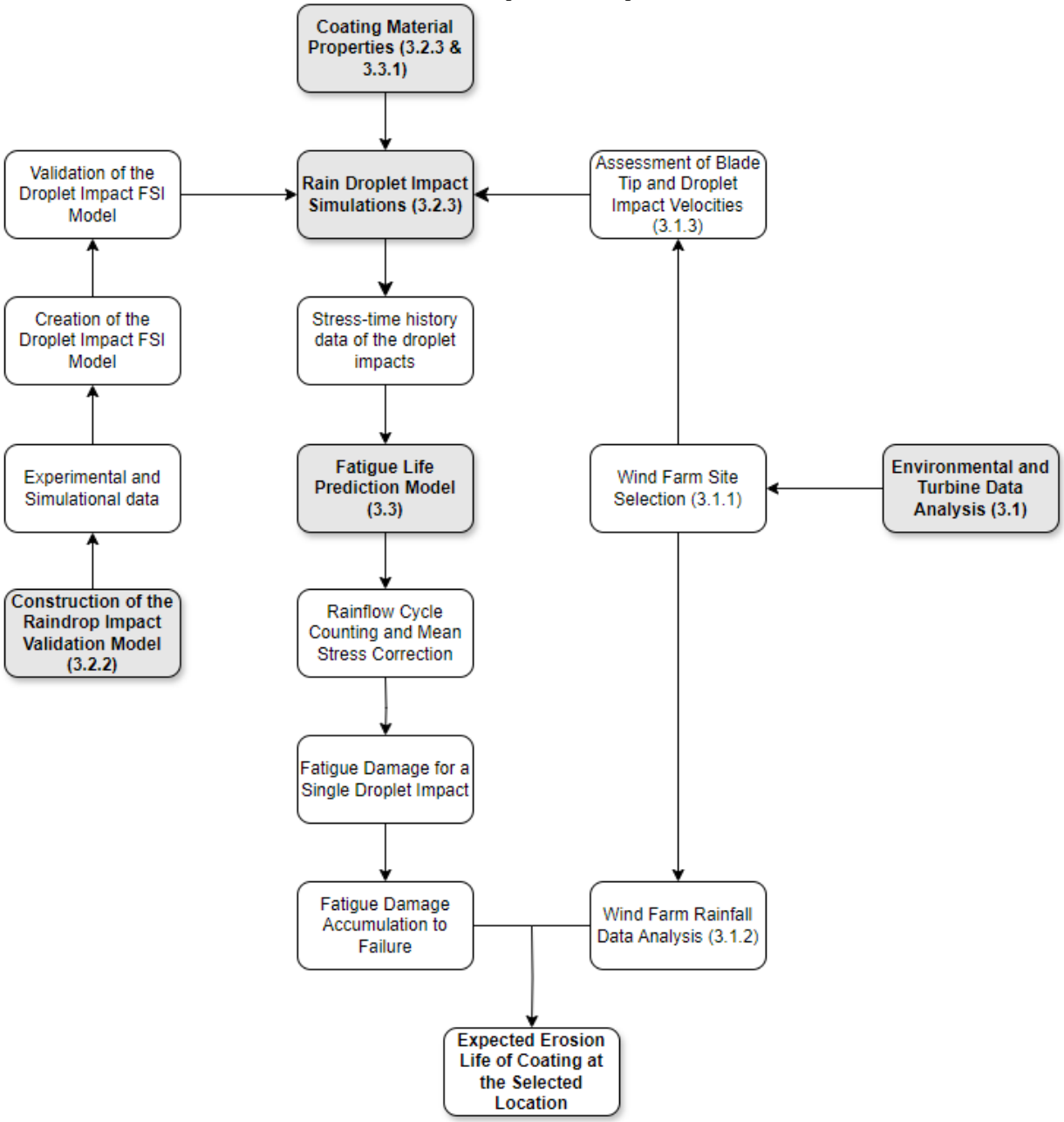

Source: Author (2024).

3.1. ENVIRONMENTAL AND TURBINE DATA ANALYSIS

This section details the methodology employed to acquire and analyze the environmental aspects surrounding the computational model, such as site and turbine selection and characterization, as well as the analysis of the site's rainfall data.

3.1.1 Site and turbine selection

The first step for rainfall analysis is to select the area or site of interest. Aiming to apply the erosion model with plausible environmental conditions for wind energy generation in Brazil, the site selection is done by combining the hotspots for future offshore enterprises on the Brazilian coast, along with the areas with availability of rainfall intensity data. Data for the areas are taken from a list of offshore wind farms undergoing environmental licensing in Brazil (IBAMA, 2024). This list supplies the proposed location of these farms, as well as the turbine model and quantity for each enterprise. The main prospective areas, outlined in Figure 32, can be geographically classified as Northeast (1, 2, and 3 – from the coast of Maranhão, going through Piauí and Ceará, up to Rio Grande do Norte), Southeast (4 – the coast of Espírito Santo and Rio de Janeiro) and South (5 – the coast of Santa Catarina and Rio Grande do Sul). Today, the Northeast region of Brazil is the definite hotspot for onshore wind energy, being responsible for 90.3% of the country's wind energy generation in 2022, especially in the states of Bahia and Rio Grande do Norte (24.17 and 23.20 TWh, respectively) (ABEEólica, 2023). For the licensing offshore enterprises, almost half of the licensing demands can be accounted to the Northeast region, with almost a third of the total number in the state of Ceará only. For the reasons outlined above, the site selection will be restricted to the Northeastern coast.

Figure 32 – Prospective areas for offshore wind farm enterprises in Brazil.

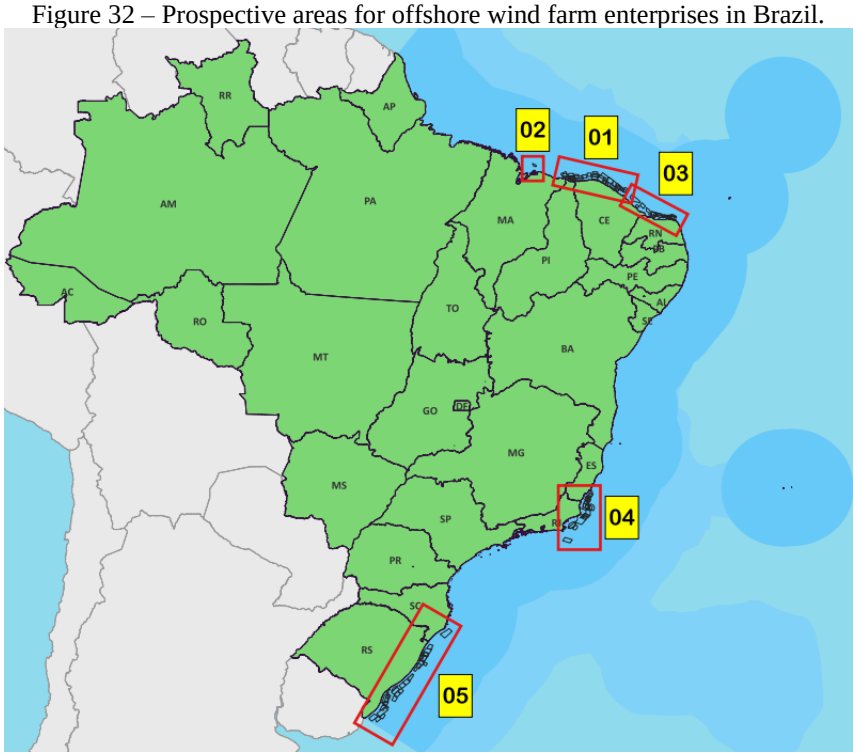

Source: IBAMA (2024).

The offshore wind farm licensing map from IBAMA (2024) provides the wind turbine models to be used by every prospective enterprise. As of July 2023, while 20% of wind farms still do not have a defined wind turbine model, the main turbine model selected, by a large margin, is Vestas' V236-15.0 MW, present at approximately 38% of all offshore wind farms, followed by GE's Haliade-X 12MW at around 10% of sites. The full data for the wind turbine models is presented in Table 1.

Table 1 – Summary data of wind turbine models from prospective Brazilian offshore wind farms.

Model	**Number of offshore wind farms present**	**Percentage of offshore wind farms present**
VESTAS V236 15.0 MW	30	38.46%
Undefined	15	19.23%
GE Haliade-X 12 MW	8	10.26%
WEC 265 20MW	7	8.97%
SG-14-222-DD	6	7.69%
NGT236	5	6.41%
SG-14-236-DD	2	2.56%
WTG-15.0-246	2	2.56%
SG-10-193-DD	1	1.28%
MHI Vestas 174	1	1.28%
IEA Wind 15-MW	1	1.28%

Source: IBAMA (2024).

As of July 2023, the V236 is still a prototype model, so turbine data is scarce and not all the necessary parameters are readily available. The Haliade-X 12MW is the second most prospected turbine model for future Brazilian offshore wind farms, as well as an already established, fully developed commercial turbine model. Due to these reasons, it has been selected for future analysis. The data for the Haliade-X 12 MW is presented in Table 2.

Table 2 – Characteristics of the Haliade-X 12 MW wind turbine system.

Parameter	Value	Unit
Power rating	12	MW
Rotor diameter	218.3	m
Hub height	138	m
Rotor speed range	7.81	rpm
Cut-in wind speed	3.5	m/s
Rated wind speed	10.5	m/s
Cut-out wind speed	34	m/s
Blade length	107.2	m
Blade mass	55	tonne

Source: VARGHESE, PAKRASHI, and BHATTACHARYA (2022) and WIND-TURBINE-MODELS (2023).

The next step is to define the wind turbine location. Having already established the turbine model as the Haliade-X 12 MW, and that the farm will be located in the Northeast region, there are seven candidate locations in the wind farm data from IBAMA (2024), as presented in Figure 33(a). The selected wind farm will be the one with the highest mean wind speed conditions, for which the data from the Global Wind Atlas (DAVIS et al., 2023) has been used. The Global Wind Atlas is a free, web-based application developed by DTU Wind and the World Bank Group, that identifies high-wind areas for wind power generation virtually anywhere in the world, primarily supporting wind power development during the exploration and preliminary wind resource assessment phases prior to the installation of meteorology measurement stations on site. It employs large-scale wind climate data provided by atmospheric re-analysis data (located in a 30 km grid), which is then used for mesoscale and microscale climate modelling (DAVIS et al., 2023).

When the wind farm locations are cross-checked with the wind speed data from the Global Wind Atlas (DAVIS et al., 2023), Figure 33(b), the RN-04 wind farm, located 7 km from the coast, has the greatest mean wind speed throughout its area, and is thus selected. For reference in future anemometric and precipitation evaluations, the wind farm area is

characterized by four vertices located at the latitude and longitude coordinates at (-4.894170, -35.962523), (-4.878241, -35.717337), (-5.011181, -35.759493), and (-4.975530, -35.998669).

Figure 33 – (a) Detail of the northeastern coast of Brazil, outlining the locations for the wind farms equipped with the Haliade-X 12 MW. (b) Figure 33(a) is overlapped by the wind speed data at 150 meters height.

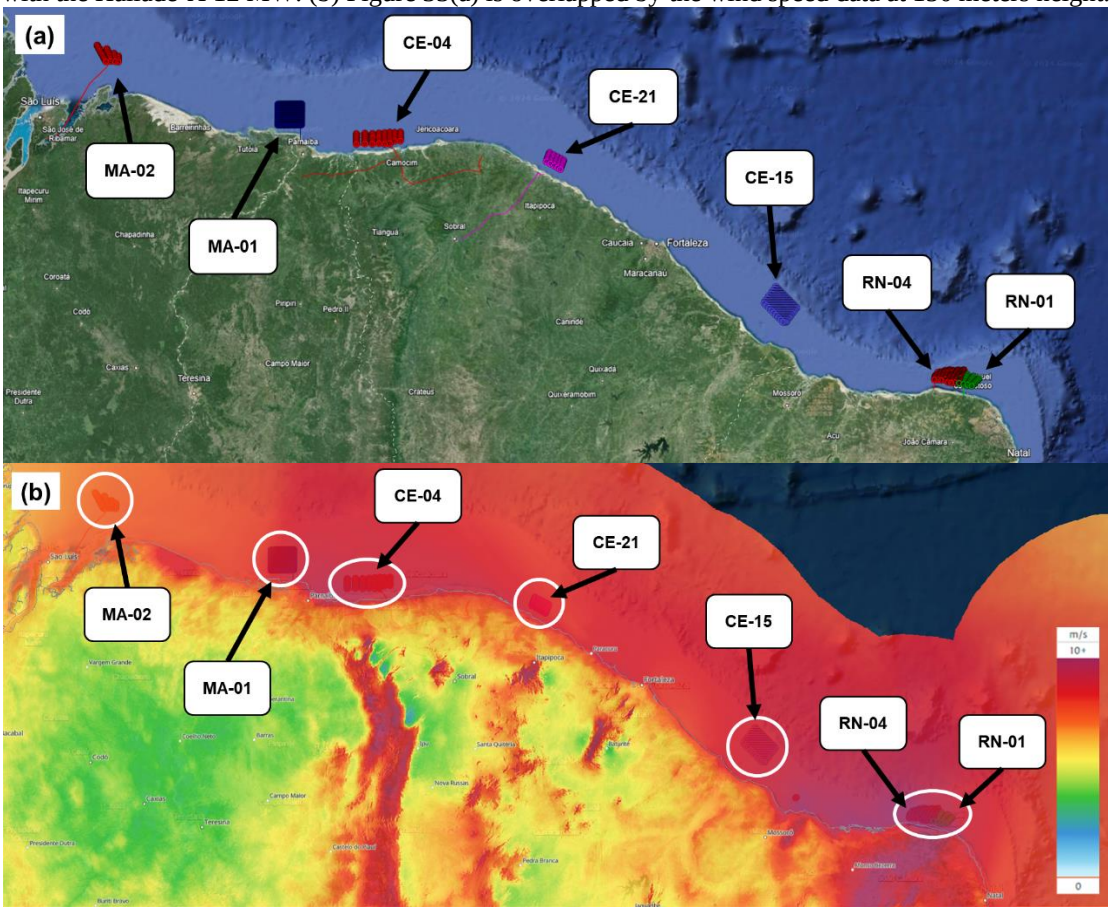

Source: (a-b) Adapted from IBAMA (2024); (b) Adapted from DAVIS et al. (2023).

3.1.2 Rainfall data analysis

From a meteorological perspective, a rain event is characterized by its intensity and duration. The intensity of rain is often measured by rain gauges and is expressed as the height of the water accumulated in a certain period, usually in mm/h. However, for the processes where the effects of individual raindrops are of interest, an intensity value per se is not very useful. In these cases, a more detailed methodology must be considered, and it is necessary to go through a series of additional steps.

One of the common ways that rainfall data is presented is by IDF (intensity-duration-frequency) curves. Although IDF curves are not directly used in this work (since only the rain intensity will be necessary for our methodology), these three characteristic components can be ascertained from NASA's IMERG (Integrated Multi-satellitE Retrievals for GPM) database,

accessed through NASA Giovanni (BEAUDOING and RODELL, 2020). IMERG's algorithm combines information from the GPM (Global Precipitation Measurement) satellite constellation to estimate precipitation over the majority of the Earth's surface. IMERG's data is particularly valuable over areas of Earth's surface that lack ground-based precipitation-measuring instruments, including oceans and remote land areas. IMERG fuses precipitation estimates collected during the TRMM (Tropical Rainfall Measuring Mission) satellite's operation (2000 - 2015) with recent precipitation estimates collected by the GPM mission (2014 - present) creating a continuous precipitation dataset spanning over two decades. This extended record allows scientists to compare past and present precipitation trends, enabling more accurate climate and weather models and a better understanding of Earth's water cycle and extreme precipitation events. IMERG is available in near real-time with estimates of Earth's precipitation updated every half-hour (NASA, 2024).

The half-hourly multi-satellite precipitation data option has been selected for this analysis. Data spanning up to 20 years (2004 to 2023) has been utilized, which should account for the statistical variability of precipitation scenarios, being in a timescale comparable to the lifetime of a wind turbine, at around 20 to 25 years. To focus on significant rainfall events only, the dataset was filtered to include only the rain intensities greater than 0.2 mm/h. To achieve a better visual comprehension, the combined rainfall intensity data is set as a probability density function (PDF). The resulting rain intensity distribution function for the RN-04 area is presented in Figure 34.

Figure 34 – Probability density function for rain intensity in the RN-04 region, from 2004 to 2023.

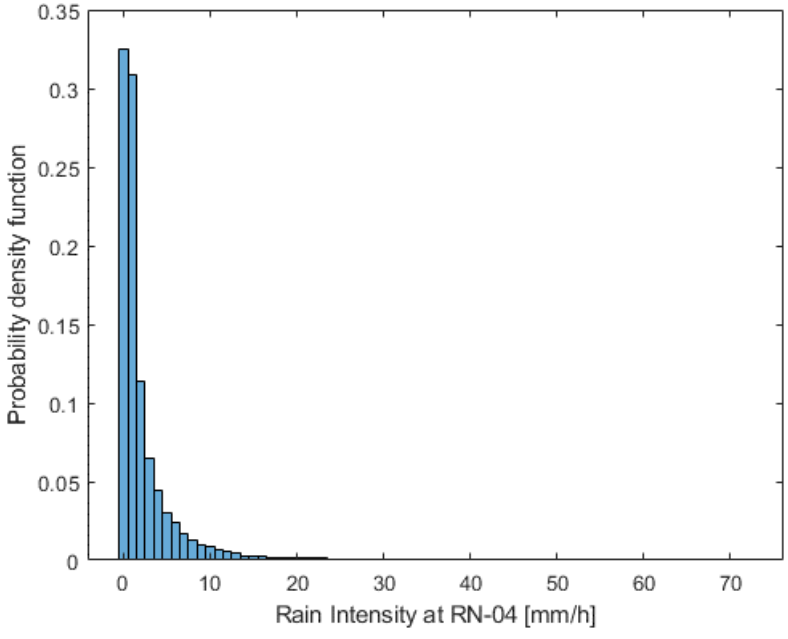

Source: Author (2024).

Next, it is necessary to be able to relate the rain intensities to the size of the raindrops. Several models have been proposed, and among them, Best's drop size distribution (BEST, 1950) is one of the most comprehensive models, being used in many similar works (KEEGAN, NASH, and STACK, 2014; AMIRZADEH et al., 2017a; DOAGOU-RAD, MISHNAEVSKY and BECH, 2020). The association proposed by Best is also very faithful to the empirical results from other sources (MARSHALL and PALMER, 1948), and for these reasons, it has been used in this study. Best's distribution for raindrop size takes the following form:

$$F = 1 - \exp\left[-\left(\frac{D}{1.3I^{0.232}}\right)^{2.25}\right] \tag{21}$$

where D is the drop diameter in mm, I is the rain intensity in mm/h and F is the fraction of liquid water in air comprised of drops with a diameter smaller than D (BEST, 1950). In statistical terms, F can be interpreted as the cumulative distribution function of raindrop size, and the effect of rain intensity on rain droplet diameter can be better comprehended when visualizing the associated probability density function (AMIRZADEH et al., 2017a). This function has been plotted for several rain intensities in Figure 35. BEST (1950) states that to ensure the accuracy of Equation 21, it is necessary to exclude 10% of the water volume comprising the smallest raindrops and 5% of the water volume comprising the largest raindrops.

Figure 35 – Probability density function (PDF) of raindrop size at various rain intensities derived from Best's raindrop size distribution.

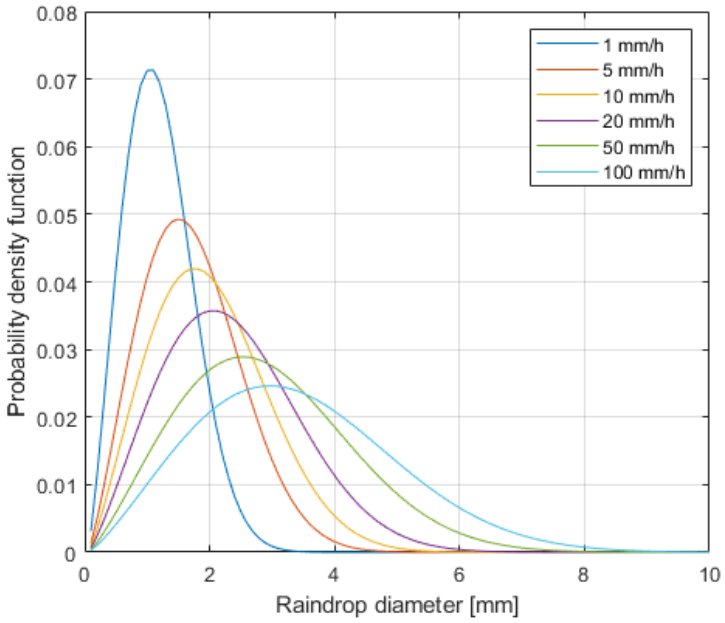

Source: Author (2024).

The selection of droplet diameters to be simulated has been done in a manner that they cover much of the droplet size distribution from the most commonly occurring rain intensities at the selected sites considered, while taking into account BEST's (1950) accuracy requirement

to exclude the smaller and bigger droplet volumes. As such, the droplet diameters considered in this study are 0.5 mm, 1 mm, 1.5 mm, 2 mm, 2.5 mm, 3 mm, and 4 mm.

Another valid consideration is whether the shockwaves and stresses from different impacts interact and interfere with one another, especially as the rain intensity increases and the number of raindrops impacting the same location does too. Fortunately, even at absurd rain intensities such as 100 mm/h, the stress waves decay quickly enough (in less than 1 ms) that no two consecutive droplet impact stresses would overlap with each other (DOAGOU-RAD and MISHNAEVSKY, 2020). Therefore, it is safe to assume that the stress waves from different impacts do not interact.

The method used in this study to define the number of impacting droplets throughout a period is to consider a single droplet diameter for every analysis. The number of uniform droplets is determined by estimating the volume of water for every rain event (here defined as every hourly rainfall occurrence) over a standard impact area, and divide it by the volume of a droplet of the specific diameter, obtaining the number of droplets as if every droplet had the same size. The full calculation method and its considerations are outlined in the following paragraphs.

BEST (1950) proposed the following relationship between the volume of water in the air and the rain intensity:

$$W = 67I^{0.846} \tag{22}$$

where I is the rain intensity in mm/h, and W is the amount of liquid water per unit volume of air expressed in mm^3 of water per m^3 of air. While Equation 22 allows the association of a volume of air with its volume of contained water at a specific rain intensity, it is still necessary to standardize its volume unit. When accounting for the influence of droplet distribution within a raindrop field, the method applied by some studies (AMIRZADEH et al., 2017ab; HU et al., 2021) was to consider the raindrops as uniformly distributed in a tall-column volume, where the height of the column is equivalent to the multiplication of the relative impact speed of the droplet with the duration of the rain event. The rain field event was then simulated by modeling a solid of a specific impacting area, traveling through the column at the target impact speed.

In these studies, while the droplets were considered spatially distributed when simulating the impacts to the substrate, the fatigue damage of any point in the surface has been considered as the sum of all contributing droplets within a radius r from the selected point; larger droplets having greater influence areas, their stress waves dissipating after they travel a certain distance from the point of impact. As shown in Figure 36(a), to calculate the fatigue

damage at point A, one has to consider all the droplet impacts colliding with the surface within a radius *r* from point A equivalent to the influence area of the largest raindrop. In the example shown in Figure 36(b), the fatigue damage in the small center square area is obtained by the superposition of multiple individual droplet impacts around it (red dots). The larger square area represents the base of the rain field column. In the long run, what an arbitrary point in the target area collects in terms of fatigue damage is independent of its location (AMIRZADEH et al., 2017b).

Figure 36 – (a) Determination of the influence area from the size of the area affected by the impact of the largest raindrop. (b) Effective raindrop impact points in the rain field column domain (larger surrounding square). The smaller center square represents the fatigue evaluation zone, while the red dots represent the droplets that are causing fatigue damage in this zone.

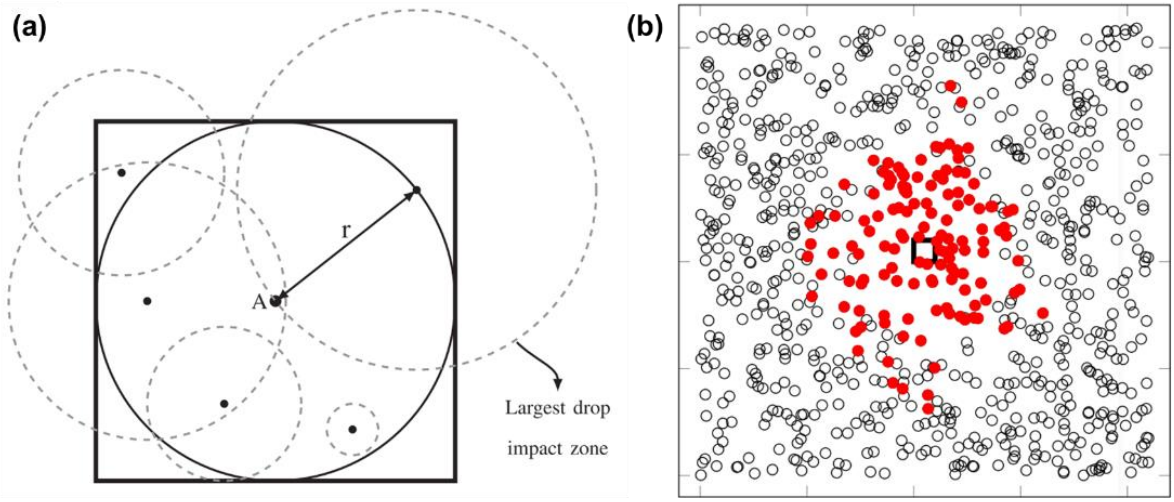

Source: AMIRZADEH et al. (2017b).

The methodology from AMIRZADEH et al. (2017b) described above, suggests an influence radius *r* equivalent to 9 times the droplet radius. The rain field column volume is:

$$V_{column} = 27D^2Vt \tag{23}$$

where V_{column} is the total volume of the rain field column, D is the diameter of the largest considered droplet, V is the relative impact speed, and t is the rain event duration. Considering the largest simulated droplet diameter as 4 mm, the base of the rain field column has been set as a square area with 36 mm sides, which would conservatively account for all the droplet impacts around the square center area that contribute to fatigue. Additionally, the relative impact speed is considered to be 90 m/s (refer to Section 3.1.3), while the rain event duration is one hour (rain intensity data employed have an hourly resolution). The total water volume of fatigue-contributive impacting rain droplets at a certain point can be ascertained by combining Equation 22 and 23 in the following equation, summing up every occurring rain event:

$$V_{water} = \sum_{i=1}^{n} W_i * V_{column} \tag{24}$$

Considering the shape of the rain droplet as a sphere for the sake of this study only, the volume of a droplet, V_D, of diameter D, is calculated by the expression for the volume of a sphere:

$$V_D = \frac{\pi D^3}{6} \tag{25}$$

The number of rain droplets of a single diameter D, N_D, can thus be calculated by dividing the total water volume of impacting rain droplets that contribute to fatigue at a certain point (V_{water}, Equation 24), by the volume of a single droplet of diameter D (V_D, Equation 25) and the number of years spanning the rain data employed (t_y). The resulting plot for the uniform droplet diameter distribution, alongside its power regression, is presented in Figure 37.

$$N_D = \frac{6V_{water}}{\pi D^3 t_y} \tag{26}$$

Figure 37 – Equivalent yearly number of droplets (in the millions) for a uniform droplet size distribution in the RN-04 area. The y-axis is in logarithmic scale for a better visualization.

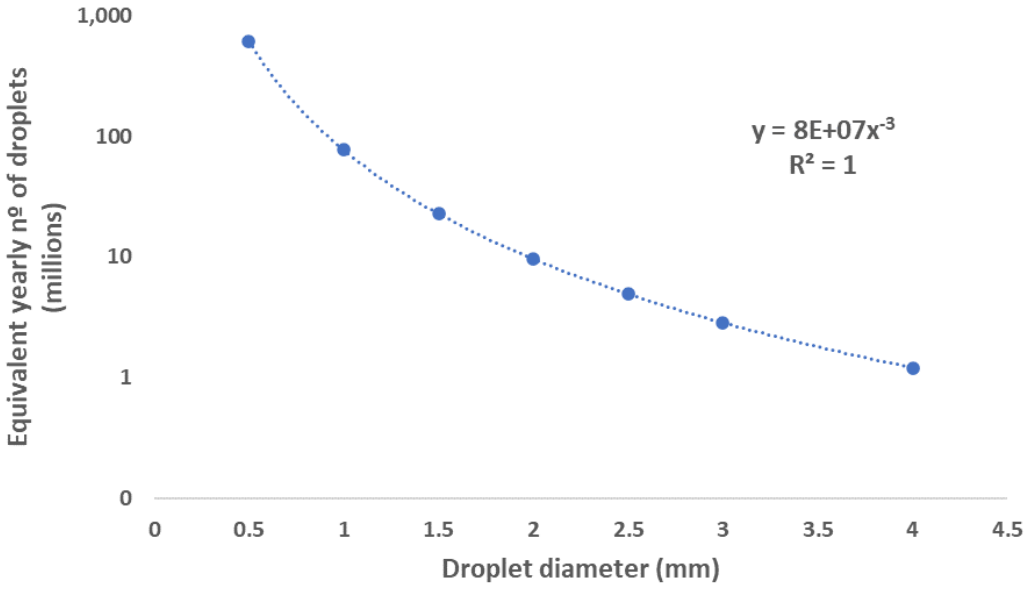

Source: Author (2024).

3.1.3 Assessment of the relative droplet impact velocity

This section will go through the steps for defining the relative droplet impact velocity to be used in the droplet impact simulations. First, it is necessary to evaluate the selected wind turbine power curve and its blade tip speed range. Second, the wind speed data at the wind farm

location must be defined (turbine and site selection have already been concluded in Section 3.1.1). Additional related parameters that require definition are the droplet terminal velocity and the angle of attack. Since this evaluation will encompass a large timeframe of months to years of wind turbine operation, average conditions have been assumed and average parameters have been used whenever possible to reduce the number of simulations required.

The blade tip velocity is largely governed by the wind velocity, cut-in speed, cut-out speed, rated speed, and the blade profile. The blades in a wind turbine start rotating when the wind speed exceeds the cut-in speed, since at very low wind speeds there is insufficient torque exerted by the wind on the turbine blades to make them rotate. As the wind speed increases above the cut-in speed, the wind turbine will start rotating and generating power. The power generated rises very fast until it reaches the power output limit of the electrical generator (rated power output) when the wind speed reaches the rated wind speed. At higher speeds, the generated power is limited, remaining constant, with no further increases in output power until the wind speed reaches the cut-out speed. When reaching the cut-out speed, a braking system is employed to bring the rotor to a halt, avoiding damage to the turbine (COLE, 2022).

Unfortunately, the Haliade-X 12 MW manufacturer power curve is not available. To setup the wind turbine's power curve, the parametric model developed by SAINT-DRENAN et al. (2020) is selected. Using the model's Python code made available by the researchers, it is possible to input the wind turbine data from Table 2 along with the environmental data in the selected location to generate the power curve for any wind turbine and location combination. The air density was set to 1.16 kg/m³, a value that better suits the conditions of the Brazilian Northeastern coast (SILVA, 2003). The power coefficient model used has been selected from the parameter data set from DAI et al. (2016), although the power curves are shown to not be sensible to alterations in the power coefficient parametrization models (SAINT-DRENAN et al., 2020). The last relevant parameter to characterize the model's power curve is the turbulence intensity.

Since the relationship between wind power and wind speed is non-linear, the effect of high-frequency variations in the wind speed on the power must be taken into consideration (NØRGAARD and HOLTTINEN, 2004). This is usually realized by considering the turbulence intensity (TI) defined as:

$$TI = \frac{\sigma(u)}{\mu(u)} \tag{27}$$

where $\mu(u)$ represents the mean wind speed and $\sigma(u)$ the standard deviation of the wind speed measured at a frequency of 1 Hz or higher during a period of 10 minutes (IEC, 2005). Since there is no wind speed data at such frequencies for the location selected, it is nearly impossible to ascertain an approximate value for the average turbulence intensity of the selected site. It is possible to assume it is in the lower range since this is an offshore area, which are regions with notably lower turbulence (BODINI, LUNDQUIST, and KIRINCICH, 2020).

Drawing from the extensive data and observations from POLLAK (2014) for offshore turbulence intensity gathered from meteorological masts, some assumptions can also be made about the RN-04 area: its proximity to the coast (around 20 km), its stable wind direction regime (which blows mostly from the open sea or alongside the coast, as presented in Figure 38), its relatively high average wind speed and the elevated turbine height all are indicative of turbine intensity values on the lower end of the spectrum. Based on that, a turbulence intensity of 5% has been selected as input for the wind turbine power curve parametrization script. Mind that this is an estimation made from limited empirical data collected from very different geographical and climatic conditions, and does not account for other factors such as interannual variability, atmospheric stability, and wake effect influence. If power curve data is available for a real wind turbine at the analyzed site, that would be much preferred. The resulting power curve for the Haliade-X 12MW wind turbine is presented in Figure 39.

Figure 38 – Yearly compass roses for various sites in Northeastern Brazil. The compass around the RN-04 region is highlighted in red.

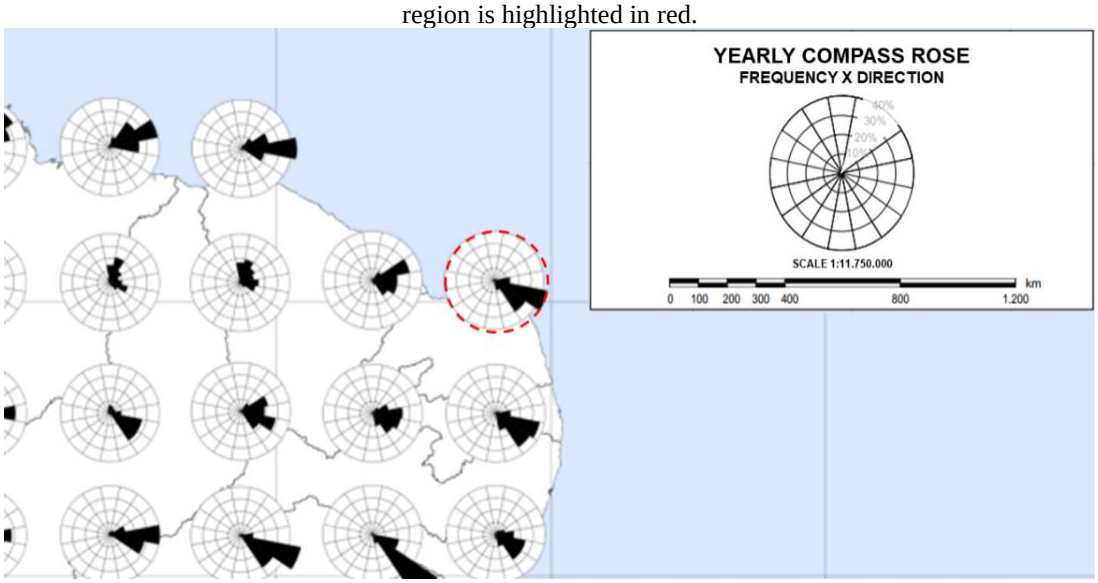

Source: Adapted from CEPEL (2017).

Figure 39 – Representative power curves for a wind turbine with a nominal power of 12 MW and a rotor diameter of 220 m, such as the Haliade-X 12 MW. The orange curve considers a turbulence intensity of 5%.

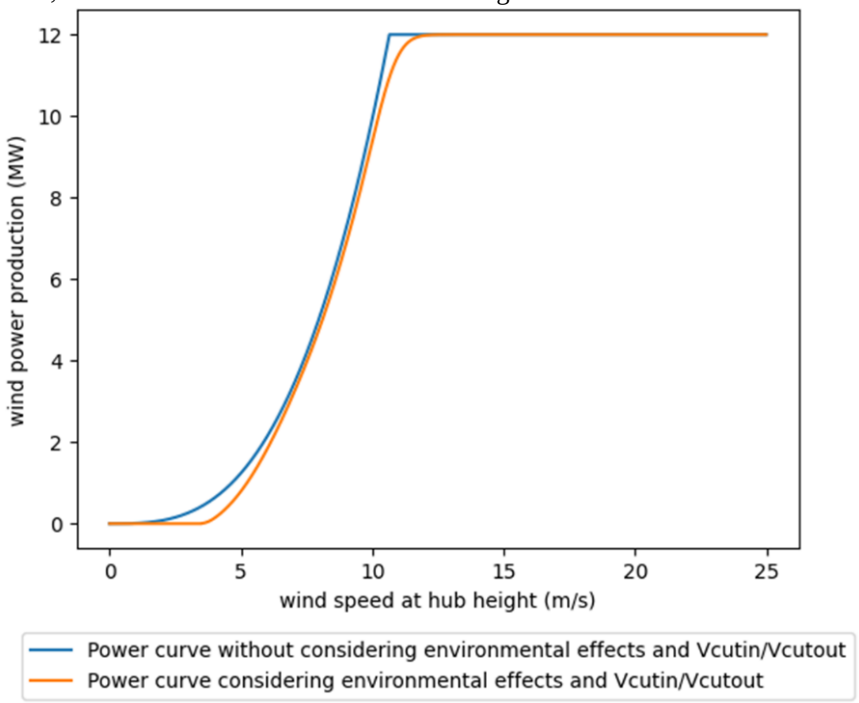

Source: Author (2024). Generated with the script from SAINT-DRENAN et al. (2020).

The mean wind speed in the RN-04 area is obtained from the Global Wind Atlas (DAVIS et al., 2023). With data available for heights of 100 and 150 meters, the wind speed is interpolated to the turbine's hub height of 138 m. The mean wind speed distribution among the windiest areas is presented in Figure 40. Considering the entire extension of the RN-04 wind farm area, the mean wind speed at a 138-meter height is set to 9.95 m/s.

Figure 40 – Mean wind speed distribution curves for the RN-04 area at multiple heights.

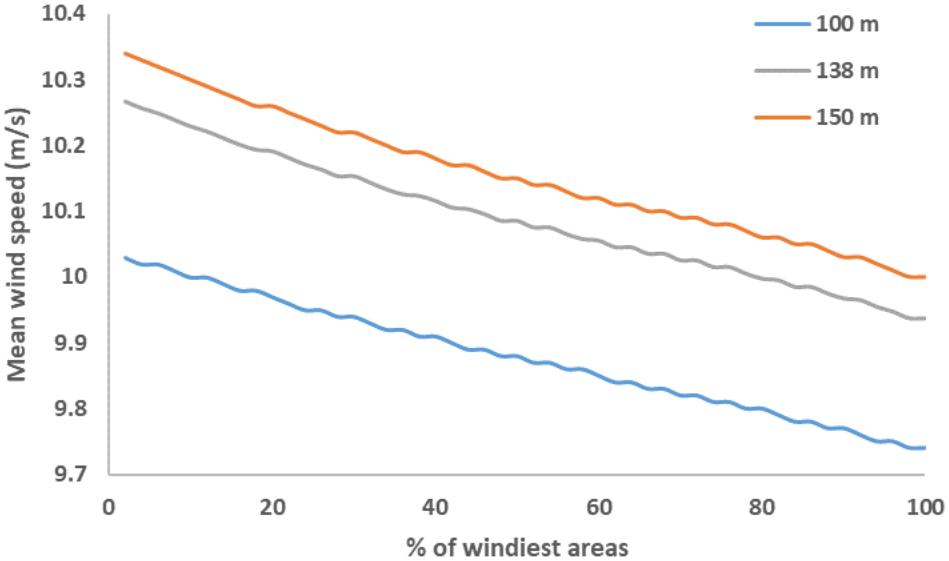

Source: DAVIS et al. (2023).

To calculate the minimum and maximum tip speeds, SAINT-DRENAN's et al. (2020) modeling script, based on the upscaling model from GARCIA (2013), provides formulas for

the parametrization of the minimal and maximal rotor rotational speed as a function of the rotor diameter, which are, respectively, in rpm:

$$Vr_{min} = 188.8 * {D_{rotor}}^{-0.7081} \tag{28}$$

$$Vr_{max} = 793.7 * {D_{rotor}}^{-0.8504} \tag{29}$$

where D_{rotor} is the diameter of the rotor. From these equations, minimum and maximum tip speeds can be obtained by:

$$V_{tip} = Vr * \frac{(2\pi * D_{rotor})}{120} \tag{30}$$

where Vr represents the minimum and maximum rotational speeds. The minimum and maximum tip speeds are then calculated to be 47.7 and 93.1 m/s, respectively, of which the former is associated with the cut-in speed, while the latter with the rated and cut-out speeds. With these, the tip speed can be interpolated to the condition of the average wind velocity in the desired area and height.

Given that rain droplets impact the leading edge at different impact angles during operation, different angles of attack can be considered. It is also assumed that only the velocity component normal to the surface contributes to the impingement. For the sake of simplification, since this would require a lot more computational simulations and the analysis of the variation of fatigue life with the blade profile is not the aim of this study, the angle of attack is conservatively set to 5° as is expected that, at the average wind speeds experienced at the selected location, the optimal pitch angle and angle of attack will be at a lower range, between 5° to 10°, especially for the blade sections near the tip (SUDHAMSHU et al., 2016).

The last factor to be considered is the droplet terminal velocity, which increases alongside the droplet's diameter, leveling out at around 9 m/s for diameters over 3.5 mm, as presented in Figure 41 (KEEGAN, NASH and STACK, 2013). For simplicity's sake, this parameter is standardized following the expected average rainfall intensity for the selected site and the droplet size distribution by rainfall intensity (refer to the data plots in Figures 34 and 35). The droplet diameter selected is 1.75 mm, above average, to be conservative regarding the predictive model, and the droplet terminal speed is thus set to 6 m/s.

Figure 41 – Free fall terminal velocity of water droplets through stagnant air for a range of stable droplet diameters.

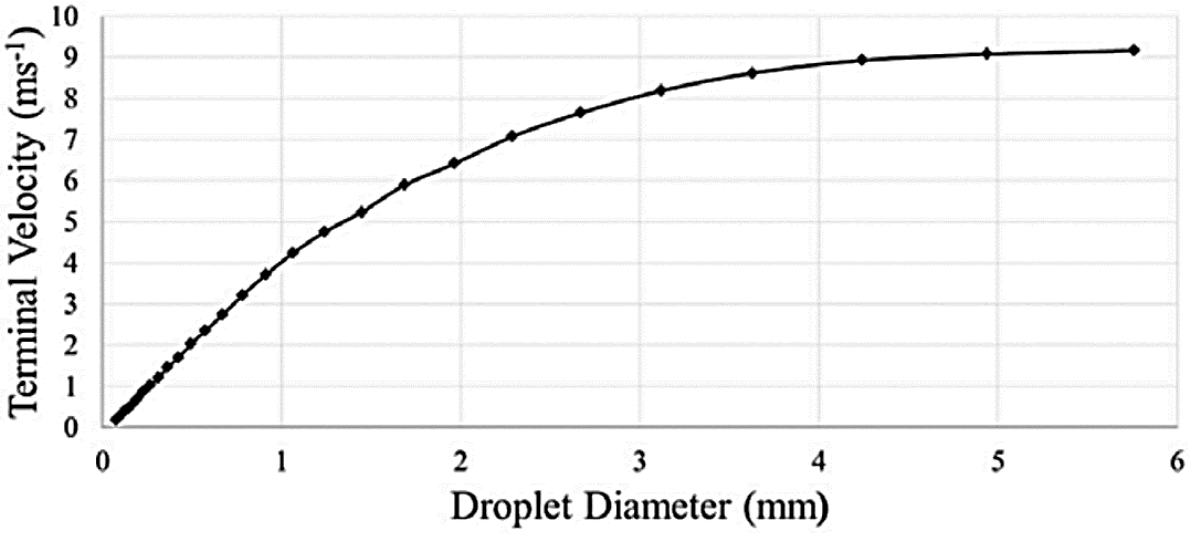

Source: KEEGAN, NASH and STACK (2013).

These parameters are incorporated with the tip velocity to obtain the relative impact velocity, by Equation 31:

$$V = \sqrt{(V_t * \cos(\mathrm{A}) + V_d)^2 + V_{wind}{}^2} \tag{31}$$

where V_t is the tip velocity, A is the angle of attack, V_d is the droplet velocity and V_{wind} is the wind velocity. The values are summarized in Table 3. The resulting relative impact velocity is approximately 90 m/s, which will be the impacting velocity used in the ensuing droplet impingement simulations.

Table 3 – Summary of the parameters employed in the impact velocity assessment.

Parameter	Value	Unit
Blade tip velocity	83.8	m/s
Droplet velocity	6	m/s
Wind velocity	9.95	m/s
Angle of attack	5	Degrees
Relative impact velocity	90	m/s

Source: Author (2024).

3.2. THE DROPLET IMPACT COMPUTATIONAL MODEL

An FSI computational model is developed in ANSYS, where the fluid domain is modeled using smoothed particle hydrodynamics (SPH), and the structure domain representing the coating is modeled using conventional finite element method. Its results are initially

compared with experiments performed by ZHANG et al. (2019), to validate the numerical model for impacting water droplets. After validation, the model is adjusted to the conditions observed in the blade during operation (see Section 3.1), and finite element impact simulations are done for different droplet diameters. The resulting stress-time history data will serve as input for the fatigue life prediction model.

3.2.1 Base parameters of the computational model

This section goes over the general base parameters of the numerical models, the ones common and applicable to both its validation and definitive versions.

The CAD (Computer Aided Design) model, represented in Figure 42, was built in ANSYS DesignModeler and Explicit Dynamics modules and is constituted of two general bodies: a spherical water droplet and a square solid surface. The model was created in a computer with the following specifications: processor 12th Gen Intel® Core™ i5-12600K 3.70 GHz, NVIDIA GeForce RTX 3060 12GB, 32GB DDR4 RAM.

Figure 42 – Geometry model for the droplet validation computational model.

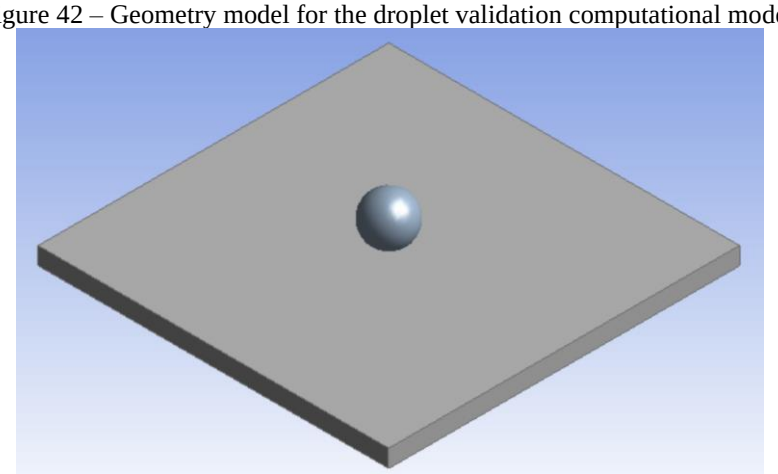

Source: Author (2024).

The model was then submitted to the ANSYS Explicit Dynamics module. An explicit dynamics analysis has been chosen because it allows a very detailed simulation of very fast and non-linear phenomena such as high-speed impacting droplets. To use an explicit dynamics simulation, first, some explicit parameters must be imputed to the materials used. To account for the compressibility of the liquid, the water droplet was defined with an equation of state parameter, in which the ANSYS Shock EOS Linear option was selected. The resulting V_s-V_p equation from the Shock EOS Linear characterization of the water droplet is presented in Figure

43. The material parameters used for the water droplet were set at the same values used by ZHANG et al. (2019) in their validation study and are presented in Table 4.

Figure 43 – Relationship between shock wave and particle velocity for the Shock EOS Linear characterization of the water droplet at the Explicit Dynamics environment.

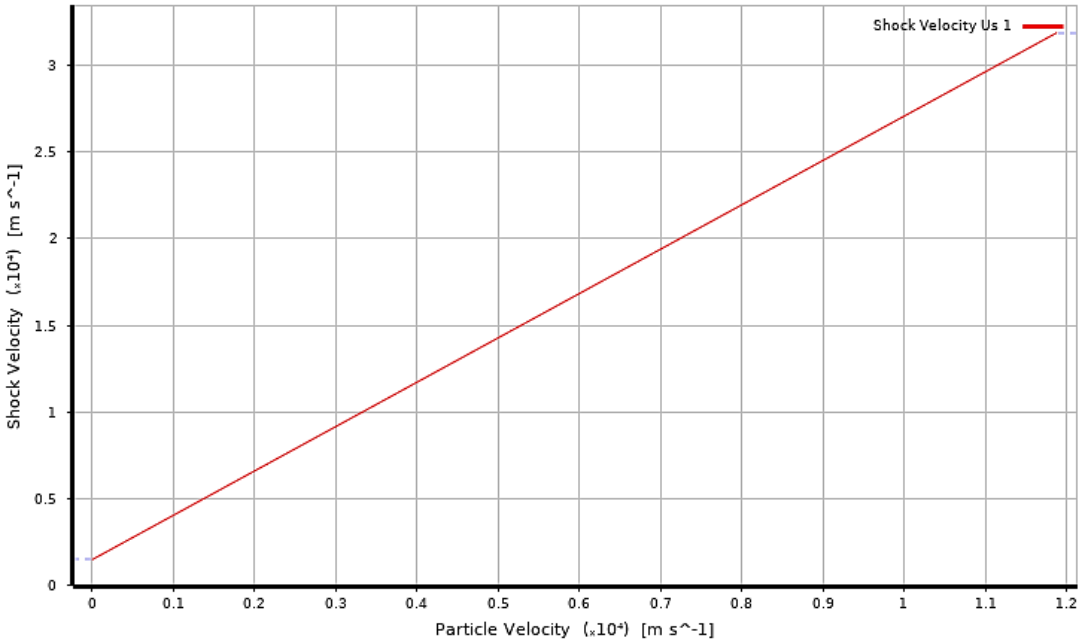

Source: Author (2024).

Table 4 – Properties for water droplet and Shock EOS parameters

Density (kg/m³)	Γ - Gruneisen Coefficient	C (m/s)	S_1	S_2
1000	0.5	1480	2.56	0

Source: Author (2024).

In the Explicit Dynamics modeling system, the initial conditions are the next parameters to be set. On the Geometry options, the Stiffness Behavior of the bodies was set to Flexible, while the Reference Frame of the solid was defined as Lagrangian, and the liquid as Particle, to allow the use of SPH features. The Standard Earth Gravity option is turned on, keeping the droplet under an acceleration equal to Earth's gravity. The solid body inferior face is constrained with a Fixed Support boundary condition, and its lateral faces are set with the Impedance boundary condition to prevent any undesirable stress wave reflections, which are both usual approaches for particle impact simulations (AMIRZADEH et al., 2017b; ZHANG et al., 2019; VERMA et al., 2020). For the validation model, Figure 44, the solid body is fully constrained by the Fixed Support condition: a necessity to be able to output the impact force reaction and validate the model. In the definitive model, only the bottom face of the solid body has the fixed support condition.

Figure 44 – Fixed Support (left) and Impedance (right) boundary conditions for the validation model.

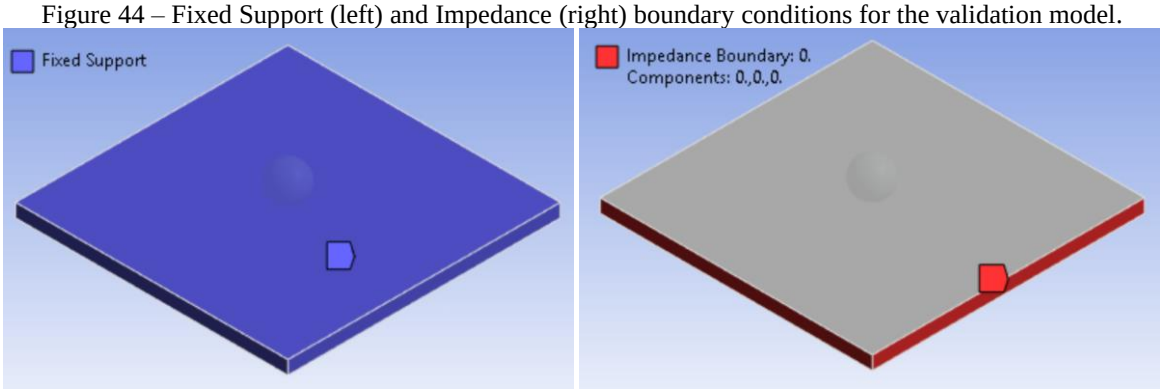

Source: Author (2024).

Since the droplet body, a fluid, will undergo large amounts of deformation along the very short length of the simulation, it is appropriate to define it by the meshless SPH method. To enable it in ANSYS Explicit Dynamics, the droplet body is first defined with the Particle Method. The SPH solver control settings are summarized in Table 5. To enable the calculation of all necessary internal forces that represent fluid-structure interaction, the body interactions between the water droplet nodes and the solid surface are set as frictionless and coupled with a trajectory-based contact detection algorithm with a penalty formulation.

Table 5 – SPH solver control settings.

Minimum Timestep (s)	**Density Factor (smoothing length)**	
	Minimum	**Maximum**
10^{-10}	0.2	2

Source: Author (2024).

3.2.2 Model validation and particle convergence study

The reference experiment used to validate the numerical droplet impact model was carried out by ZHANG et al. (2019), as well as LI et al. (2014), and consisted of the setup shown in Figure 45. There, the droplet was generated by using a flat-tipped needle that was connected to a high-precision syringe pump. Water droplets dropped off the needle under gravity and fell freely. Although they studied the impact responses of different droplets with varying sizes, shapes, and impact speeds, only a single spherical droplet of 2.70 mm diameter, and an impacting velocity of 2.67 m/s has been considered for the validation purpose of a computational model, which is the same for the current study. An aluminum plate with a machined and polished upper surface, with dimensions of 20 mm X 20 mm X 1 mm, was used to receive the falling droplet. A piezoelectric force transducer was attached vertically to the bottom of the plate to measure the contact forces generated due to water droplet impact. The

charge signal from the transducer was then amplified by a charge amplifier and converted to a voltage signal, which was recorded by a computer. A high-speed camera recorded the time evolution of the droplet shape at 40,000 frames per second. The droplet diameter and impact velocity could be measured from the images before the droplet collided with the plate surface.

Figure 45 – Schematic of the droplet impact experimental setup.

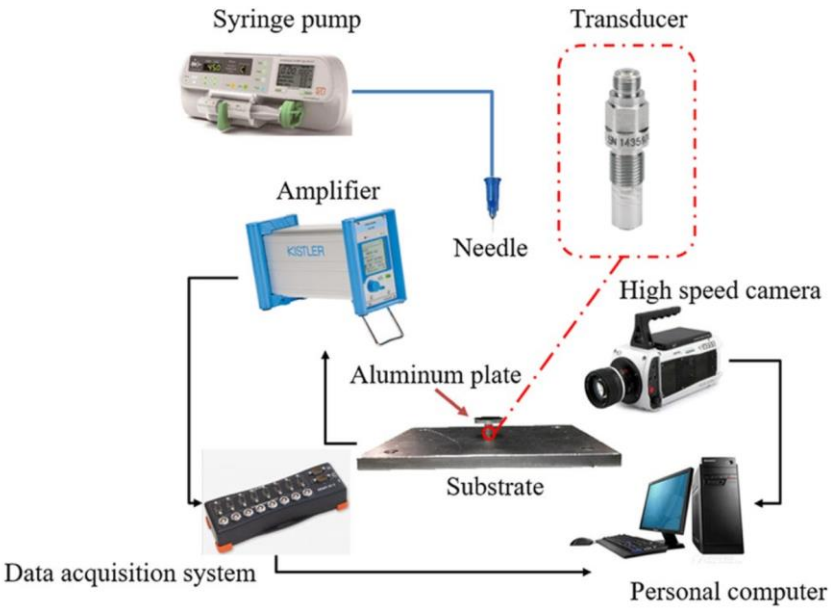

Source: ZHANG et al. (2019).

Next, it is necessary to replicate the reference experiment in a virtual model. The geometry of the solid body is altered to reflect the 20x20x1 mm aluminum plate. The material parameters used for the aluminum plate were set to be the same values used by ZHANG et al. (2019) in their numerical validation study, and are presented in Table 6. The water droplet is set with a 2.7 mm diameter and an initial impacting velocity of 2.67 m/s towards the plate.

Table 6 – Aluminum material properties.

Density (kg/m³)	**Young's Modulus (GPa)**	**Poisson's Ratio**	**Yield Strength (MPa)**	**Tangent Modulus (GPa)**
2820	70	0.3	240	27

Source: Author (2024).

To obtain results that are independent of mesh and particle size effects, a mesh convergence study is performed to obtain the minimum number of particles required to discretize the water droplet. To test for grid independence and make sure that the mesh sizing is both accurate and efficient, a series of simulations of varying droplet particle sizes were generated with ANSYS Meshing software.

The mesh sizing has been defined based on the recommendations of several previous works (AMIRZADEH et al., 2017b; DOAGOU-RAD, MISHNAEVSKY, and BECH, 2020; VERMA et al. 2020). In the end, it was decided to have an element width lesser than 0.15 mm and at least 20 elements thickness-wise. The plate mesh is then defined with 150 divisions in its sides and 20 divisions in its thickness. Element order must be linear to allow for Explicit Dynamics analyses. Table 7 presents the details of the validation mesh for the aluminum plate. Figure 46 presents a representation of the validation model's final mesh at the simulation starting time.

Table 7 – Aluminum plate validation mesh parameters

Sizing (nº of divisions)	Elements	Nodes	Element Type	Element Order
150 (sides) x 20 (thickness)	450.000	478.821	Hexa	Linear

Source: Author (2024).

Figure 46 – Mesh detail of the validation mesh at the simulation outset.

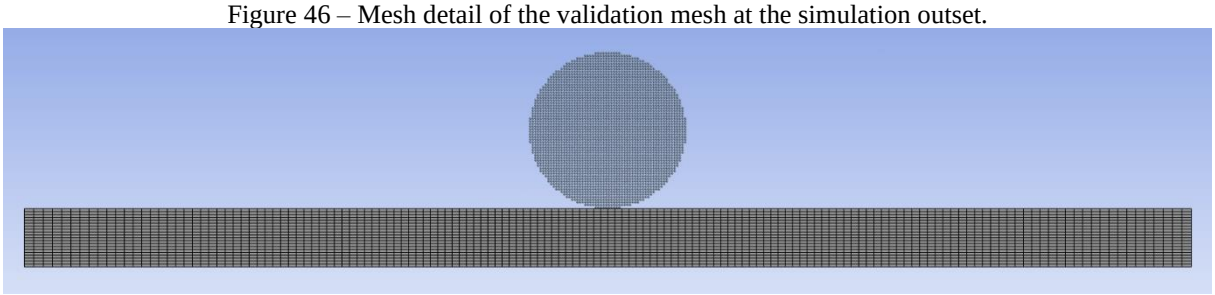

Source: Author (2024).

While the plate mesh sizing remains constant, the number of particles comprising the droplet will be incrementally altered to test for mesh independence, or more specifically in this case, particle independence. Since this is strictly for validation purposes, every simulation will be contained to a single droplet size equal to the one used in the laboratory experiments by ZHANG et al. (2019), but there will be different particle refinements to allow the investigation of particle independence.

The main output parameter selected to gauge the effectiveness of the validation is the impact peak force; the droplet morphology remains a secondary parameter for model validation reasons only. Validating the computational model will ensure its outputs make physical sense while allowing the outputs to be extrapolated to different parametrizations of droplet size, velocity, and surface material for which there is no experimental data to reference. Investigating particle independence is a particularly essential step to achieve streamlined simulations because most of the computational load is due to the number of particles contained in the meshless body.

To consider the numerical model validated, both the peak impact force and the droplet morphology will be compared with the empirical observations from ZHANG et al. (2019) and must attain results that are similar enough. The peak force on the aluminum plate will be measured with the Force Reaction option in ANSYS Mechanical, from which the total force reaction (the sum of forces in the X, Y, and Z-axis) will be considered. For the simulation to surpass the peak stage of the impact force curve and contain its point of interest, the minimal simulation end time was verified experimentally and set to 600 μs.

3.2.3 The definitive rain droplet impact model

After the first Explicit model under the same conditions from the tests executed by ZHANG et al. (2019) and LI et al. (2014), has been created, tested, and validated, it is necessary to adapt it to the actual material and environmental conditions for simulation of rain droplet impact in a wind turbine coating. The drop diameters considered in this study are 0.5 mm, 1 mm, 1.5 mm, 2 mm, 2.5 mm, 3 mm, and 4 mm, resulting in 7 unique simulations. The main output, to be used in the fatigue life prediction model, is the absolute maximum principal stress-time history, the same as AMIRZADEH et al. (2017b).

The geometrical setup is very similar to the one previously outlined in Section 3.2.2. Built in ANSYS Design Modeler and Explicit Dynamics modules, it is constituted of two bodies – a spherical SPH water droplet and now, a square polymeric material representative of the impacted coating. The polymer body geometry instance is only representative of the layer corresponding to the outermost surface, i.e., the coating or the erosion protection system, and has a thickness of 0.6 mm, a value similar to the recommended thickness for many coatings in the industry. The dimensions of the square solid body edges are dependent on the droplet diameter and will be set up posteriorly during mesh parametrization (refer to the summary presented in Table 10).

The selected coating material is the epoxy resin Epon E862, a commercial resin with applications in aerospace composites. Due to the detailed testing done by LITTELL et al. (2008) concerning both tension and compression, it was decided that the material properties presented in their study would be adopted for the coating material in the rain impact simulations. The relevant material data used to characterize the Epon E862 epoxy resin is presented in Table 8.

Table 8 – Epoxy coating material parameters

Density (kg/m^3)	Young's Modulus (GPa)	Poisson's Ratio	Bulk Modulus (GPa)	Shear Modulus (GPa)
1150	2.5	0.4	4.17	0.893

Source: LITTEL et al. (2008).

The mesh sizing in every plate instance is defined based on the corresponding droplet size, following the recommendations originally proposed by AMIRZADEH et al. (2017a) and AMIRZADEH et al. (2017b), which has also been used for other previous works (DOAGOU-RAD, MISHNAEVSKY, and BECH, 2020). The main points are two: The finite element mesh should be fine enough to ensure that the pressure profile covers a radius of 10 elements at the time of lateral peak maximum (at the crosswise section) and it should have at minimum 20 elements thickness-wise. At this sizing, the mesh will be able to include the smaller features of the impact pressure profile in the transient stress analysis, such as those near the lateral peak pressure position. A meshing schematic is presented in Figure 47.

Figure 47 – Schematic presenting the relationship between the solid's finite element mesh sizing and the impact pressure for any droplet size.

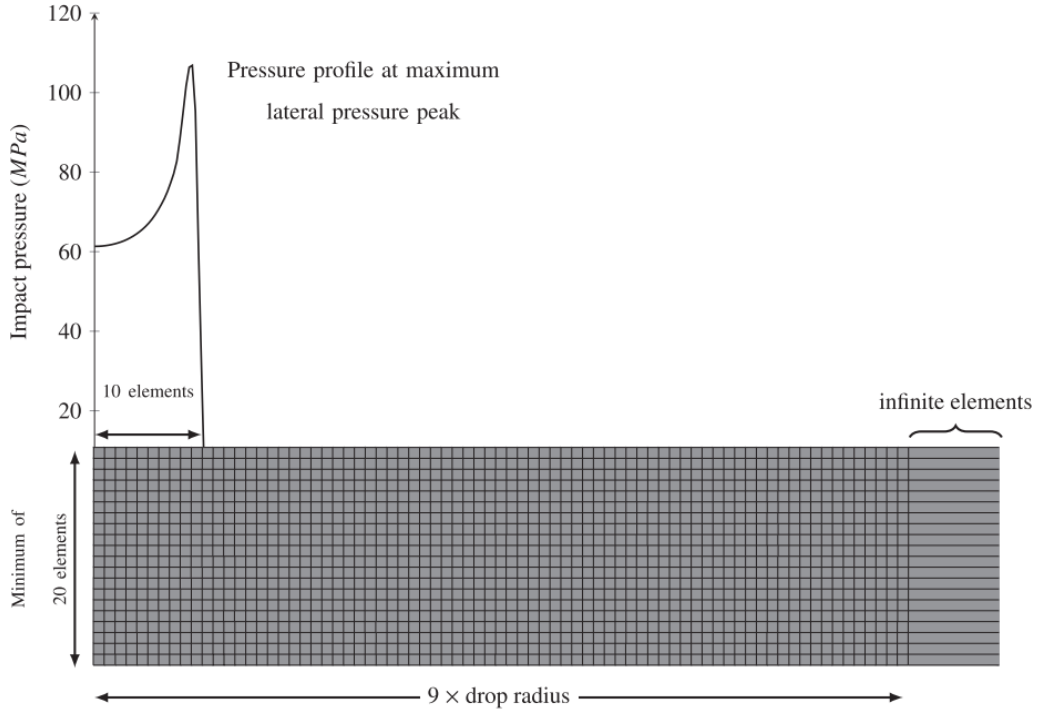

Source: AMIRZADEH et al. (2017b).

The maximum lateral pressure peak positions used to determine the mesh sizing are taken from the data provided by AMIRZADEH et al. (2017b) and interpolated for some of the droplet diameters. Although they have been determined for a 100 m/s impact velocity, it is assumed that the variation would be minimal for an impact velocity of 90 m/s. A summary of

the maximum lateral pressure peak positions and the maximum crosswise element sizes for the solid body is presented in Table 9 for every droplet selected.

Table 9 – Summary for the maximum lateral pressure peak positions and crosswise element sizes for multiple droplet diameters obtained from the data presented in AMIZARDEH et al. (2017a).

Droplet diameter (mm)	**0.5**	**1**	**1.5**	**2**	**2.5**	**3**	**4**
Maximum lateral pressure peak position (mm)	0.05	0.08	0.12	0.16	0.21	0.25	0.36
Maximum crosswise element size (mm)	0.005	0.008	0.012	0.016	0.021	0.025	0.036

Source: Author (2024).

To match these requirements, every droplet diameter simulated had its own configuration for (1) the solid body edge dimension, (2) the crosswise element sizing for the solid body, and (3) the particle sizing for the SPH droplet body. The body edge dimension refers to the length of the edge of the square-shaped solid body. Although AMIRZADEH et al. (2017b) recommended that the distance from the impact center to the impedance boundaries should be at least 9 times the droplet radius, this has not been deemed necessary for the present evaluation. The reason is that to keep the recommended size of the solid body while also maintaining the element size below the minimum required would greatly increase the number of elements, especially for the larger droplet diameters, leading to an unfeasible computational time. In their study, presented in Figure 48, AMIRZADEH et al. (2017b) have also shown that the droplet impact fatigue damage is quickly reduced along the distance to the center of impact: For most droplet diameters, the maximum fatigue damage declines in the order of thousands at a distance of just two times the droplet radius. Additionally, first, the main model output is related to peak stresses, which are expected to be mostly near the center of the impact surface, and second, there are impedance boundary conditions set at the lateral faces, such that the impact waves are also not expected to reflect at the sides and interfere with the original impact stress.

Figure 48 – Fatigue damage pattern for raindrops of various diameters on normalized axes. The x axes stretch from the impact point to 8 times the droplet radius.

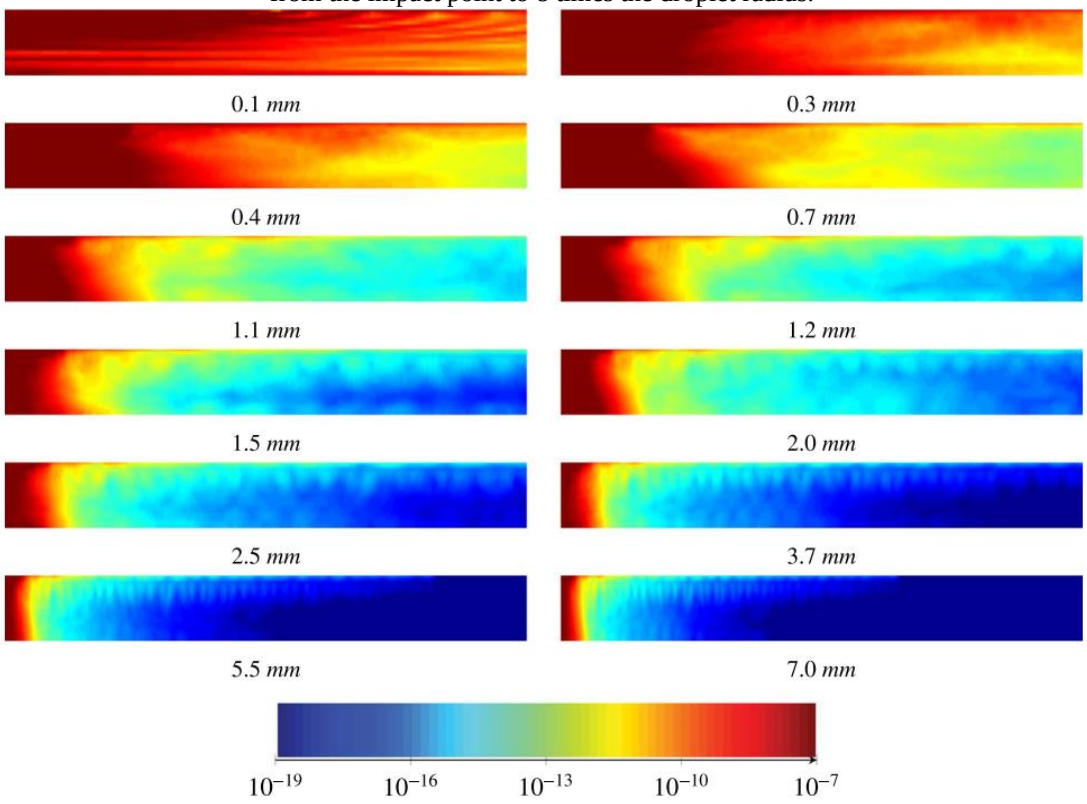

Source: AMIRZADEH et al. (2017b).

It was thus decided to group similar droplets, matching their solid body geometry and particle sizing configurations. There were 3 groups total, the first was composed of the 0.5 mm diameter droplet, the second was composed of the 1 and 1.5 mm diameter droplets, and the third was composed of the remaining droplets. The meshing configuration parameters are summarized in Table 10. The particle sizing of the water droplet followed the same configuration presented in the validation model, always keeping a minimum particle density of 60 (refer to Section 4.1.1 for the model validation results). The mesh sizing of the solid body was set with the Number of Divisions and Edge Sizing meshing options. Element order must be linear to allow for Explicit Dynamics analysis.

Table 10 – The definitive model's mesh configuration parameters.

Droplet diameter (mm)	Solid body edge dimension (mm)	Nº of divisions (crosswise x thickness)	Crosswise element size (mm)	Particle sizing (mm)	Nº of Nodes, Elements, and Particles
0.5	2	400 x 20	0.005	0.0083	N: 3.376.821 E: 3.200.000 P: 113.020
1	4	500 x 20	0.008	0.0167	N: 5.271.021 E: 5.000.000 P: 110.960
1.5	4	500 x 20	0.008	0.0167	N: 5.271.021 E: 5.000.000 P: 374.480
2	8	500 x 20	0.016	0.0333	N: 5.271.021 E: 5.000.000 P: 115.065
2.5	8	500 x 20	0.016	0.0333	N: 5.271.021 E: 5.000.000 P: 224.704
3	8	500 x 20	0.016	0.0333	N: 5.271.021 E: 5.000.000 P: 388.321
4	8	500 x 20	0.016	0.0333	N: 5.271.021 E: 5.000.000 P: 923.747

Source: Author (2024).

Since there is a wide range of droplet diameters, it is expected that their peak and post-peak behavior vary considerably. The smaller droplets will reach the lateral jetting stage earlier, entering the slowly descending post-peak stress phase earlier. As such, it would not make sense to simulate them to the same time extent as the larger droplet diameters. The simulation end times were thus set to 15 μs (for the 0.5 mm, 1 mm, and 1.5 mm diameter droplets), 20 μs (for the 2 mm diameter droplet), and 25 μs (for the 2.5 mm, 3 mm, and 4 mm diameter droplets). The number of result points was set to keep the results with the same sampling frequency of 50 ns. To ascertain the impact stresses, the Minimum Principal Stress and Maximum Principal Stress were selected and scoped to the solid body geometry only. Both outputs will be used in the Explicit Dynamics environment as inputs for a user-generated result for the AMPS. The AMPS will in turn be used as the input for the fatigue life prediction model to determine the fatigue damage caused by a single droplet of a particular size.

Additionally, to reduce the number of elements and save computational time, the fiber-reinforced composite structure of the blade is ignored in the definitive model. To validate this simplification, the stresses in the solid body were calculated, as per the previous parameters, for two separate instances: first, using only the coating layer, and second, with the addition of a composite layup structure representative of a wind blade leading edge. The test composite structure is representative of a laminate composed of 3 UD (unidirectional) layers, which would

amount to a 3 mm thickness. An assumption is made that the coating and the layers within the laminate are perfectly bonded, as the consideration of cohesive properties at their interfaces would convolute the stress analysis. A setup comparison is presented in Figure 49.

Figure 49 – Geometry setups: just the coating layer (left) and the coating-laminate combination (right).

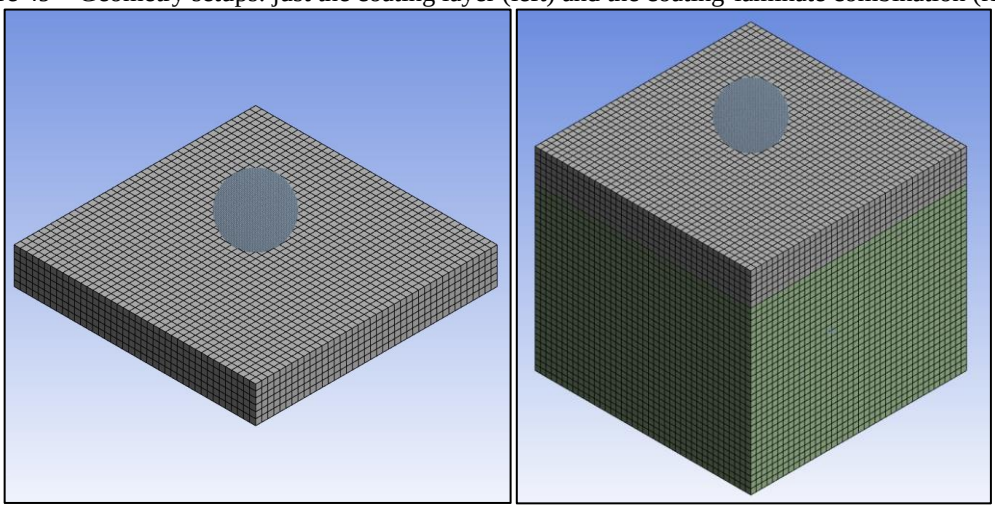

Source: Author (2024).

The mesh resolution was lowered in this validation test due to the amount of computational time that would be added to the simulation with the additional laminate structure, being simply set up with a mesh sizing of 0.1 mm. This isn't expected to influence the result, since a comparison between setups with equal mesh configuration is being considered. The selected material for the UD laminate is the Epoxy E-Glass UD, taken directly from the ANSYS material database, which has its main mechanical properties presented in Table 11. The material selection serves solely as a placeholder for this validation, and by no means is trying to be faithful to wind turbine blade layup design. The coating material remains the Epoxy Epon E862. An impact simulation comparison for a 1 mm droplet at 90 m/s is done between the coating and the coating-laminate geometry setup and the absolute maximum principal stress in the solid body will be considered for evaluation.

Table 11 – Epoxy E-Glass UD material data.

Density (kg/m³)	**Young's Modulus 1 (GPa)**	**Young's Modulus 2 (GPa)**	**Poisson's Ratio**	**Shear Modulus 1-2 (GPa)**
2000	45	10	0.3	5

Source: ANSYS (2023).

3.3. FATIGUE LIFE PREDICTION MODEL

This section goes over the fatigue life prediction model development. The model has been done in the Python programming language. Using the results obtained from the FEA droplet impact simulation and the rainfall data as inputs, the model intends to output an estimative for the erosion onset time of the particular coating.

3.3.1 Coating fatigue properties

Erosion modeling of coatings usually requires knowledge of the fatigue properties of the coating material. This kind of information is very restrictive for fatigue life evaluations such as this study's, as this data is usually not considered or disclosed in commercial coatings datasheets. Due to the scarcity and inability to find fatigue data for any commercial LEP coating, or the Epon E862, the next best option is to pick the data from a similar coating material available in the literature.

The selected material is the epoxy resin Hercules 3501-6, which had its fatigue behavior characterized in the technical report by WALRATH and ADAMS (1980), which determined the material's strength versus number of cycles (S-N) curves under tension-tension and compression-compression loadings. Fatigue testing was performed using a stress ratio of 0.1 and a cyclic rate of 5 Hz. Since compressive stresses are dominant during the droplet impact, the compressive fatigue results are selected. The S-N curve results for the Hercules 3501-6 is presented in Figure 50. Its average static compressive strength was 164 MPa, with results reaching up to almost 200 MPa.

Figure 50 – Compression static and fatigue strengths and its regression equation for the Hercules 3501-6 epoxy.

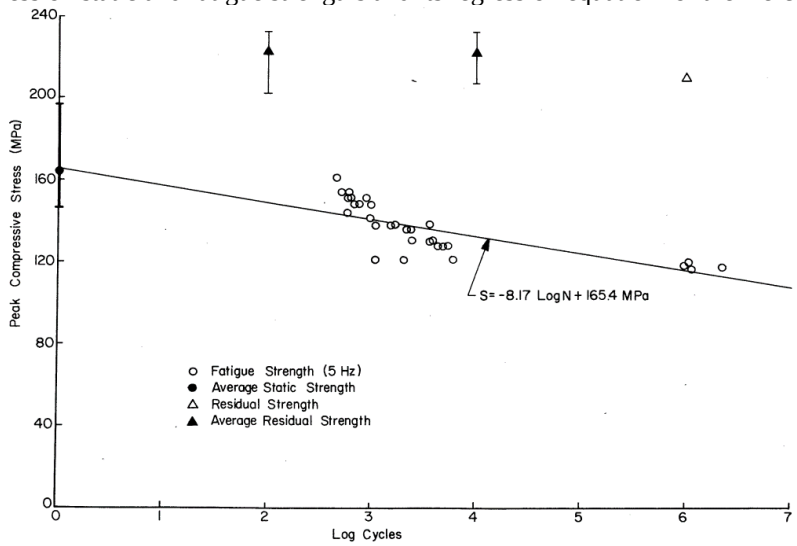

Source: WALRATH and ADAMS (1980).

Having the experimental data presented in the S-N curve and fitted to Basquin's law (Equation 6) provides the material's fatigue strength coefficient (FSC), σ'_f, and its fatigue strength exponent (FSE), b. The FSC and FSE will be essential in the fatigue life prediction model as inputs for the Palmgren-Miner hypothesis. Since the material being simulated is not the Hercules 3501-6, but the Epon E862, the S-N curve is adapted to match the higher ultimate compressive strength of the material, at 180 MPa (LITTELL et al., 2008). A sensitivity analysis for the material's fatigue life data is presented in Chapter 4. The adapted S-N curve with the supposed fatigue data for the Epon E862 is presented in Figure 51. Through a power regression, the resulting equation is in a format similar to Basquin's equation and the material data relevant to fatigue evaluation can be directly observed. These, plus the material compressive strength, are presented in Table 12.

Figure 51 – Comparison between the fatigue data for the epoxy Hercules 3501-6 and the supposed Epon E862.

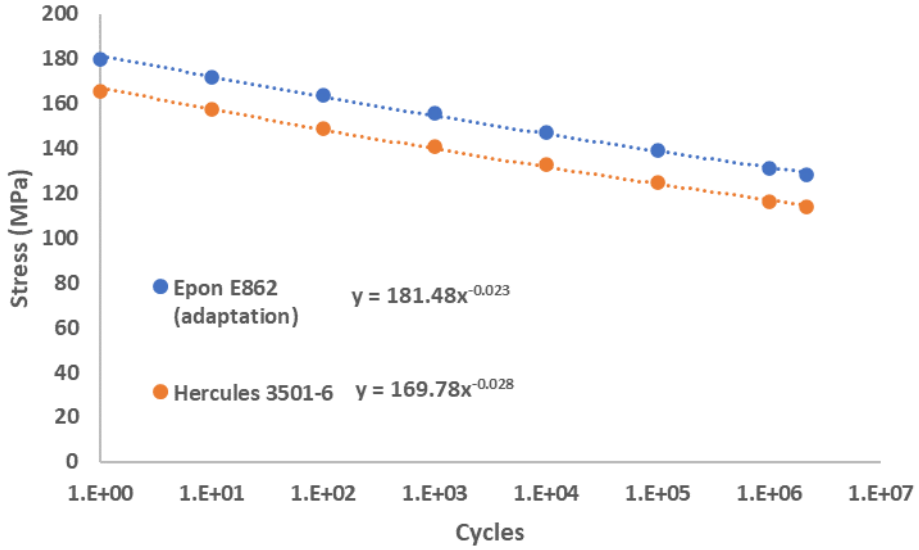

Source: Author (2024).

Table 12 – Epoxy coating parameters relevant to the fatigue life model. The ultimate compressive strength data is obtained from LITTEL et al. (2008).

Ultimate Compressive Strength (MPa)	FSC (MPa)	FSE
180	181.48	-0.023

Source: Author (2024).

3.3.2 Fatigue life analysis

The fatigue life model takes the stress-time history for a single droplet diameter and specific impact velocity, and couples it with the impacted substrate fatigue properties (presented

in Table 12), providing the fatigue damage for this single droplet impact. This model has been created in the Python programming language, and its script is available in Appendix A.

The initial steps in the fatigue life model are to input the data from Table 12, and the stress-time history from the computational model into it. These are the 7 selected droplet diameters (selected after the rainfall data analysis – Section 3.1.2), for which the absolute maximum principal stresses at a particular droplet size and impact speed (outputs from the computational model – Section 3.2.3) are inputted alongside the coating fatigue data (obtained from experimental data – Section 3.3.1). Then, the AMPS stress data (in Pascal units) becomes the input for the Rainflow cycle counting algorithm. The algorithm used is taken from the "Rainflow" project by JANISZEWSKI (2023), available at the PyPI repository. After processing the input signal, the algorithm outputs a numerical matrix, each line corresponding to a cycle or half-cycle. This matrix has 5 columns, containing the mean stresses, stress amplitudes, whether the cycle is a full or half-cycle (1 or 0.5, respectively), and its starting and ending point in the input signal.

The next step is to take the resulting matrix and work on its results. First, it is needed to apply the Linear Goodman Relation (Equation 14) to convert the multiaxial stress amplitudes into corrected equivalent stress amplitudes for zero mean stress. Note that the ultimate tensile strength in Equation 16 should be substituted with the ultimate compressive strength for the negative mean stresses (AMIRZADEH et al., 2017). After conversion, the corrected stress amplitudes can be applied to Basquin's law formula (Equation 6), providing the maximum number of cycles/impacts that the coating can endure up to the end of its incubation time. Both data are necessary inputs to the Palmgren-Miner cumulative fatigue damage. The summation is carried out over all the stress amplitude values present in for all cycles, with fatigue failure occurring when the damage index is equal to one. Since the recommended practice is to register all half-cycles as contributing to the fatigue damage as half of an equivalent full cycle of the same range and mean stress characteristics (CRANDALL, MARK, and KHABBAZ, 1962; MADSEN, 1990; SUTHERLAND, 1999), this is also included into the algorithm (Equation 9).

4. RESULTS AND DISCUSSION

4.1. NUMERICAL MODELLING OF THE LIQUID DROPLET IMPACT

In this section, the detailed results obtained from the computational droplet impact model validation and the droplet impact simulations are presented and discussed.

4.1.1 Model validation results

Droplet morphology analysis allows an initial, qualitative standpoint to modeling effectiveness. Figure 52 presents a comparison between the droplet shape during different stages of impact, between the experiments from ZHANG et al. (2019) to the left and the numerical simulation of this exact validation model to the right. Starting contact at 0 μs, the evolution of the impact phases can be noted by the droplet shape throughout the different timestamps – from the initial direct impact at 50 μs to the initiation and evolution of lateral jetting at 100 μs and 200-500 μs, respectively. All in all, the numerical model is very agreeable with the experiments in terms of droplet morphology, reproducing the droplet behavior during all stages of its impact on the aluminum plate.

Figure 52 – Side-by-side droplet morphology comparison between the experiments (left) from ZHANG et al. and the numerical simulation (right). Scale is maintained between the pictures.

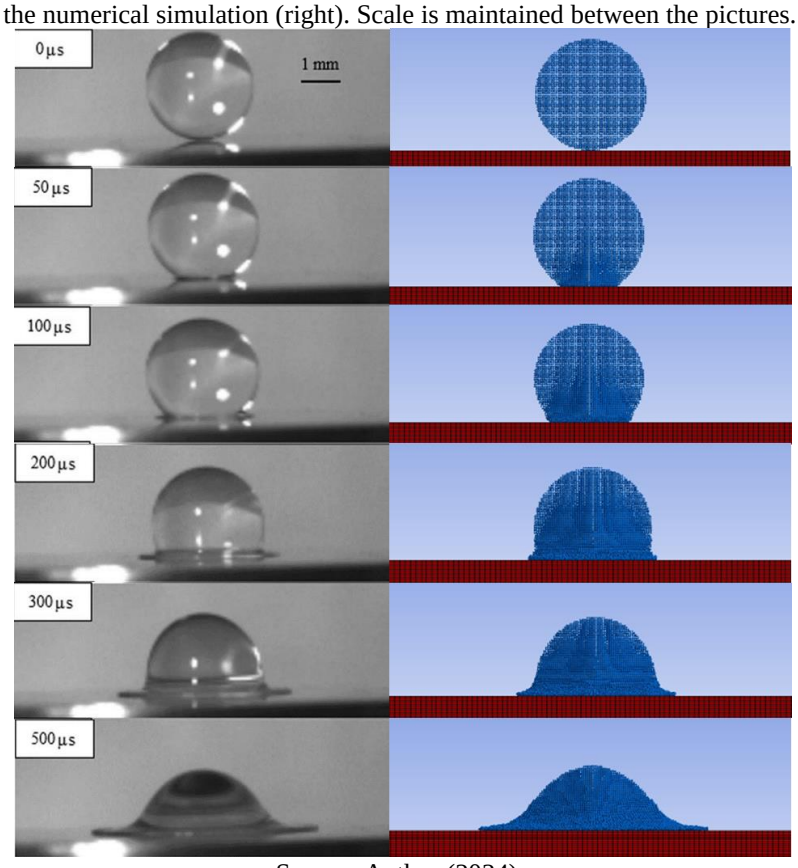

Source: Author (2024).

Comparing the impact force evolution at the initial contact stages is the other main point for validation. When the droplet collided with the plate, ZHANG et al. (2019) observed a rapid rising stage followed by a relatively slow falling stage from the impacting force, which peaked at 0.04499 N, just 3.5% larger than the analytical solution calculated from Equation 5 (0.04357 N). When simulating within the 600 µs interval, the simulations made with timesteps below 75 µs already presented a respectable agreement with the experimental and the numerical results from ZHANG et al. (2019) validation model (modeled in ANSYS Fluent), as demonstrated in Figure 53.

Figure 53 – Impact loading time evolution. The experimental and numerical results from ZHANG et al. (2019) are compared to the simulation results from this study at timesteps below 75 µs. The orange dotted line marks the simulation ending at 600 µs.

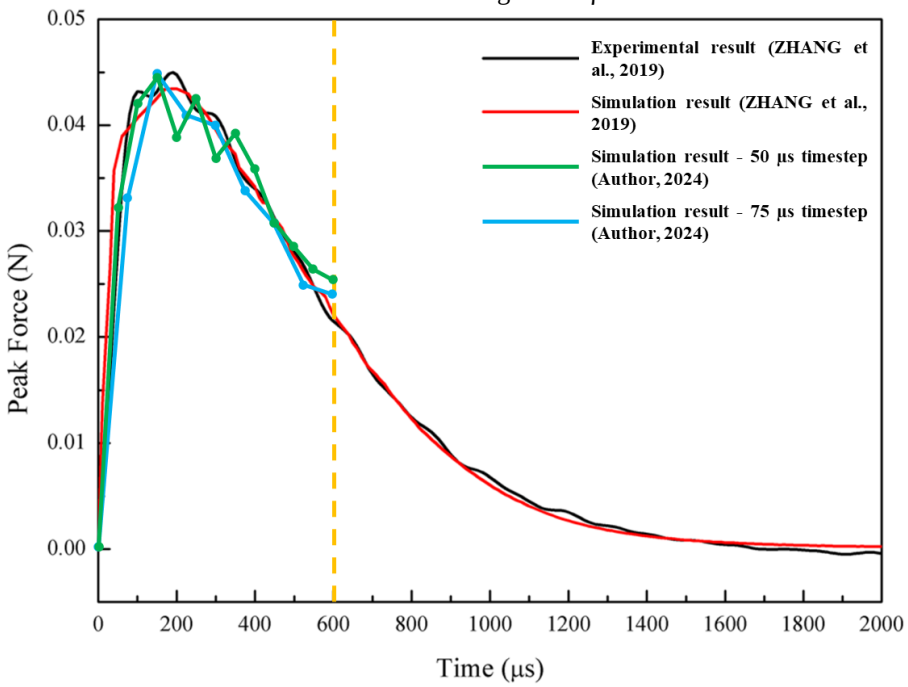

Source: Author (2024).

While refining the number of particles in the droplet body from, roughly, 55,000 to 130,000, the peak force promptly converged to 0.04508 N, just 0.21% above the empirical result of 0.04499 N (ZHANG et al., 2019), as presented in Figure 54. Particle convergence is achieved at approximately 110,000 particles, with any further increase in the number of particles having an insignificant consequence on the difference between the experimental and simulated results. To standardize the number of particles necessary for convergence to several droplet diameters, the particle density concept was created, which is the ratio between the droplet diameter and the diameter of a single SPH particle, as per Equation 32:

$$Particle\ Density = \frac{Diameter_{(droplet)}}{Diameter_{(particle)}} \tag{32}$$

This means that whatever the droplet diameter in the simulation, the particle size parameter must be adjusted to keep the particle density parameter the same. Therefore, the particle density in any analysis has been kept to a minimum of 60. Together with the droplet morphology evaluation, these are positive results to validate the numerical model. Table 13 presents all the results for the particle convergence study.

Figure 54 – Particle convergence study.

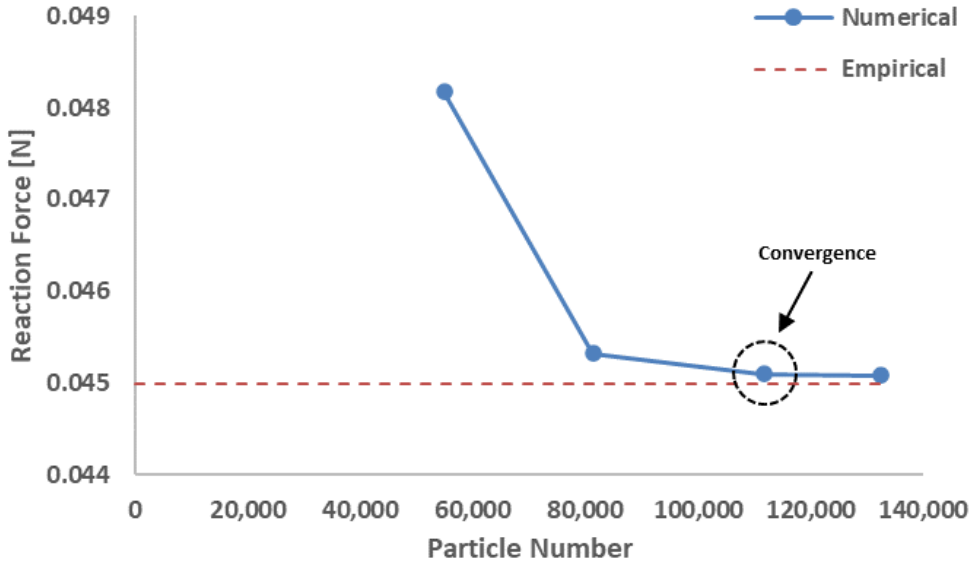

Source: Author (2024).

Table 13 – Particle convergence and independence study data.

Nº of Particles	Particle Size [mm]	Particle Density	Reaction Force [N]	Difference to the previous simulation	Difference to the empirical result
54,987	0.0570	47.4	0.04817	-	7.07%
81,360	0.0500	54.0	0.04532	-5.91%	0.74%
111,696	0.0450	60.0	0.04510	-0.49%	0.24%
132,587	0.0425	63.5	0.04508	-0.04%	0.21%

Source: Author (2024).

As for the validation case for ignoring the composite substrate, a comparison between the absolute maximum principal stress between both setups is presented in Figure 55. Besides the similarity between the stress values alongside the entire simulation timespan, the peak stress values in the coating surface in both cases were the same, which was expected since the peak stresses would be contained near the impact surface. This result corroborates with other works in the literature where the underlying composite structure was omitted for simulation purposes (KEEGAN, NASH, and STACK, 2014; AMIRZADEH, et al., 2017b; KAORE et al., 2022).

Considering that (1) the inclusion of the composite structure in the model would sharply increase the computational cost, and (2) the scope of the present study is limited to the coating's incubation period, simplifying the finite element model by considering solely the isotropic coating material would not alter the stresses within the coating layer significantly, and thus it is not deemed as an issue.

Figure 55 – Impact stress (AMPS) comparison between coating/laminate and coating-only simulation setups.

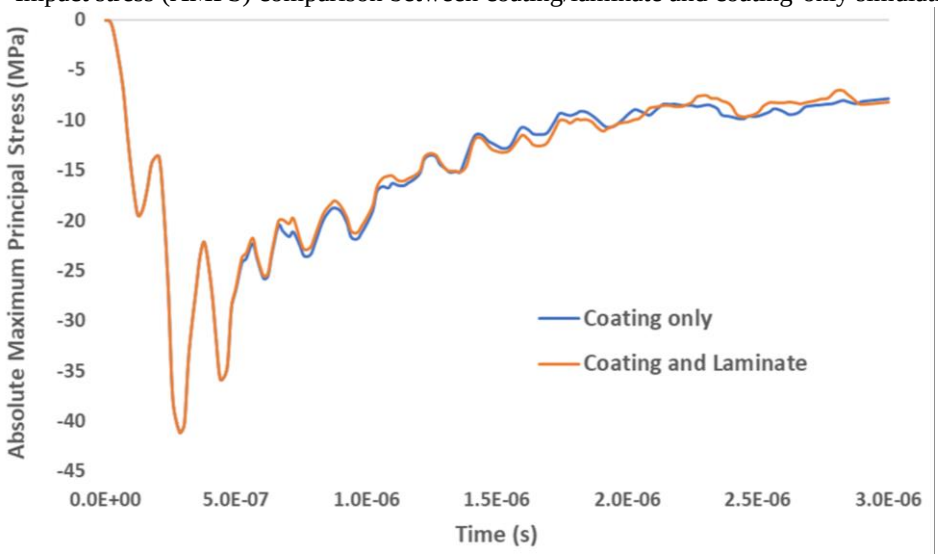

Source: Author (2024).

4.1.2 Droplet impact stress results

The base stresses used for this analysis are the Minimum and Maximum Principal stresses. From them, the Absolute Maximum Principal stress (AMPS) is calculated. The stress data for a 1 mm diameter droplet is presented in Figure 56.

Figure 56 – Stress data for a 1 mm diameter droplet. The minimum principal stress and the absolute maximum principal stress are equal.

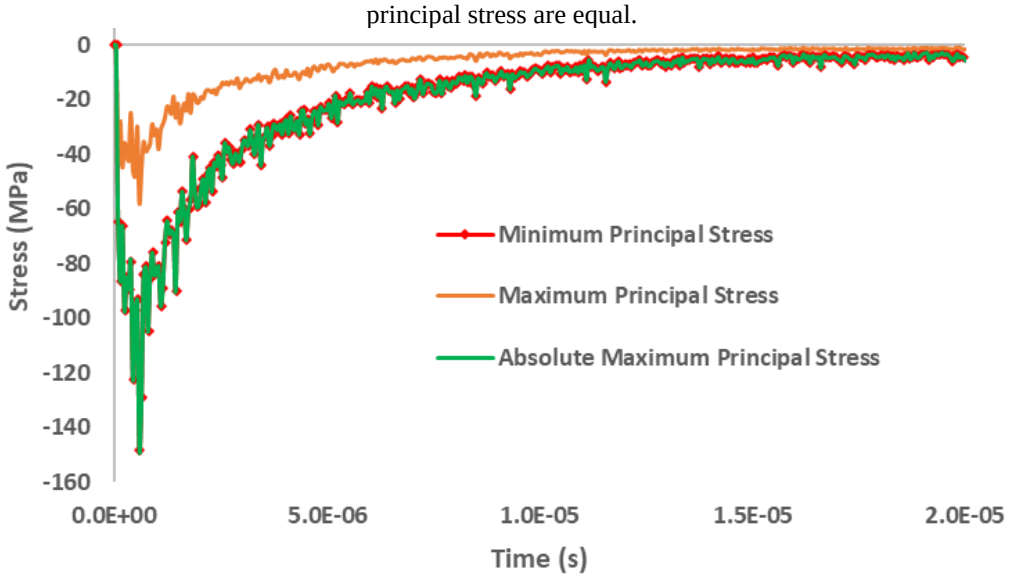

Source: Author (2024).

The main simulation input for the fatigue evaluation model, the AMPS is not directly available as an output from the ANSYS environment, and a custom result has to be set up. Contrary to what its name may imply, it is just whatever the absolute maximum value is between the maximum and minimum principal stresses while retaining its original sign. In the case of an impacting droplet, as expected, the compressive stresses are much larger and the absolute maximum principal stress is equal to the minimum principal stress for every droplet diameter during the period simulated, for all simulated scenarios, as presented in Figure 57.

Figure 57 – Absolute Maximum Principal Stress over time for multiple droplet diameters impacting the epoxy coating at 90 m/s.

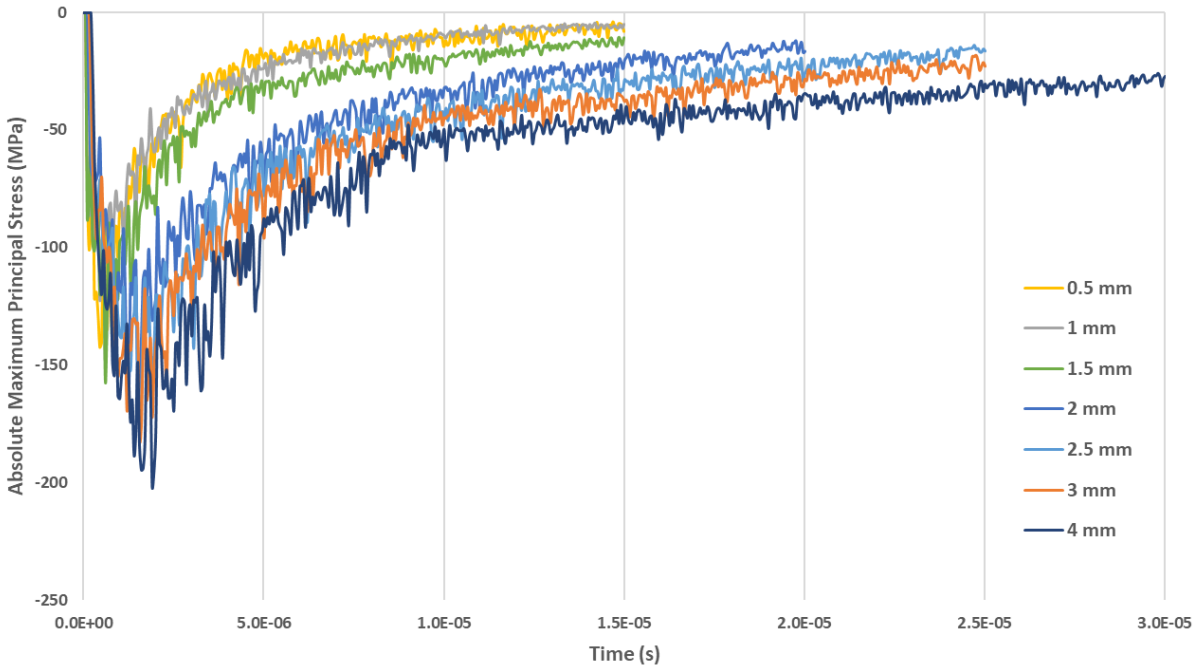

Source: Author (2024).

The data shows that the stress results were physically consistent, with larger droplets reaching greater peak and post-peak stresses, as presented in Figure 58. The impact time duration (total time in which a droplet is imparting stress) also increased with the increased droplet diameter, with smaller droplets showing quicker and sharper post-peak stress decay. The sharper increment in the peak time from the 1.5 mm to the 2 mm droplet diameter is attributed to the changes in geometry and meshing parameters of the larger droplets. Overall, the simulation data was consistent with the empirical observations by LI et al. (2014), ZHANG et al. (2017), and MITCHELL et al. (2019), which have been presented in Section 2.4.

Figure 58 – Peak stress and stress time (AMPS) for multiple droplet diameters impacting the coating at 90 m/s.

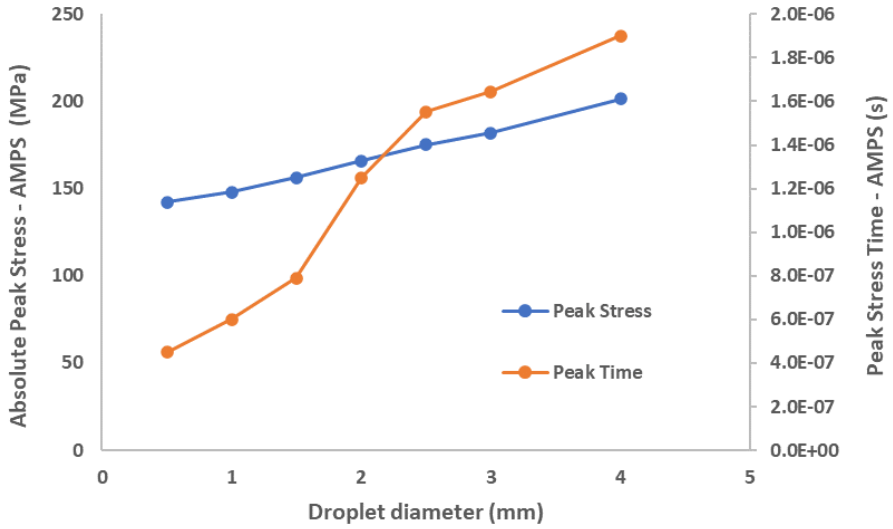

Source: Author (2024).

The impact stress contours depicted in Figures 58 and 59 show the equivalent von-Mises stress behavior over time for the 2 mm diameter droplet. There it is possible to observe the three typical stress waves that emerge from the impact zone. In the top view depicted in Figure 59, the propagation of the shear waves known as Rayleigh waves, waves that move along the surface, interacting with surface cracks, is noticeable in the first stages of impact.

Figure 59 – Top view of the Equivalent von-Mises Stress contours for a 2 mm diameter water droplet impact at 90 m/s.

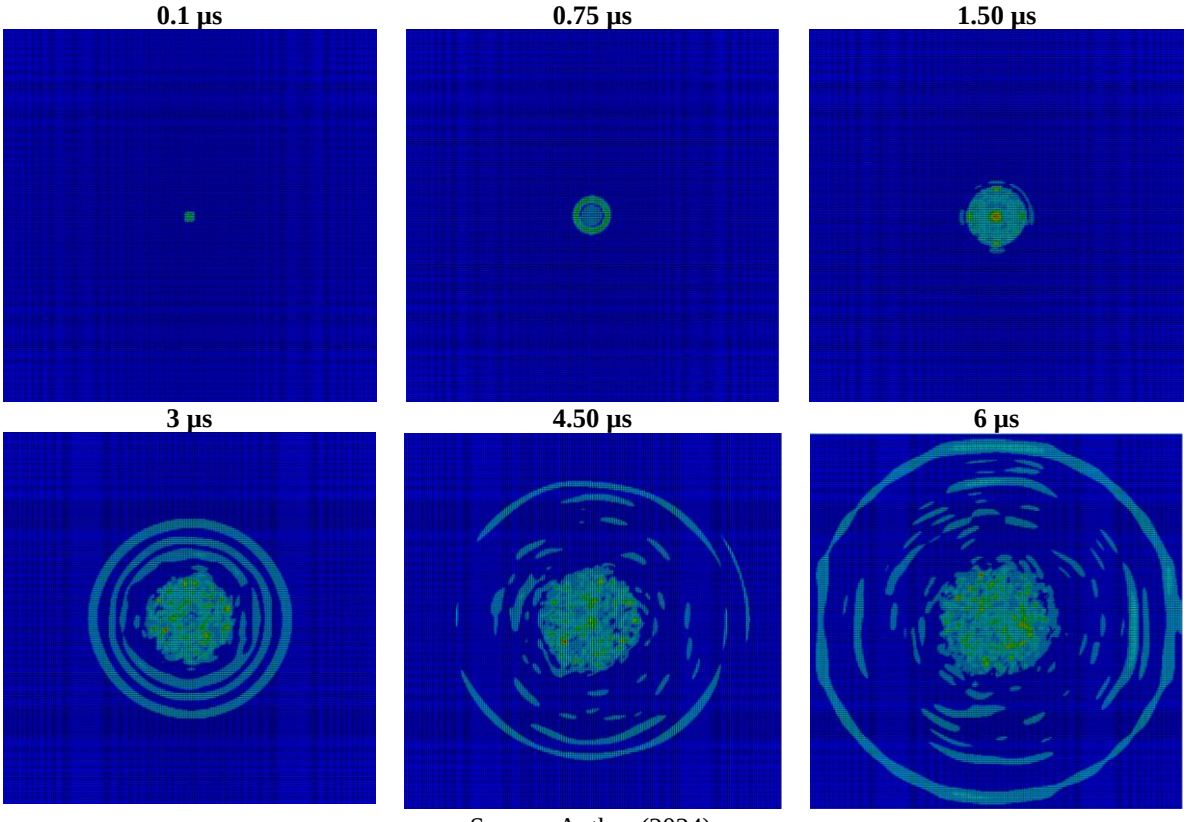

Source: Author (2024).

The other two bulk waves, the compressional waves traveling in a longitudinal direction and the shear wave traveling in a transverse direction, can be noticed throughout the transversal section stress-time history presented in Figure 60. From 1.5 µs onwards, it is possible to notice the wave reflection at the bottom surface and its interference with the initial compressive waves, a mechanism that damages the material at different depths, as observed by BRUNTON (1966).

Figure 60 – Transversal view at the center of the impact point of the Equivalent von-Mises Stress contours for a 2 mm diameter water droplet impact at 90 m/s.

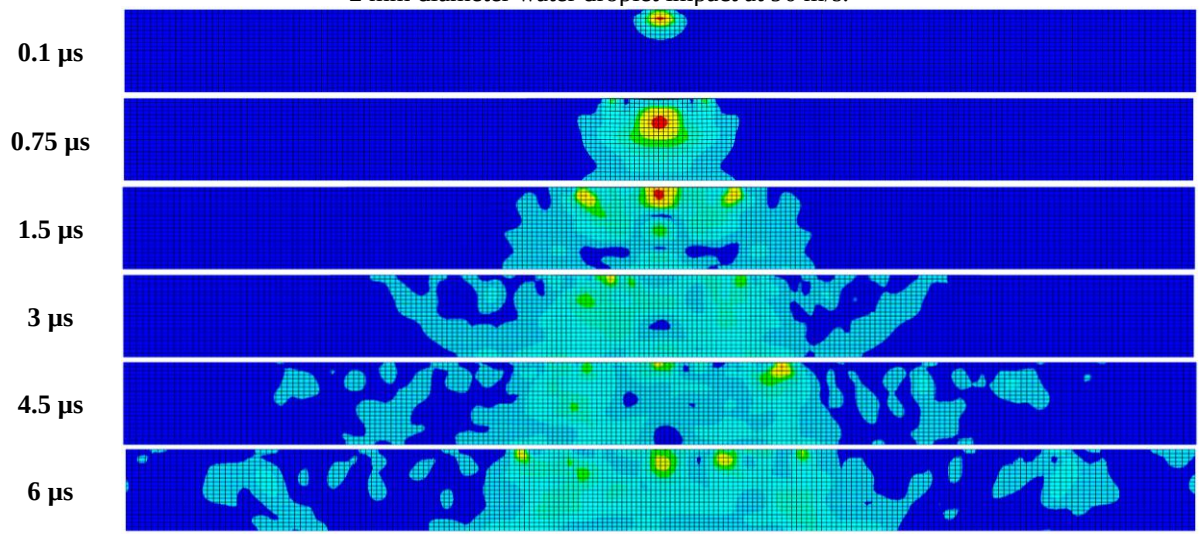

Source: Author (2024).

4.1.3 Computational cost

The steps taken to simplify the simulations proved to be essential in making them feasible considering the computational resources available, especially for the range of the larger droplets. This was mainly grouping the droplets into similar simulation and meshing parameters, of which the limiting of the square edge substrate dimension and the simulation time was the most crucial. For reference, the largest droplet simulation, at 4 mm diameter, took 111.5 hours to complete and the resulting files amounted to 445 GB of disk space. This was a considerable hurdle, especially with a limited 1 TB hard disk, which made it necessary to export, and then delete the simulation data of a previous simulation to start the next.

Symmetry schemes would be the first solution to be employed. This had been considered in the early stages of the work, when the model was first being set, but since symmetry schemes are not compatible with the droplet's SPH meshing in the ANSYS Explicit Dynamics environment, this option was ruled out in the initial stages of development of the computational model. The alternative option, a fully classical Lagrangian mesh had been considered as well, but the simulations either failed to converge, or were predicted to take as

long or longer than the SPH alternative. While being dropped in favor of the meshless method, the application of a fully classical Lagrangian mesh coupled with symmetry tools could still be validated as an option to be used in future works to reduce the computational load.

Second, the solid body mesh can be optimized by applying unstructured meshing and increasing the severity of bias factors to keep the resolution high near the impact point, while reducing the total number of elements. Lastly, with the advancement of measuring techniques, empirical definition of impact-induced stresses is made possible, such as the work of SUN et al. (2022), which employed high-speed stress microscopy to measure the temporal evolution of the shear stress of water droplet impacts on a soft solid surface. Also, new methods such as photoelastic tomography are starting to be deployed for probing the shear and pressure forces on droplet impact (AMERICAN PHYSICAL SOCIETY, 2023). What this means is, that the model could be directly validated with impact stress results instead of indirectly by impact force results, as has been the case in this study. In practice, it will allow the mesh's necessary resolution to be reevaluated (and, optimistically, reduced) by enabling the definition of a mesh convergence point directly tied to stress results.

4.2. RAIN EROSION PREDICTION MODEL

In this section, the detailed results from the fatigue life prediction model, including its sensitivity analysis, are presented and discussed.

4.2.1 Fatigue data sensitivity analysis

To evaluate the impact of variations in input fatigue parameters on the output of the fatigue life model, a sensitivity analysis was conducted. Initially, the input parameters, FSC and FSE, were incrementally altered by a 1% margin from the values used in this work's model (181.48 and 0.0023, respectively), while measuring the output fatigue damage for the 2 mm diameter droplet. The analysis results are summarized in Figure 61. While the FSC presents itself as the greater contributor to the variance of the output parameter, the results show that minor alterations to both input parameters greatly influence the model's fatigue damage output. However, in practice, the FSE is much more sensitive to changes to the base fatigue data, being more inclined to a significant variation, potentially becoming the most influential parameter.

Figure 61 – Sensitivity analysis for the fatigue damage of a 2 mm diameter water droplet by incrementally altering the fatigue input parameters (FSC and FSE) by 1%.

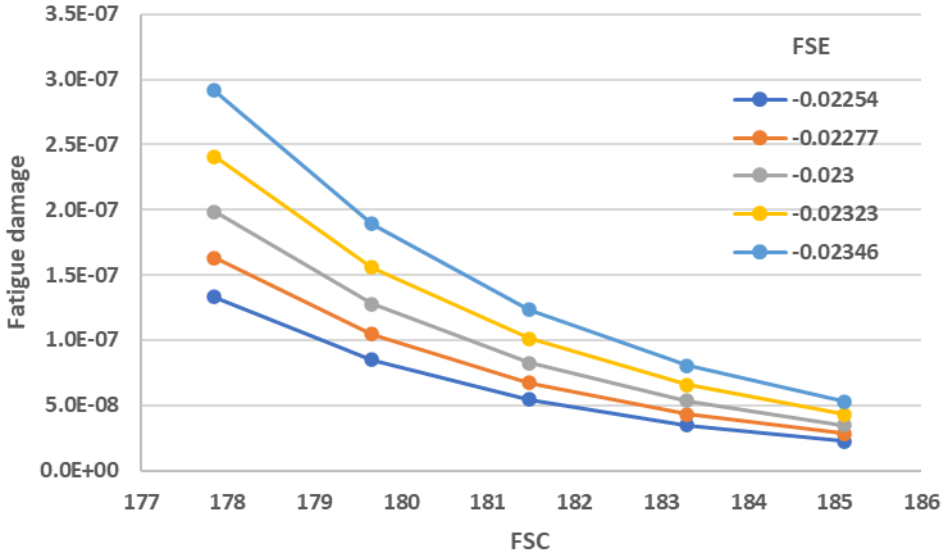

Source: Author (2024).

When comparing the expected fatigue damage for the Hercules 3501-6 and the adapted Epon E862 (the purple triangle and the red square in Figure 62, respectively), it is observed that the former yields a fatigue damage result 75 times greater than the latter. This comparison highlights how much of a difference adapting the Epon E862 fatigue data from the Hercules 3501-6 can make, as well as shedding light on the model's sensitivity and the significant impact that a chosen fatigue method might have.

Figure 62 – Sensitivity analysis for the fatigue damage of a 2 mm diameter water droplet for multiple fatigue input parameters (FSC and FSE). The purple triangle represents the Hercules 3501-6 condition, while the red square represents the Epon E862 adaptation's.

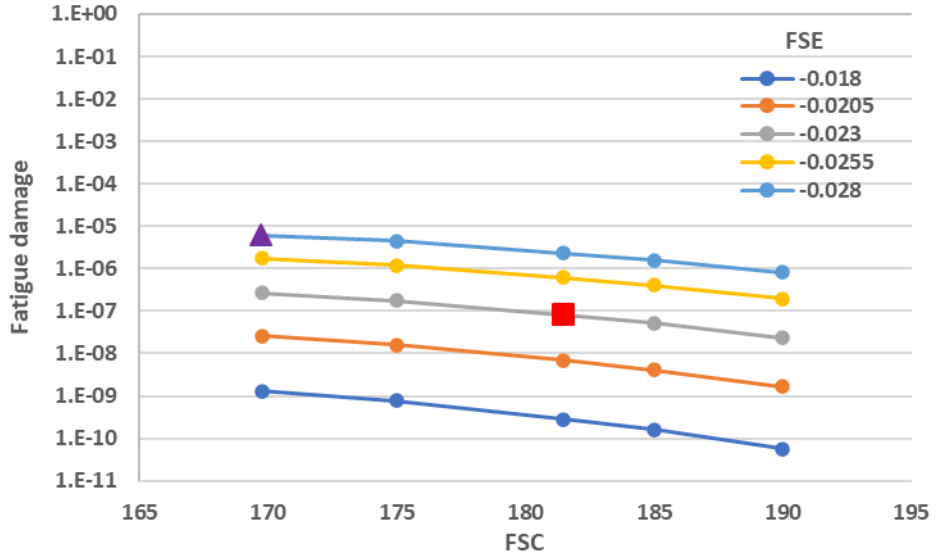

Source: Author (2024).

Previous studies have employed similar fatigue life models that used S-N data from diverse fatigue testing methods, such as tensile (AMIZARDEH et al., 2017b; HU et al., 2021),

or compressive (KAORE et al., 2022). While compressive-compressive fatigue testing might be considered more appropriate than tensile-tensile due to the predominantly compressive nature of the droplet impact stresses, it could be argued that the quasi-static tests are not a suitable substitute for impact fatigue testing (MILELLA, 2012), especially considering the model's large sensitivity to input data. Alternatively, other works related to rain erosion modelling have directly employed impact fatigue testing with impact velocity-life data (VERMA et al., 2021), or adapted rain erosion testing data to obtain it (BECH, HASAGER and BAK, 2018) (although, they have considered the less accurate water hammer pressure equation to ascertain the droplet impact pressures). For future studies, testing the actual coating material with an appropriate impact fatigue testing method, combined with droplet impact computational modelling is recommended in order to produce more accurate input data for such fatigue life models.

4.2.2 Erosion life results

The model end output is the fatigue damage caused by a single droplet (of multiple sizes) impacting a particular material at a particular velocity. Although there is no empirical evidence accessible in the literature specifically relating the liquid droplet diameter to its fatigue impact damage, it is expected that the single impact fatigue damage will increase as the droplet diameter increases, as their greater masses would result in greater kinetic energy and, thus, larger impact stress. This study's fatigue damage data is presented in Figure 63 and is specific to the selected droplet diameters, impact velocity, and epoxy coating.

Figure 63 – Single water droplet fatigue damage for multiple diameters when impacting the Epon E862 epoxy coating at 90 m/s. Also presented in a logarithmic scale for better visualization.

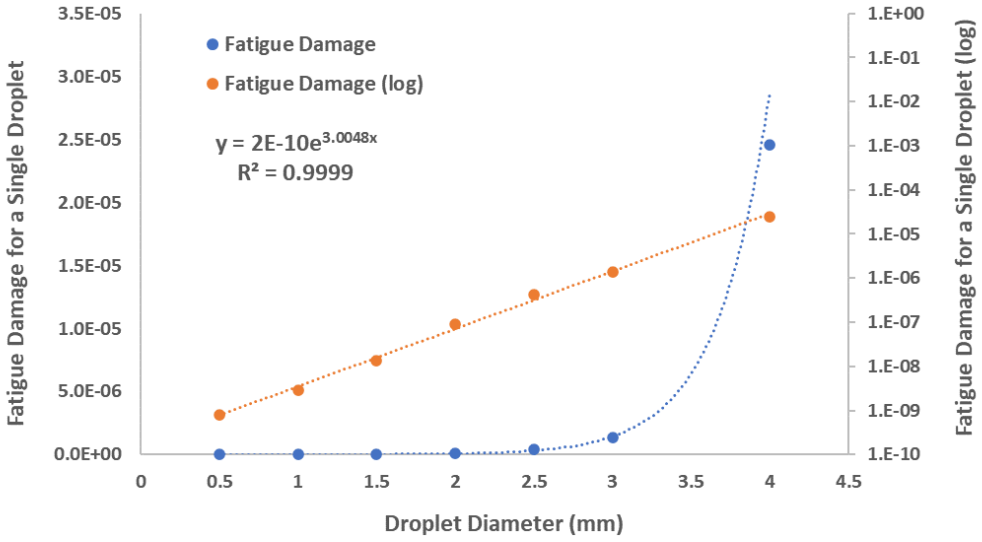

Source: Author (2024).

An exponentially increasing trend in fatigue damage with an increasing drop diameter is observed, and the resulting mathematical equation obtained from the regression of the data provides a very good agreement with the data ($R^2 = 0.9999$) and can be presented as:

$$F_d = (2 \cdot 10^{-10}) \cdot e^{3.0048d} \tag{33}$$

where F_d is the single droplet impact fatigue damage, and d is the droplet diameter. It should be emphasized that this equation is relative to a specific impact velocity, and a specific impacted material. Any changes to both parameters would result in a different equation altogether.

These fatigue damage results were obtained while considering the fatigue damage contribution of Rainflow half-cycles as just half of an equivalent full cycle of the same range and mean stress characteristics (CRANDALL, MARK and KHABBAZ, 1962; MADSEN, 1990; SUTHERLAND, 1999), the recommended practice for wind turbine applications, as had been outlined in Section 2.6.4. Still, there is no clear method in the literature on whether the half-cycles damage contribution should be ignored, accessed as half the equivalent damage, or have its full damage considered. Although there is no clear statement in the text, the latter appears to have been employed in similar studies (AMIRZADEH et al., 2017b; KAORE et al., 2022). To better comprehend how the methodology impacts the fatigue damage, the three methods were tried and their resulting fatigue damages are presented in Figure 64. It is clear from the data that the chosen method is extremely relevant: the oppressive majority of the accumulated fatigue damage results from just the few half-cycles counted, indicating the negligible fatigue damage contributions from the full cycles. As would be expected, the fatigue damage relation between the full and half contribution methods turned out to be double. While the difference is not as great as ignoring the half-cycles contribution, the method choice is very significant when trying to predict failure, for which the full contribution method is the most conservative of the two.

Figure 64 – Single water droplet fatigue damage for multiple half-cycle damage evaluation methods in the literature. The Y-axis in plot (b) is in logarithmic scale for improved visualization.

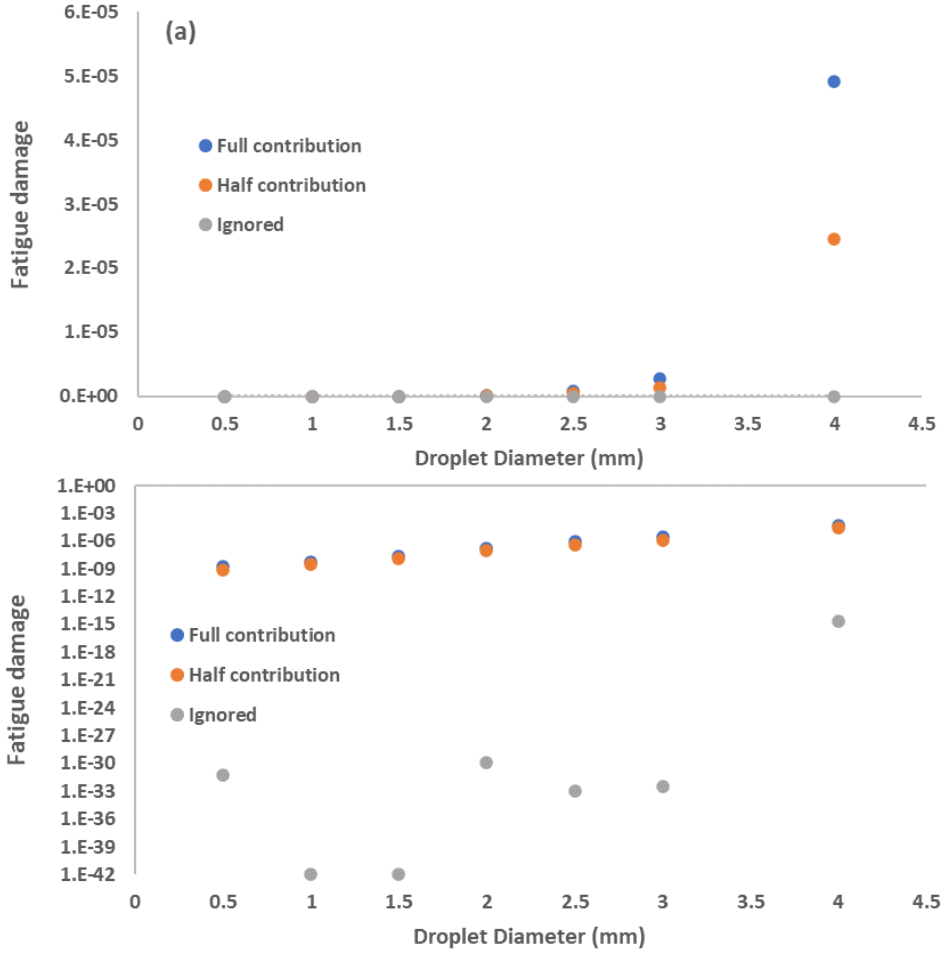

Source: Author (2024).

The combination of the fatigue damage data alongside the equivalent yearly number of droplets was the chosen method to assess the number of impacts necessary for failure (in this case, the end of the incubation period), and the resulting expected erosion onset time for each of the selected location in this study. It is worth reminding that the considered erosion onset marks the end of incubation time, and is related to the total operational time of the wind turbine, and idle time should not be considered. This information is summarized in Table 14 for the RN-04 offshore wind farm.

Table 14 – Erosion onset expectancy data for the coating of a wind turbine located at the RN-04 offshore wind farm.

Droplet diameter (mm)	Equivalent yearly number of droplets	Fatigue Damage	Number of impacts to failure	Erosion onset (years)
0.5	614,479,424	8.12E-10	1.23E+09	2.01
1	76,809,928	2.94E-09	3.40E+08	4.43
1.5	22,758,497	1.32E-08	7.58E+07	3.33
2	9,601,241	8.8E-08	1.14E+07	1.18
2.5	4,915,835	4.31E-07	2.32E+06	0.47
3	2,844,812	1.38E-06	7.27E+05	0.26
4	1,200,155	2.46E-05	4.07E+04	0.03

Source: Author (2024).

Since the method used to ascertain the erosion onset estimate is an approximation based on the total yearly volume of rain being reassigned as the equivalent number of droplets for a single droplet diameter, it is expected that it might lead to skewed results, especially for droplet diameters at the lower and upper ends of the droplet size distribution function. Figure 65 presents the estimated erosion onset data in graphic format.

Figure 65 – Estimated erosion onset for multiple droplet diameters at the RN-04 offshore wind farm.

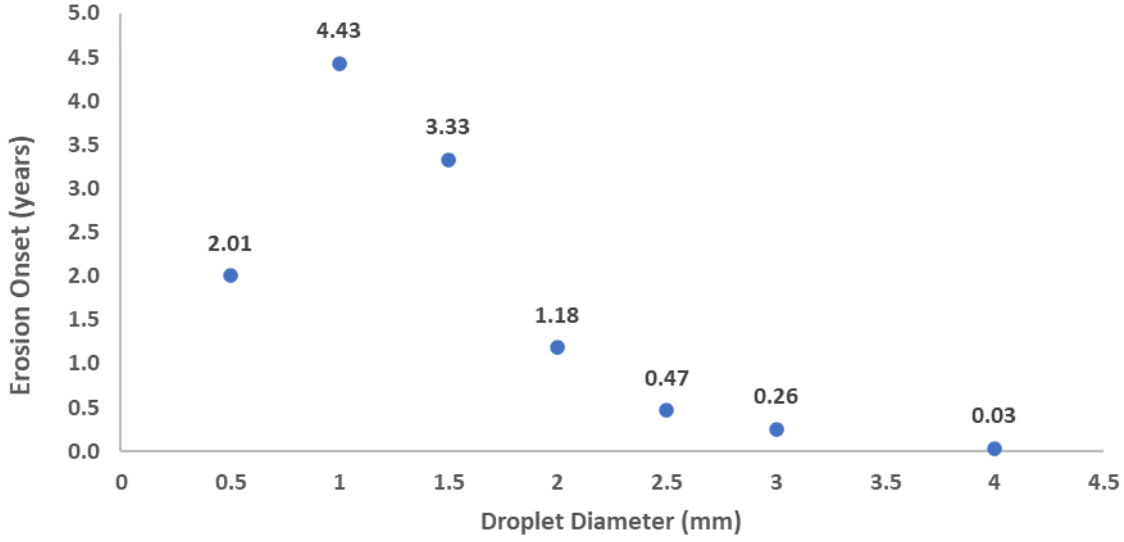

Source: Author (2024).

At the extreme diameters, varied results can be observed. The 0.5 mm diameter droplet, besides having the lowest single droplet fatigue damage, also provided erosion onset results similar to observable field results, even lower than the 1 mm and the 1.5 mm droplet results, which can be justified by the comparatively much higher equivalent number of droplets. On the other end, the 4 mm droplet diameter, besides having a lower equivalent number of droplets, possessed a comparatively much higher single-unit fatigue damage. This results in an overly small erosion onset of 11 days, with failure at around 40.000 impacts. With the current information available in the literature and no empirical testing, it is difficult to ascertain if this is indeed the magnitude of damage for a 4 mm droplet. Otherwise, this is possibly an overestimation of the fatigue damage during the Rainflow cycle counting algorithm of the fatigue life model.

Considering only significant rainfall events, defined as those with a rain intensity greater than 0.2 mm/h (as described in Section 3.1.2), the average rain intensity for a precipitation event in the RN-04 area is approximately 2.5 mm/h. At this rain intensity, the droplet diameter distribution has, approximately, a mean of 1.3 mm with a standard deviation of 0.6 mm. In this average precipitation scenario, every droplet diameter near its range (0.5 mm up to 2 mm diameter) provides erosion onset results in line with most field observations for wind blades, which usually show signs of leading edge erosion within the first 3 years after installation (REMPEL, 2012). The erosion onset results for most droplet diameters were also agreeable with the lifetime results presented in erosion models on similar studies (AMIRZADEH et al., 2017b; VERMA et al., 2021), which ranged from 0.867 up to almost 15 years and considered inland and coastal wind turbines sites, with turbine power ranging from 1.5 up to 13.2 MW. The exceptions, being the three largest droplet diameters, can be linked to the uniform droplet diameter method employed, the fatigue damage overestimation by the Rainflow algorithm, and the previous studies' areas having less intense precipitation.

Possibly, keeping to the average droplet diameter results would be the most accurate method to reach an approximate estimate for the erosion onset. Even considering this, the equivalent droplet number methodology has a clear shortcoming related to the quantitative assessment of the time for the erosion onset. One way to improve upon the fatigue model’s accuracy can be attempted by incorporating additional methods to improve the rain field abstraction model (AMIRZADEH et al., 2017), such as (1) raindrop field distributed impacts, which would require further programming in the ANSYS APDL scripting language, as probing the stress distribution in the entire surface area is not something readily available in the standard

Explicit Dynamics environment; (2) and rain intensity related random sampled individual droplet diameters, which would require a droplet stress library obtained from an interpolation scheme of the simulated stresses, as simulating the entire range of possible droplet diameters and velocities would be too computationally expensive. While one would account for the positioning of the droplet in the rain field, the other would account for impact stress differences due to variations in droplet diameter and impact speed.

Another option to break from the averaging artifices used is to combine real rainfall and wind turbine data from a wind farm for usage in the rain intensity, wind speed, and pitch angle parameters of the model. Last, but not least, the final challenge regards the material characterization. Having a commercial coating fully characterized for its fatigue and elastic - or viscoelastic - properties would be an incredible boon for the assertiveness of the model, improving it twofold: first, by providing an explicit dynamics computational model that simulates the impact to a virtual material much similar to the real one, and second by improving the accuracy of the fatigue life model, estimating failure to the actual fatigue data for the studied material, which is incredibly critical to the model's accuracy, as presented in the sensitivity analysis performed in Section 4.2.1.

Besides these shortcomings, the fatigue model still provided fatigue damage and erosion onset results that are physically coherent, and that are mostly within the expected results, based on real-life observations and the results from similar studies. It should be emphasized that the objective of this study is not to present an accurate erosion life prediction tool. Instead, it aims to give the first steps in developing a multilayered model that can relate climatic characteristics at a wind farm site, to the operating conditions of the turbine, and ultimately to the material properties of a particular coating, providing quantitative results for comparing the risks and potential of rain erosion at specific locations.

5. CONCLUSION

Planning on improving the power supply to the population-dense areas along its extensive coast, the offshore wind generation is considered to be a key, strategic complement to the Brazilian energy matrix in the upcoming years, especially along the Northeastern coast of the country, which is bound to be the hotspot for offshore wind energy in the country. With the increasing interest in offshore wind farms, their notably higher maintenance costs, and susceptibility to leading edge erosion, predicting when the coating system will start failing will be crucial for maintenance planning and keeping the AEP performance of the wind turbine at the highest level.

This work intends to deliver an initial modelling basis, application, and methodological review for a computational failure prediction model for the analysis of rain erosion in the leading edge of offshore wind turbine blades, providing:

1. An in-depth guideline for creating a computational model for simulating a rain droplet impact in ANSYS Explicit Dynamics. While the solid domain was modelled with finite element method, the fluid domain was modelled with the meshless smooth particle hydrodynamics (SPH) method. The contact forces and droplet morphology results were validated with empirical results obtained in the literature.
2. A straightforward location and turbine-specific methodology for evaluating the average operational conditions at offshore wind farm sites, encompassing parameters such as the rainfall intensity, wind turbine power characteristic and tip speed, impacting angle of attack, and wind and droplet velocity. Coupled with the computational model, it allows the simulation and study of rain droplet impact at the operating conditions of a wind turbine blade (model and location-specific). A case study for estimating the erosion onset time of prospective offshore wind turbine blades is considered.
3. A fatigue life model for predicting the erosion onset of wind turbine coatings under rain droplet impact and erosion is presented, providing quantitative results for comparing the risks and potential of rain erosion at specific locations. The fatigue life model resulted in droplet fatigue damage and erosion onset results that are physically coherent and within the expected results based on real-life observations and the results from the literature. The erosion onset estimates were coherent for most droplet diameters, ranging from 0.47 up to 4.43 years of operating time, and consistent with the values found in similar erosion models throughout the literature. Considering the average rain intensity

in the area, the average droplet diameter is 1.3 mm (standard deviation of 0.6 mm), for which the estimated erosion onset is in agreement with real-life observations in wind turbine blade coatings.

4. A sensitivity analysis has been performed to evaluate the impact of changes to fatigue data on the fatigue damage output from fatigue-life failure predictive models. The results indicate that the single droplet fatigue damage is highly sensitive to input fatigue data. Partly due to the scarcity of fatigue testing data for polymeric materials, this study, along with previous works, has relied on S-N data for different materials and testing methods, which may not be appropriate to the simulated scenario of an impacting droplet. This practice is also problematic for the model's accuracy because of its large sensitivity to input data. To improve the accuracy of fatigue life models, future research should focus on testing the actual coating materials with appropriate impact fatigue methods, while combining it with droplet impact computational models.

The subject of rain erosion prediction is very complex, with many related variables to be considered, such as the weather characteristics, the wind turbine’s operating conditions, the material properties of the surface coating, the wind blade structure, and the droplet impact dynamics. As such, rain erosion remains a difficult phenomenon to simulate and even more so to predict. Still, advancements in this field of study can reap great benefits, as the phenomena surrounding the droplet impact is a daily life occurrence that has a very extensive effect, eroding steam and wind turbine blades, scouring aircraft, and wearing away the soil. As such, the research for more appropriate and accurate rain erosion prediction models must continue.

6. SUGGESTIONS FOR FUTURE WORKS

- Improvements to the fatigue life model's accuracy can be done by implementing additional methods such as (1) a raindrop field distributed impacts, (2) rain intensity related, randomly sampled droplet diameters coupled with a droplet stress library obtained from an interpolation scheme of the actual simulated stresses, and (3) consider and couple the seasonally variable wind speed and precipitation data into the fatigue model.

- Additional factors intrinsic to wind turbine operation were ignored in the current study and can be considered for model improvements, such as the control strategy of the wind turbine, the effects of varying rotor azimuth angle, and the disturbance caused in the trajectory of the rain droplet due to aerodynamic effects while the blade is rotating.

- Use real-time data from a wind turbine site (wind speed, rain intensity, wind turbine model, blade pitch, coating material parameters) to feed the model, fine-tuning it for more accurate results. Instead of average parameters, a randomly sampled statistical distribution is suggested.

- Execute tensile, fatigue, and rain erosion testing of a commercial LEP material, then simulate it in the model. This should provide more accurate erosion failure results, which can be validated against the material's rain erosion testing performance.

- Use real rain erosion testing data to modify and fine-tune the model to work as a virtual rain erosion tester, mirroring the real apparatus, and providing quicker, cheaper, and ampler data.

- Test different materials and coating configurations, such as viscoelastic materials, GFRP laminates, and multi-layered coatings.

- Apply the model in the study of the erosive effect of solid airborne particles, such as sand, on the leading edge of wind turbines.

REFERENCES

3M. **Wind Protection Tape 2.1.** Available at: https://www.3m.com/3M/en_US/p/d/b5005165002/. Accessed: 14/01/2024.

ABEEólica. **Wind Energy Report 2022**. Available at: https://abeeolica.org.br/energia-eolica/dados-abeeolica/. Accessed: 14/10/2023.

AMERICAN PHYSICAL SOCIETY. **76th Annual Meeting of the Division of Fluid Dynamics.** Session X03: Drops: Impacts on Solid I. November, 2023. Available at: https://meetings.aps.org/Meeting/DFD23/Session/X03?showAbstract.

AMIRZADEH, Behrooz. et al. **A computational framework for the analysis of rain-induced erosion in wind turbine blades, part I: Stochastic rain texture model and drop impact simulations.** Journal of Wind Engineering and Industrial Aerodynamics, 163, 33–43. 2017. DOI: https://doi.org/10.1016/j.jweia.2016.12.006.

AMIRZADEH, Behrooz., et al. **A computational framework for the analysis of rain-induced erosion in wind turbine blades, part II: Drop impact-induced stresses and blade coating fatigue life.** Journal of Wind Engineering and Industrial Aerodynamics, 163, 44–54. 2017. DOI: 10.1016/j.jweia.2016.12.007.

ANSYS, Inc. **ANSYS Explicit Dynamics Analysis Guide.** Release 2019 R2. 2019.

ANSYS, Inc. **Ansys 2023 R2.** Cambridge, UK. 2023.

BASQUIN, O.H. **The exponential law of endurance tests.** Proceedings of the American Society for Testing and Materials 10, 625-30. 1910.

BEAUDOING, H.; RODELL, M. **NASA/GSFC/HSL, GLDAS Noah Land Surface Model L4 monthly 0.25 x 0.25 degree V2.1.** Greenbelt, Maryland, USA, Goddard Earth Sciences Data and Information Services Center (GES DISC), 2020. Accessed: 05/07/2024. DOI: 10.5067/SXAVCZFAQLNO.

BECH, J. I.; HASAGER, C. B.; BAK, C. **Extending the life of wind turbine blade leading edges by reducing the tip speed during extreme precipitation events.** Wind Energy. Sci., 3, 729–748. 2018. DOI: https://doi.org/10.5194/wes-3-729-2018.

BEST, A. C. **The size distribution of raindrops.** Quarterly Journal of the Royal Meteorological Society, v. 76, n. 327, p. 16–36, 1950. DOI: doi.org/10.1002/qj.49707632704.

BILLINGHAM, J.; KING, A. C. **Wave motion.** Cambridge, UK. Cambridge University Press. 2000.

BISHOP, N. W. M.; SHERRATT, F. **Finite Element Based Fatigue Calculations.** HT17, NAFEMS, 2000. DOI: https://doi.org/10.59972/ta5h05jd.

BLADEREP. **LEP 9.** Available at: https://www.bladerep.com/en/products/leading-edge-protection/lep-9. Accessed: 14/01/2024.

BODINI, N.; LUNDQUIST J. K.; KIRINCICH, A. **Offshore Wind Turbines Will Encounter Very Low Atmospheric Turbulence.** J. Phys.: Conf. Ser. 1452, 2020. DOI: 10.1088/1742-6596/1452/1/012023.

BOWDEN, F. P.; FIELD, J. E. **The brittle fracture of solids by liquid impact, by solid impact and by shock.** Proc. R. Soc. London, Ser. A, 282, 331-352, 1964. DOI: doi.org/10.1098/rspa.1964.0236.

BRASIL. **Decreto Nº 10.946, de 25 de janeiro de 2022.** Dispõe sobre a cessão de uso de espaços físicos e o aproveitamento dos recursos naturais em águas interiores de domínio da União, no mar territorial, na zona econômica exclusiva e na plataforma continental para a geração de energia elétrica a partir de empreendimento offshore. Available at: https://www.planalto.gov.br/ccivil_03/_Ato2019-2022/2022/Decreto/D10946.htm. Accessed: 19/03/2022.

BRUNTON, J. H. **High Speed Liquid Impact.** Philosophical Transactions of the Royal Society A: Mathematical, Physical and Engineering Sciences, 260(1110), 79–85. 1966. DOI: https://doi.org/10.1098/rsta.1966.0031.

CEPEL. **New Brazilian Wind Atlas (2013 Simulations).** CEPEL, 2017. Available at: http://novoatlas.cepel.br. Accessed: 09/12/23.

CHEN, J., WANG, J., NI, A. **A review on rain erosion protection of wind turbine blades.** Journal of Coatings Technology and Research. 2018. DOI: 10.1007/s11998-018-0134-8.

COAD, E. J., FIELD, J. E. **The liquid impact resistance of CVD diamond and other infrared materials.** Window and Dome Technologies and Materials V. 1997. DOI: 10.1117/12.277041.

COLE, Stephanie. **Wind Turbine Power Curve.** Available at: https://theroundup.org/wind-turbine-power-curve/. Published at 24/08/2022. Accessed: 24/12/2023.

COOK, S. S. **Erosion by Water-Hammer.** Proceedings of the Royal Society A: Mathematical, Physical and Engineering Sciences, 119(783), 481–488. 1928. DOI: 10.1098/rspa.1928.0107

CORTÉS, Enrique et al. **On the Material Characterisation of Wind Turbine Blade Coatings: The Effect of Interphase Coating–Laminate Adhesion on Rain Erosion Performance.** Materials, 10, 1146, 2017. DOI: https://doi.org/10.3390/ma10101146.

COSTA, Ángel M. et al. **New Tendencies in Wind Energy Operation and Maintenance.** Applied Sciences, 11, 1386. 2021. DOI: https://doi.org/10.3390/app11041386.

CRANDALL, S. H.; MARK, W. D.; KHABBAZ, G. R. **The Variance in Palmgren-Miner Damage Due to Random Loading.** Cambridge: Massachusetts Institute of Technology, 1962.

DAI, Juchuan et al. **Research on power coefficient of wind turbines based on SCADA data.** Renewable Energy 86, 206–215, 2016. DOI: https://doi.org/10.1016/j.renene.2015.08.023.

DAVIS, Neil N. et al.[1] **The Global Wind Atlas: A high-resolution dataset of climatologies and associated web-based application.** Bulletin of the American Meteorological Society, Volume 104: Issue 8, Pages E1507-E1525, August 2023. DOI: https://doi.org/10.1175/BAMS-D-21-0075.1.

DÍAZ, H.; SOARES, C. G. **Review of the current status, technology and future trends of offshore wind farms.** Ocean Engineering, 209, 107381. 2020. DOI: 10.1016/j.oceaneng.2020.10738.

DOAGOU-RAD, S.; MISHNAEVSKY, L. **Rain erosion of wind turbine blades: computational analysis of parameters controlling the surface degradation.** Meccanica 55, 725–743, 2020. DOI: https://doi.org/10.1007/s11012-019-01089-x.

DOAGOU-RAD, S.; MISHNAEVSKY, L.; BECH, J. I. **Leading edge erosion of wind turbine blades: Multiaxial critical plane fatigue model of coating degradation under random liquid impacts.** Wind Energy; 1–15. 2020. DOI: doi.org/10.1002/we.2515.

DOWNING, S.D., SOCIE, D.F. **Simple rainflow counting algorithms.** Int. J. Fatigue 4 (1), 31–40. 1982. DOI: https://doi.org/10.1016/0142-1123(82)90018-4.

GARCIA, J. P. S. D. L. **Wind turbine database: modelling and analysis with focus on upscaling.** Master's thesis, Chalmers University of Technology, Göteborg, Sweden. 2013. Available at: https://publications.lib.chalmers.se/records/fulltext/179591/179591.pdf.

GAUDERN, N. **A practical study of the aerodynamic impact of wind turbine blade leading edge erosion.** Journal of Physics: Conference Series, 524, 012031. 2014. DOI: 10.1088/1742-6596/524/1/012031.

GENERAL ELECTRIC. **Haliade-X offshore wind turbine.** Available at: https://www.ge.com/renewableenergy/wind-energy/offshore-wind/haliade-x-offshore-turbine. Accessed: 03/03/2022.

GINGOLD, R. A., MONAGHAN, J. J. **Smoothed particle hydrodynamics: theory and application to non-spherical stars.** Monthly Notices of the Royal Astronomical Society, 181(3), 375–389. 1977. DOI: 10.1093/mnras/181.3.375.

GLOBAL ENERGY MONITOR. **Brazil Atlantic Coast Offshore Wind Development.** Available at: https://www.gem.wiki/Brazil_Atlantic_Coast_Offshore_Wind_Development. Accessed: 09/07/2024.

GRUNDWÜRMER, Matthias et al. **Sol–gel derived erosion protection coatings against damage caused by liquid impact.** Wear, Volume 263, Issues 1–6, Pages 318-329, 2007. DOI: https://doi.org/10.1016/j.wear.2006.12.039.

[1] Data obtained from the Global Wind Atlas version 3.3, a free, web-based application developed, owned and operated by the Technical University of Denmark (DTU). The Global Wind Atlas version 3.3 is released in partnership with the World Bank Group, utilizing data provided by Vortex, using funding provided by the Energy Sector Management Assistance Program (ESMAP). For additional information: https://globalwindatlas.info.

HAN, W., KIM, J., KIM, B. **Effects of contamination and erosion at the leading edge of blade tip airfoils on the annual energy production of wind turbines.** Renewable Energy, 115, 817–823. 2018. DOI: 10.1016/j.renene.2017.09.002.

HATTORI, S., HIROSE, T., SUGIYAMA, K. **Prediction method for cavitation erosion based on measurement of bubble collapse impact loads.** Wear 269 (7), 507–514. 2010. Available at: https://deepblue.lib.umich.edu/bitstream/handle/2027.42/84234/CAV2009-final33.pdf;sequence=1. Accessed: 21/02/2024.

HERRING, Robbie. **Integration of Thermoplastic/Metallic Erosion Shields into Wind Turbine Blades to Combat Leading Edge Erosion.** Technical Presentation. 2018. Available at: https://rave-offshore.de/files/downloads/konferenz/konferenz-2018/Finale_Praesentationen/16243.pdf. Accessed: 14/01/2024.

HERRING, Robbie et al. **The increasing importance of leading edge erosion and a review of existing protection solutions.** Renewable and Sustainable Energy Reviews. 115. 2019. DOI: https://doi.org/10.1016/j.rser.2019.109382.

HERRING, Robbie et al. **Assessment of a wind turbine blade erosion lifetime prediction model with industrial protection materials and testing methods.** Coatings 11, no. 7, 767. 2021. DOI: https://doi.org/10.3390/coatings11070767.

HEYMANN, F. J. **"Erosion by Liquids... the Mysterious Murderer of Metals"**. Machine Design, pp. 118-124. 1970.

HEYMANN, F.J. **Toward quantitative prediction of liquid impact erosion. In Characterization and Determination of Erosion Resistance.** ASTM Special Technical Publication (474); ASTM International: West Conshohocken, PA, USA, 1970.

HU, Weifei et al. **A computational framework for coating fatigue analysis of wind turbine blades due to rain erosion.** Renewable Energy, 170, 236-250. 2021. DOI: https://doi.org/10.1016/j.renene.2021.01.094.

IBAMA. **Mapas de projetos em licenciamento - Complexos Eólicos Offshore.** Available at: https://www.gov.br/ibama/pt-br/assuntos/laf/consultas/mapas-de-projetos-em-licenciamento-complexos-eolicos-offshore. Updated: 07/05/2024.

IBRAHIM, M. E.; MEDRAJ, M. **Water Droplet Erosion of Wind Turbine Blades: Mechanics, Testing, Modeling and Future Perspectives.** Materials (Basel). 13(1): 157. 2020. DOI: https://doi.org/10.3390/ma13010157.

IEC. **IEC 61400-12-1: Power performance measurements of electricity producing wind turbines.** 2005.

IRENA. **Wind Energy Data – Installed Capacity Trends.** IRENA Tableau Database. Available at: https://www.irena.org/wind. Accessed: 29/06/2024.

JACKSON, M. J., FIELD, J. E. **Modelling liquid impact fracture thresholds in brittle materials.** British Ceramic Transactions, 99(1), 1–13. 2000. DOI: 10.1179/bct.2000.99.1.1

JANISZEWSKI, Piotr. **Python implementation of the ASTM E1049-85 rainflow cycle counting algorythm for fatigue analysis.** Rainflow 3.2.0 Python Project. 2023. Available at: https://pypi.org/project/rainflow/.

JENKINS, D., BOOKER, J. **The impingement of water drops on a surface moving at high speed.** In: Richardson E.G., editor. Proceedings of the Aerodynamic Capture of Particles; Leatherhead Surrey, UK. 13–14 January 1960; Oxford, UK: Pergamon Press. 1960.

JOUKOWSKY, N. **Über den hydraulischen Stoss in Wasserleitungsrohren.** 1898.

KAORE, A. N. et al. **Turbine specific fatigue life prediction model for wind turbine blade coatings subjected to rain erosion.** Materials Today Communications, v. 31, p. 103487. 2022. DOI: https://doi.org/10.1016/j.mtcomm.2022.103487.

KEEGAN, M. H., NASH, D. H., STACK, M. M. **On erosion issues associated with the leading edge of wind turbine blades**. J. Phys. D: Appl. Phys. 46 383001. 2013. DOI: 10.1088/0022-3727/46/38/383001.

KEEGAN, M. H.; NASH, D. H.; STACK, M. M. **Wind Turbine Blade Leading Edge Erosion: An Investigation of Rain Droplet and Hailstone Impact Induced Damage Mechanisms.** Strathprints. Strath.ac.uk. 2014. Available at: https://strathprints.strath.ac.uk/58904/.

KINSLER, Lawrence et al. **Fundamentals of Acoustics.** New York: John Wiley & Sons, Inc. 2000.

LESSER, M. B., FIELD J. E. **The impact of compressible liquids.** Annual review of fluid mechanics, 15(1), 97-122. 1983. DOI: doi.org/10.1146/annurev.fl.15.010183.000525.

LESSER, Martin. **Thirty years of liquid impact research: a tutorial review.** Wear, 186-187, 28–34. 1995. DOI: https://doi.org/10.1016/0043-1648(95)07190-3.

LI, Jingyin et al. **Impact force of a low speed water droplet colliding on a solid surface.** Journal of Applied Physics 116, 214903. 2014. DOI: https://doi.org/10.1063/1.4903316.

LITTEL, Justin D. **Measurement of epoxy resin tension, compression and shear-strain curves over a wide range of strain rates using small test specimens.** Journal of Aerospace Engineering, vol. 21, no. 3, pp. 162-73. 2008. DOI: https://doi.org/10.1061/(ASCE)0893-1321(2008)21:3(162).

MADSEN, P. H. **Recommended Practices for Wind Turbine Testing and Evaluation**. Vol. 3 - Fatigue Loads, International Energy Agency, 1990.

MATSUISHI, M.; ENDO, T. **Fatigue of metals subjected to varying stress.** Paper presented to Japan Soc Mech Engrs. Jukvoka, Japan. 1968.

MILELLA, Pietro Paolo. **Fatigue and corrosion in metals.** Springer Science & Business Media, 2012.

MINER, M. A. **Cumulative damage in fatigue.** Journal of Applied Mechanics 12, 159-64. 1945.

MISHNAEVSKY, Leon et al. **Micromechanisms of leading edge erosion of wind turbine blades. X-ray tomography analysis and computational studies.** Wind Energy, 1–16. 2019. DOI: https://doi.org/10.1002/we.2441.

MISHNAEVSKY, Leon. **Toolbox for optimizing anti-erosion protective coatings of wind turbine blades: Overview of mechanisms and technical solutions.** Wind Energy, 1–18. 2019. DOI: https://doi.org/10.1002/we.2378.

MITCHELL, Benjamin R. et al. **The transient force profile of low-speed droplet impact: measurements and model.** Journal of Fluid Mechanics, 867, 300–322. 2019. DOI: 10.1017/jfm.2019.141.

MOK, C. **A cumulative damage concept in rain erosion study.** AIAA J., 7, 751–753. 1969. DOI: https://doi.org/10.2514/3.5206.

NASA. Global Precipitation Measurement. IMERG's database. Accessed: 08/07/2024. Available at: https://gpm.nasa.gov/data/imerg.

NIJSSEN, R. P. L. **Fatigue Life Prediction and Strength Degradation of Wind Turbine Rotor Blade Composites.** Tech. Rep. SAND2006-7810P, Sandia National Laboratories. 2006.

NØRGAARD, P. H., HOLTTINEN, H. **A multi-turbine power curve approach.** 2004. Available at: www.semanticscholar.org/paper/A-Multi-Turbine-Power-Curve-Approach-N%C3%B8rgaard-Holttinen/bbe01a9987893a53bd3c443b7e9b2773046f725c.

O'CARROLL, Anthony. **Correlation of Mechanical Properties to Rain Erosion Resistance of Polymeric Materials.** M.Sc. Thesis, University of Limerick, Limerick, Ireland, 2018. DOI: dx.doi.org/10.13140/RG.2.2.33222.93769.

PALMGREN, A. **Die Lebensdauer von Kugellagern.** Zeitschrift des Vereins Deutscher Ingenieure 68, 339-41. 1924.

PERROT, Pierre. **A to Z of Thermodynamics.** Oxford University Press. ISBN 978-0-19-856552-9. 1998.

POLLAK, Daniel Alexander. **Characterization of Ambient Offshore Turbulence Intensity from Analysis of Nine Offshore Meteorological Masts in Northern Europe.** DTU Wind Energy Master Thesis M-0056, 8 March 2014. Available at: https://c2wind.com/f/content/daniel-pollak-edited.pdf.

POLYTECH. **ELLE™ Leading Edge Protection.** Available at: https://www.polytech.com/media/4315/elle-product-brochure-eng.pdf. Accessed: 14/01/2024.

POWELL, S. **3M Wind Blade Protection Coating W4600.** Industrial Marketing Presentation. 2011.

PREECE, C. M., MACMILLAN, N. H. **Erosion**. Annual Review of Materials Science, 7(1), 95–121. 1977. DOI: 10.1146/annurev.ms.07.080177.

REMPEL, Lisa. **Rotor blade leading edge erosion-real life experiences.** Wind Systems Magazine, October. 2012.

ROSATO et al. **Designing with Plastics and Composites: A Handbook.** 1991.

RYCHLIK, Igor. **A new definition of the rainflow cycle counting method.** International Journal of Fatigue. Volume 9, Issue 2, Pages 119-121. 1987. DOI: https://doi.org/10.1016/0142-1123(87)90054-5.

SAINT-DRENAN, Yves-Marie et al. **A parametric model for wind turbine power curves incorporating environmental conditions.** Renewable Energy, 157, 754-768, ISSN 0960-1481, 2020. DOI: https://doi.org/10.1016/j.renene.2020.04.123.

SAPRE, Chinmay. **Turbine blade erosion and the use of wind protection tape.** M.Sc. Thesis, University of Illinois at Urbana-Champaign. 2012. Available at: http://hdl.handle.net/2142/31084.

SAREEN, A., SAPRE, C.A., SELIG, M.S. **Effects of leading edge erosion on wind turbine blade performance.** Wind Energy 17 (10), p. 1531–1542. 2014. DOI: 10.1002/we.1649.

SIGALOTTI, L. D. G., KLAPP, J., GESTEIRA, M. G. **The Mathematics of Smoothed Particle Hydrodynamics (SPH) Consistency.** Front. Appl. Math. Stat. 7:797455. 2021. DOI: 10.3389/fams.2021.797455.

SILVA, Gustavo Rodrigues. **Características de vento da Região Nordeste: análise, modelagem e aplicações para projetos de centrais eólicas.** Master's Dissertation. Graduate Program in Mechanical Engineering, Universidade Federal de Pernambuco, Recife, 2003. Available at: repositorio.ufpe.br/handle/123456789/5432.

SØRENSEN, J. D. **Framework for risk-based planning of operation and maintenance for offshore wind turbines.** Wind Energy, 12(5), 493–506. 2009. DOI: 10.1002/we.344.

SPRINGER, G. S.; YANG, C. I. **Model for the Rain Erosion of Fiber Reinforced Composites.** AIAA J. 13 (7), 887-883, 1975.

SPRINGER, G.S. **Erosion by Liquid Impact.** Scripta Publishing Co. 1976.

SUDHAMSHU, A. R. et al. **Numerical study of effect of pitch angle on performance characteristics of a HAWT.** Engineering Science and Technology, Volume 19, Issue 1, Pages 632-641, March 2016. DOI: https://doi.org/10.1016/j.jestch.2015.09.010.

SUN, T. et al. **Stress distribution and surface shock wave of drop impact.** Nature Communications, 13(1), 1-8. 2022. DOI: https://doi.org/10.1038/s41467-022-29345-x.

SURESH, Subra. **Fatigue of Materials.** Cambridge University Press. 2nd Edition. 1998. DOI: https://doi.org/10.1017/CBO9780511806575.

SUTHERLAND, Hebert J. **On the Fatigue Analysis of Wind Turbines.** Sandia National Laboratories. Technical Report. 1999. Available at: www.osti.gov/servlets/purl/9460.

THIRUVENGADAM, Alagu. **The concept of erosion strength.** In Erosion by Cavitation or Impingement; ASTM Special Technical Publication (408); ASTM International: West Conshohocken, PA, USA. 1967.

THOMAS, G.P., BRUNTON, J.H. **Drop impingement erosion of metals.** Proceedings of the Royal Society of London. Series A, Mathematical and Physical Sciences, Volume 314, Issue 1519, pp. 549-565. 1970. DOI: https://doi.org/10.1098/rspa.1970.0022.

VARGHESE, R.; PAKRASHI, V.; BHATTACHARYA, S. A. **Compendium of Formulae for Natural Frequencies of Offshore Wind Turbine Structures.** Energies 2022, 15, 2967. DOI: https://doi.org/10.3390/en15082967.

VERMA, A. S. et al. **Numerical investigation of rain droplet impact on offshore wind turbine blades under different rainfall conditions: A parametric study.** Composite Structures, 112096. 2020. DOI: 10.1016/j.compstruct.2020.112096.

VERMA, A. S. et al. **A probabilistic long-term framework for site-specific erosion analysis of wind turbine blades: A case study of 31 Dutch sites.** Wind Energy, 24(11), 1315-1336. 2021. DOI: doi.org/10.1002/we.2634.

VESTAS. **V236-15.0 MW offshore wind turbine**. Available at: https://www.vestas.com/en/products/offshore/V236-15MW. Accessed: 15/10/2023.

WALRATH, David E.; ADAMS, Donald F. **Fatigue Behavior of Hercules 3501-6 Epoxy Resin.** Report No. NADC 78139 60. 1980.

WANG, Yan et al. **CFD simulation on wind turbine blades with leading edge erosion.** Journal of Theoretical and Applied Mechanics, p. 579–593. 2021. DOI: https://doi.org/10.15632/jtam-pl/141546.

WIND-TURBINE-MODELS. **GE Haliade-X 12 MW.** Available at: https://en.wind-turbine-models.com/turbines/1809-ge-general-electric-ge-haliade-x-12-mw. Accessed: 12/12/2023.

WÖHLER, August. **Versuche liber die Festigkeit der Eisenbahnwagenachsen. Zeitschrift fur Bauwesen 10**; English summary (1867). Engineering 4, 160-1. 1860.

XU, L.; BHAMIDIPATI, V. **An efficient method to estimate the SN curves of engineering materials.** Proceedings of the SEM Annu. Conf. Expo. Exp. Appl. Mech., 2002. Available at: https://www.researchgate.net/publication/267713142_An_Efficient_Method_to_Estimate_the_S-N_Curves_of_Engineering_Materials.

ZHANG, Bin et al. **Experimental studies on the effect of Reynolds and Weber numbers on the impact forces of low-speed droplets colliding with a solid surface.** Exp. Fluids 58 (9), 125. 2017. DOI: 10.1007/s00348-017-2413-z.

ZHANG, Bin et al. **Effects of droplet shape on impact force of low-speed droplets colliding with solid surface.** Experiments in Fluids 60, 64. 2019. DOI: https://doi.org/10.1007/s00348-019-2712-7.

APPENDIX A – FATIGUE LIFE MODEL SCRIPT

```
!pip install rainflow
import decimal

# Ultimate Compressive Strength [MPa]
UCS = 180

# Fatigue Strength Coefficient
FSC = 181.21
FSC = decimal.Decimal(FSC)

# Fatigue Strength Exponent
FSE = -0.023
FSE = decimal.Decimal(FSE)

# Fatigue damage counter
fatigue_damage = 0

# Insert Stress Signal in Pa
signal = []

# Rainflow Cycle counting algorithm
import rainflow
rainflow.count_cycles(signal)

print("Rainflow cycle counting output table:")
print("")
print ("StressRange MeanStress CycleType Start End")

for rng, mean, count, i_start, i_end in rainflow.extract_cycles(signal):

   # Print cycle count output (stress range, stress amplitude, cycle type (full or half), cycle start, cycle
end)
   print(rng, mean, count, i_start, i_end)

   # Mean Stress Correction (Linear Goodman Relation)
   rng_corrected = decimal.Decimal((rng/1000000)/(1-(mean/(1000000*UCS))));

   # Basquin's law application for ascertaining the maximum cycles at the stress range
   Nmax = decimal.Decimal((rng_corrected/(FSC))**(1/FSE));

   # Palmgren-Miner cumulative fatigue damage algorithm
   if count == 1:
     fatigue_damage = fatigue_damage + rng_corrected/Nmax
   if count == 0.5:
     fatigue_damage = fatigue_damage + (rng_corrected/Nmax)/2

print (" ")
print ("Droplet fatigue damage:")
print('{:.2e}'.format(fatigue_damage))
```